UNIVERSITY OF OSLO

Master's Thesis

Metal-Insulator Transitions in Rare-Earth Nickelates for Next-Generation Electronics

A Case Study of Neodymium Nickelate by Atomic Layer Deposition

Linn-Margrethe Rykkje

Materials Science for Energy and Nanotechnology
60 Credits

Department of Chemistry
The Faculty for Mathematics and Natural Sciences

Abstract

Miniaturization of silicon-based transistors has for more than 50 years played a key role in improving electronic device performance. With sizes now approaching the fundamental limit, however, continued technological progress will rely on finding alternative materials with better functionality. To that end, this thesis explores the potential of rare-earth nickelate (RENiO$_3$, RNO) thin films for room-temperature electronics, focusing particularly on NdNiO$_3$ for its exotic electronic behavior.

While RNOs have attracted *significant* attention in fundamental research, their potential for industrial purposes remains untapped. This work attempts to bridge that gap by demonstrating the success of a new, low-temperature synthesis route of NdNiO$_3$ thin films using atomic layer deposition (ALD). We show that NdNiO$_3$ deposited at 225 °C with ALD results in uniform, as-deposited crystalline thin films, whose stoichiometry can be precisely tuned by varying the pulsed ratio between the metal-organic precursors, Nd(thd)$_3$ and Ni(acac)$_2$.

In complex oxide ALD, the pulsing scheme not only dictates the chemical composition, but also governs the growth characteristics of the thin film and its structure. Much of the ability to control material functionality through ALD synthesis thus comes down to strategically exploiting these rather complex behaviors. By working in a feedback loop between synthesis and characterization, we are able to explore these effects and use them to optimize the structural and electronic properties of NdNiO$_3$ thin films.

For instance, certain pulsing ratios of x:y Nd:Ni facilitated highly crystalline (out-of-plane oriented) thin films with low resistivities as deposited. Conversely, other ratios resulted in amorphous, non-conducting or phase separated thin films, despite the fact that the Nd content in the film (as a % of total cation content) maximally differed by 5 % for these pulsing schemes. These observations underpin the complexity of precursor interactions and atomic arrangement (amongst others) that both provide effective tuning knobs and hamper implementation.

NdNiO$_3$ is the RNO member with its metal-insulator transition (MIT) closest to room temperature, making it the most relevant candidate for room-temperature electronics. Our stoichiometric NdNiO$_3$ thin film undergoes its MIT at 140 K, which we attempt to increase by substituting various REs into it at different degrees. While we were not able to observe any MITs in these thin films, the substitutions induced interesting changes to the relationship between crystallinity and conductivity that merit further investigation.

With sufficient control of functional properties, the metal-insulator transition in RNOs could be used as a fundamentally different switching mechanism in transistors, solving the size challenge and contributing to more efficient and sustainable technology. The work presented in this thesis demonstrates how ALD of NdNiO$_3$ thin films could facilitate such a green transition in the future.

Acknowledgements

This thesis was completed at the University of Oslo for the degree of Master of Science (M.Sc.) in Materials Science for Energy and Nanotechnology. The research was carried out in the research group for Nanostructures and Functional Materials (NAFUMA) at the Department of Chemistry from August 2020 to June 2022.

First and foremost, an immense thank you to my supervisors, Prof. Ola Nilsen and Dr. Henrik Sønsteby. You both welcomed me into the thin-film group from the moment I walked into your offices, and for that I will be forever grateful. Your presence, support and mentoring have extended far beyond just research and I truly could not have wished for better supervisors than you.

I would also like to extend my gratitude to researchers and technical staff that have aided this work. These include Dr. Susmit Kaur for running my PPMS measurement, as well as Victor Bobal and Halvor Dolva for assistance in the MiNa Lab.

Gecko café has become a home away from home over these past two years and it would not have been the same without its former and current inhabitants. So, thank you Mathilde, Yani, and Veronica for keeping spirits high in the office and, most importantly, bringing all the knowledge to quiz-lunches. I have thoroughly enjoyed your company and look with fondness back at the fun times we have had. A special thanks to Veronica for being a social catalyst, teaching me how to work the (ALD) ropes, and supporting me from beginning to end.

I am but one of many M.Sc. students – and now also proper Masters! – at NAFUMA. I am thankful for having had the opportunity to learn from and with you through all these years. Ina and Erlend deserve special recognition for always cheering me up and on; this experience would not have been the same or as enjoyable without you. Ina, I cannot wait to realize all of our small and big future plans that we have put on hold during this trying time. The future is better with you in it. Erlend, you always manage to brighten my day, often with delightfully nerdy puns and jokes, but most of all, just by being you.

Mom and dad, thank you for your never-ending support and love. Despite the famous words of my two-year old self ("Inne kan sølv"), I could not have done this without you and the experiences you have gifted me. Thank you also for letting me explore, fail and learn at my own pace. I love you both.

Last but definitely not least, Odd Petter, my love. You never cease to amaze and inspire me with your patience, empathy, wisdom, and kindness for everyone around you. Even after the longest of days and grumpiest of moods, you make me laugh like no one else can. Because of you I have not only survived, but also learned something in this process. Thank you for all that you are.

List of Abbreviations

acac	Acetylacetonate (2,4-Pentanedione)
AFM	Antiferromagnetic
ALD	Atomic Layer Deposition
CD	Charge disproportionation
GPC	Growth per cycle
MBE	Molecular Beam Epitaxy
MIT	Metal-Insulator Transition
NNO	Neodymium Nickelate, $NdNiO_3$
_pc_	_Pseudo_cubic
PLD	Pulsed Layer Deposition
PM	Paramagnetic
PPMS	Physical Property Measurement System
PVD	Physical Vapor Deposition
RE	Rare-Earth
$RENiO_3$ / RNO	Rare-Earth Nickelate
RP	Ruddlesden-Popper
SE	Spectroscopic Ellipsometry
STO	Strontium Titanate, $SrTiO_3$
thd	2,2,6,6-Tetramethyl-3,5-heptanedione
T_{MIT}	Metal-Insulator Transition Temperature
TMO	Transition Metal Oxide
XPS	X-Ray Photoelectron Spectroscopy
XRD	X-Ray Diffraction
XRF	X-Ray Fluorescence

Table of Contents

1   Introduction

The purpose of this introductory chapter is to provide a broader perspective on the topic at hand. It begins with the rationale and motivation behind the thesis, focusing on a research gap that arises at the intersection between prior art and future visions. The thesis objectives are stated and explained in light of previous research in the field.

1.1   The Big Picture

Today's electronics components are faster, lighter, and more reliable than ever. Concomitantly, the size of electronic devices has decreased. For more than five decades, microchip manufacturers have been able to double the number of transistors on integrated circuits while reducing cost, a predictive observation known as Moore's Law (illustrated in Figure 1.1). On the consumer end, technology has consistently improved in terms of speed, efficiency, and capability, benefitting all facets of the high-tech society we live in.
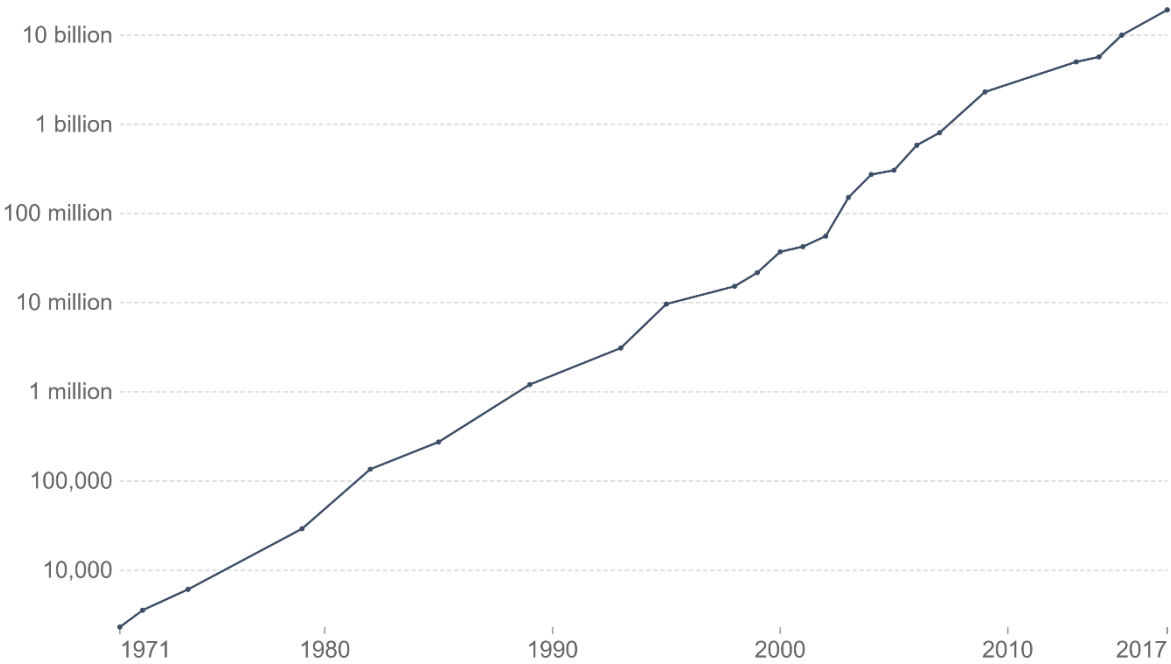
Source: Karl Rupp. 40 Years of Microprocessor Trend Data.   CC BY

Figure 1.1 Illustration of Moore's Law and its predicted increase in the number of transistors in a microprocessor from 1971 to 2017. Data based on [1], obtained via [2].

From a technological perspective, the transistor is performing better than ever. What was once 10 μm (about the size of a blood cell) in size is now a thousand times smaller, with 3 nm transistor nodes soon reaching the market. Questions are lurking in the shadows, however – questions whose answers may have a profound impact on future technology improvement. When, if ever, does Moore's Law come to an end? How far can we push it, how small can we go?

While smaller has equaled better for a long time, the idyll may be coming to end. Transistors are approaching the fundamental size limit defined by the smallest manipulable constituents in the universe (that we know of), namely atoms. Since nothing can be smaller than atoms, and physics and chemistry at the nanometer scale become prone to quantum-mechanical effects, the problem threatening Moore's Law is not simply one of engineering – or is it?

Current transistor design has focused on improving performance by reducing size. As this becomes increasingly challenging, the goal should instead be to find materials that can perform the same function, but better. The potential of such strategies was demonstrated in 2007 when Intel made their most major modification to the transistor since its invention: replacing silicon dioxide (SiO_2) as a gate dielectric with ultrathin films of hafnium dioxide (HfO_2).

Consequently, there has been a surge in research activity trying to find new and sustainable directions for the transistor. Integral to achieving this is finding suitable materials that have relevant functionalities and can be synthesized with high quality and control. This thesis explores one such materials system: rare-earth nickelate ($RE\text{NiO}_3$) thin films deposited with atomic layer deposition. Following the implementation of ultrathin HfO_2 films made with ALD, ALD became embraced by the electronics industry for the low-temperature synthesis of conformal thin films it offers. With the advent of low-temperature epitaxy, it is one of the most promising contenders for application-based research.

As for the rare-earth nickelates, they exhibit an interesting and technologically relevant metal-to-insulator transition (MIT) that arises from a strong, intrinsic structure-property relationship. Being able to exploit the mechanism that drives the MIT could open for new and innovative solutions to the transistor problem. However, the ability to harvest the potential recognized in these materials has been hampered by the complex nature of the underlying physics and strong correlations.

1.2   The Small Details

The fact that rare-earth nickelates exhibit a complex type of MIT does not make the connection to electronics obvious. To understand the connection, it is necessary to briefly revisit the basic operating mechanism of conventional transistors.

Computers use a binary system that stores ones and zeros, representing "on" and "off" states, respectively. Physically, these correspond to switching between two distinguishable states of a material, which semiconductors in transistors do by either allowing a flow of electrons (conducting, on) or restricting it (insulating, off). The activation of the flow is controlled by a gate potential, and the electrons must traverse from source to drain through the channel, whose conductivity is manipulated by the gate voltage. These three components make up the conventional three-terminal transistor.

Rare-earth nickelates with MITs intrinsically exhibit the switching behavior used to differentiate between two states in their ability to transition from metallic to insulating. Since the "switch" is effectively contained within the material itself, *i.e.*, they are not dependent on an applied voltage to reduce a band gap as in silicon semiconductors, they technically might not need a gate oxide to control their state. Instead, they could rely on fundamentally different switching mechanisms, *e.g.*, temperature or strain-coupling, that may be more efficient and energy-conserving. For instance, removing the need for a voltage-controlled third terminal and thus removing the gate oxide outright will drastically reduce power-consumption. Such relatively small modifications to transistor design and build could pave the way for greener and more sustainable technology in the future.

Other, more exotic, architectures depending on rare-earth nickelates are also under development. This includes neuromorphic hardware that has the potential to emulate biological spiking neural networks to perform extremely efficient in-memory computing and extract key information from sensed data. These platforms also have the capacity to learn new tasks and adapt their processing by integrating synaptic plasticity directly on-chip. So-called memristive devices offer high-density, non-volatile analogue and reconfigurable information storage that perfectly fits the requirements for plastic synaptic weights in neuromorphic hardware. A graphic of how $NdNiO_3$ (NNO) can be envisioned for such applications is provided in Figure 1.2. At the fundament lies a deeper understanding of the structure-property relations of the nickelates and their electronic behavior.

The main caveat for implementing such novelties in transistor design is that this requires a functional materials with an MITs around room temperature and two well-separated physical states. This would allow synaptic weight updates directed by joule heating in a two-terminal "transistor". The rare-earth nickelates are promising contenders, but none of them inherently satisfy the temperature-related criterion. One strategy is to tune the MIT temperature (T_{MIT}) and the best starting point is, presumably, the rare-earth nickelate with an MIT closest to room temperature: $NdNiO_3$.
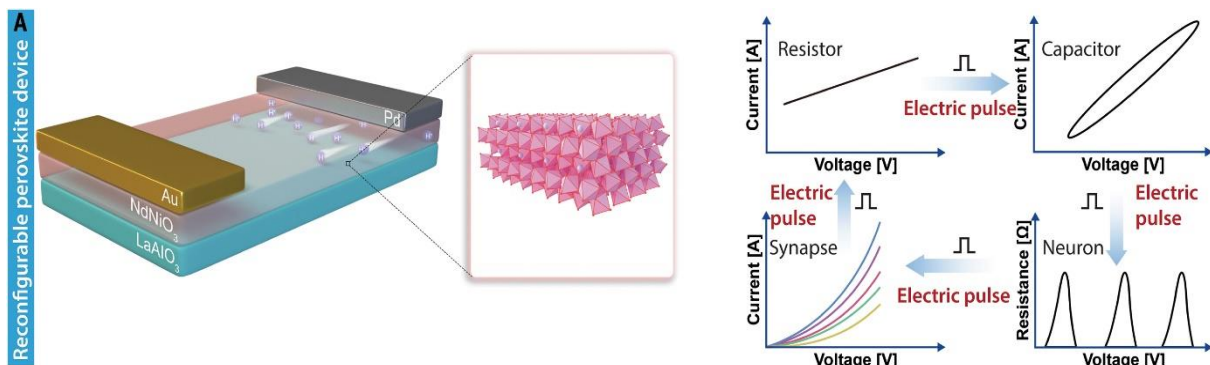
Figure 1.2 Schematic of hydrogen-doped NdNiO3 for reconfigurable devices that can be electrically controlled and transformed into neurons, synapses, and memory capacitors. Reproduced from [3].

1.3   Aim of the Thesis

We see a unique opportunity to bridge the uncertain future of traditional Si-based circuitry in microchips to the unequalled potential of the rare-earth nickelates using ALD. While earlier research has focused on either replacing parts of current transistors with better materials or looking for entirely new strategies, this work could cater to both and thus facilitate a smooth transition to non-Si-based alternatives.

Rare-earth nickelates have the added advantage of being perovskite oxides, which are exceptionally versatile materials due to their structural flexibility and chemical adaptability. This is highly relevant since structural compatibility between a range of materials with different functional properties means that layers (thin films) of these materials can be grown seamlessly on top of each other. In the future, this may be the key to realizing fully integrated perovskite oxide stacks, a benefit that is not available in current Si-based processes.

This thesis represents a potential step in that direction. The aim is to evaluate the prospect of using the rare-earth nickelate $NdNiO_3$ for room-temperature electronics. A synthesis route via ALD has to be developed for thin films of $NdNiO_3$ before chemical, structural and electrical characterization will be used to optimize the physical properties of these films. Attempts to alter the MIT temperature can then be made by investigating the effect of A-site rare-earth substitution in $(RE,Nd)NiO_3$ thin films.

The thesis objectives can be summarized as follows:

- Develop and demonstrate the possibility of ALD as a low-temperature synthesis route for $NdNiO_3$ thin films.

- Use chemical, structural and electrical characterization methods in a feedback loop with synthesis to optimize the functional properties of $NdNiO_3$ thin films.

- Assess the effect of partially substituting Nd with other rare-earth elements to tune the MIT temperature and other related characteristics.

1.4   History and Prior Art

In spite of the current spotlight on rare-earth nickelates, they are far from a recent discovery. First synthesized in bulk form in 1971 by Demazeau *et al.* [4], they were extensively characterized in following years, but only as polycrystalline ceramic samples with single crystallites limited to the size of ~1 μm [5]. This was a result of the challenging synthesis conditions that were required to stabilize the high Ni^{3+} oxidation state. Interest in and possibilities for research were thus renewed when physical

vapor deposition (PVD) methods such as molecular beam epitaxy (MBE), pulsed layer deposition (PLD), and radio frequency (RF) sputtering became able to produce high-quality crystalline thin films.

As a result, the research library on these materials has grown rapidly over the last two decades, spurred on by the RNOs rich and complicated phase diagram (discussed in more detail in 2.3.1). Significant attention has been devoted to investigating the effects of strain [6-8], oxygen non-stoichiometry [9, 10], deposition parameters [11], electric fields [12], and doping [13, 14] on the emerging structural, electronic and magnetic properties. Particularly relevant are studies that concern the MIT temperature and what factors affect it. A linear dependence of the T_{MIT} on composition has been found for solid-solutions of $SmNiO_3$ and $NdNiO_3$ (*i.e.*, $Sm_{1-x}Nd_xNiO_3$) made in both bulk (powder) [15] and thin films [16]. With a near 50/50 ratio between Sm and Nd, a room-temperature T_{MIT} was obtained. An issue with this solid solution, however, is that the MIT becomes smeared out in temperature, and not as sharp as what is needed in the proposed electronic devices. Strain has also been recognized as an effective tuning knob for the MIT by affecting characteristic bond angles in the structure that govern many of the material's functional properties.

Despite these efforts, the seemingly vast potential of the RNOs remains untapped. While studies utilizing MBE, PLD, and RF sputtering have undoubtedly made significant contributions to our fundamental understanding of this materials system, these techniques necessitate high temperatures and pressures that are not compatible with technical processing and industrial integrated circuit manufacturing requirements. As a result, a quality and availability gap between oxide heterostructures and traditional Si-semiconductors has emerged, preventing us from making full use of the diverse functionalities that complex oxides such as RNOs have to offer.

This is likely to change with the prospect of low-temperature ALD synthesis for depositions of high-quality thin films. Functional complex oxide ALD has progressed rapidly in recent years, going from being the unknown cousin of PVD-based methods to an equal contender that offers unmatched thickness and conformality control. The success of ALD was for some time impeded by the need for post-deposition annealing to obtain epitaxial thin films. However, processes with increasing control of as-deposited crystallinity have been developed in the research group for various rare-earth nickelates ($LaNiO_3$ [17], $SmNiO_3$ [18], $EuNiO_3$ [19], $GdNiO_3$ [20]). While epitaxy is not yet routinely achieved, the experimental results from these studies indicate that we are closing in on some of the key parameters. Except for these studies, there are very few other published works on ALD of rare-earth nickelates.

In fact, previous ALD of $NdNiO_3$ – the main character of this thesis – has only been reported twice in literature: first by Sun *et al*. in 2021, looking into the electrochromic properties of $NdNiO_3$ for smart windows [21], and even more recently by Zhang *et al*. in 2022, demonstrating the potential of $NdNiO_3$ as reconfigurable artificial neurons [3]. Both of these routes require post-deposition annealing,

however, removing the intrinsic low-temperature advantage of ALD. Evidently, an established synthesis route for $NdNiO_3$ is still in its infancy, and as deposited epitaxy is yet to be achieved.

2 Theory

This chapter provides an overview of theoretical aspects that help set the thesis work in a scientific context. The characteristics of perovskite oxides and transition metal oxides are introduced and lay the foundation for understanding the rare-earth nickelates and their various transitions. A brief account of thin film theory concludes the chapter.

2.1 Perovskite Oxides

2.1.1 Introduction to perovskites

Much of the interesting behavior and potential of rare-earth nickelates is rooted in underlying interactions and characteristics that generally concern complex oxides (compounds consisting of oxygen in combination with two or more elements), and particularly perovskites. The wealth of diverse functionality in these materials has made them a natural springboard for materials science research and engineering.

Perovskites are a class of materials that share the structural features of their namesake, Perovskite, known as the mineral calcium titanate ($CaTiO_3$). After its discovery in 1893 by Gustav Rose, a vast number of compounds has been found to crystallize in the same structure and these have collectively inherited the perovskite family name. Like $CaTiO_3$ they are typically characterized by a general ABX_3 chemical formula. Here, A is a larger cation than B, while X denotes an anion – most commonly oxygen or a halogen.

Of particular importance to materials science are the perovskite oxides, ABO_3. With a wide range of functional properties, they possess a wealth of potential that makes them technologically relevant for numerous applications. Some perovskite oxide phenomena that have sparked significant interest are high-temperature superconductivity ($YBa_2Cu_3O_7$), colossal magnetoresistance ($La_{1-x}Sr_xMnO_3$ [22]), multiferroicity ($BiFeO_3$ [23]), catalytic activity ($La_{1-x}Ca_xMnO_3$ [24]), and photovoltaic absorbers ($LaVO_3$ [25]). These exemplify a few of the fields and purposes for which perovskite oxides have been envisioned, and new possibilities emerge frequently as various chemical and structural modifications are explored.

In spite of significant research effort, the physical mechanisms underlying these behaviors have yet to be fully elucidated. The immense variety in perovskite oxide chemistries and functionalities offers a playground for scientists to explore and discover; however, it also makes it difficult to predict, control and engineer properties at will. Part of the challenge is rooted in the strong structure-property relationship that typically characterizes perovskite oxides. While the structure gives us a lens to understand properties through, it is in turn often complicated by additional interactions between

lattice, charge, orbital, and spin degrees of freedom. These complexities seem to lie at the heart of what is commonly referred to as *emergent phenomena*: new and often unexpected properties arising from interactions that cannot be understood solely from the behaviors of individual constituents [26].

2.1.2   Perovskite oxide structure

Many perovskite characteristics are best understood *in lieu* of the structural commonalities that define the family. In ABO_3 perovskite oxides, A and B denote two different crystallographic sites (positions in the unit cell) occupied by a larger and smaller cation, respectively. The arrangement of these ions can be visualized as a three-dimensional network of corner-sharing BO_6 octahedra (see Figure 2.1a), each comprised of a six-cornered oxygen cage centered around the B cation. In this picture, the A cations are located in the inter-octahedral cavities with 12-coordination to oxygen.
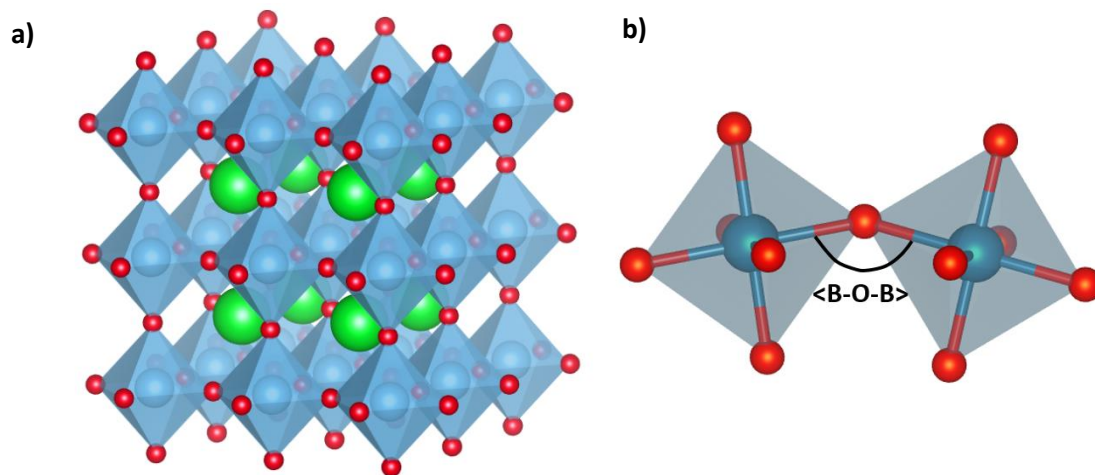
*Figure 2.1 **a)** An ABO₃ perovskite structure shown as a three-dimensional network of corner-connected BO₆ octahedra (blue polyhedra) with the A-site cation located in the cavities between. **b)** Geometric definition of the B-O-B bond angle from octahedral corner-connectivity.*

This description differs from the conventional unit cell representation because it emphasizes the structure's functional BO_6 units rather than its symmetry. It is important to stress, however, that these two perspectives are structurally equivalent, only with a shifted frame of reference, see Figure 2.2. The rationale for using the octahedral packing perspective is that it draws attention to the highly significant B-O-B angle, which is geometrically defined by the corner-connectivity in Figure 2.1 b.
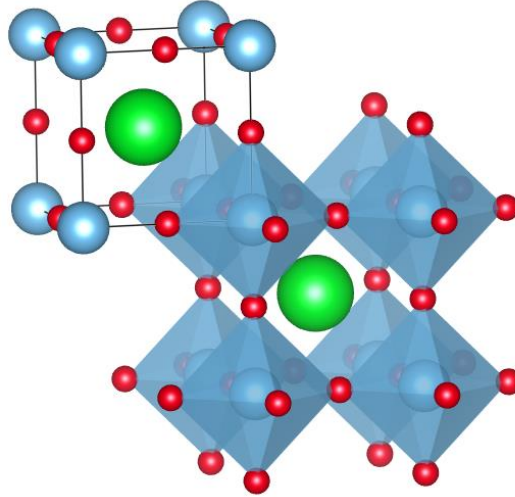
Figure 2.2 Shifted frame of reference for a perovskite unit cell with different definitions of the origin.

Contrary to many other structure types, the perovskite structure is unusually flexible and can accommodate a large number of different combinations of A and B site ions, even with substantial size differences. These variation*s* are typically essentialized by the Goldschmidt tolerance factor (*t*), which quantifies the stability of a structure based on relative ionic size ratios, as shown in Equation 1:

$$t = \frac{r_A + r_O}{\sqrt{2}\,(r_B + r_O)}$$

Eq. 1

$t \approx 1$ represents an ideal cubic structure because it will be stabilized by tight ion packing. If the ratio becomes skewed (deviates from 1), the structure can mitigate the instability by distorting its parent cubic structure through tilts and rotations of the BO_6 octahedra, and, if needed, associative cation displacements [27]. Octahedral rotations typically occur to accommodate the A cation, leaving the environment of the B cation largely unchanged. Such distortions can have dramatic consequences for electronic transport and magnetic ordering because they affect the B-O-B bond angle and the corresponding orbital overlap. Thus, even subtle structural changes can have unexpectedly large consequences for the physical properties of the material. Importantly, these changes can be induced externally, intentionally or not, through the use of atomic defects, pressure or strain, which provides an immensely useful route for tuning and controlling properties.

Although our general understanding of correlation effects and dynamic interactions has progressed significantly over the last decades, theoretical and experimental studies continue to reveal new dimensions of complexity. Our ability to fully harvest the potential of perovskite oxides depends on advancing our methods to acquire a better picture of the dynamics that take place in the crossover regime between physics and chemistry. Much of this is obscured by additional complicating factors, such as d-electron physics in transition metal perovskite oxides and strong electronic correlations (interactions between electrons of comparable energy scales). In the archetype $CaTiO_3$, the cations have no d-electrons, and thus bonding is primarily related to oxygen 2p states. This drastically changes

for *e.g.* transition metals, where electron interactions including d-electrons must be taken into account. Furthermore, interface and heterostructure effects may also be present in the case of thin films. The ultimate goal is to become so familiar with their effects that we can exploit them for applications.

2.2   Transition Metal Oxides

2.2.1   Characteristics of transition metal oxides

The structural adaptability of the perovskite structure has made it a favored structure by ternary transition metal oxides (TMOs), in which at least one of the cation sites (typically the B-site) is occupied by a d-block element. Transition metals often have multiple possible oxidation states and this makes them chemically flexible and compatible with many other ions. The fact that transition metals have their valence electron(s) in the d-orbital(s) further contributes to the rich, varied and unusual landscape of properties exhibited by many TMOs.

There is a strong notion that the nature of d-electrons plays a crucial role for the functional behaviors of TMOs. An important characteristic of d-orbital electrons is that they are neither strongly localized nor fully itinerant, but best described by the crossover regime in which the two characters mix. As is often the case in materials science, nontrivial effects tend to appear in such regimes. Moreover, d-electrons are very spatially confined, meaning that electron-electron correlations are no longer non-negligible, as they are assumed to be in single-particle approximations. As may already have been inferred, these circumstances facilitate a favorable environment for strong correlations and emergent phenomena that are at the origin of more complex physical phenomena.

It is therefore not entirely surprising that many TMOs exhibit unexpected behaviors that do not conform to the traditional models and theories. Studies of these materials have therefore been crucial in stimulating novel and paradigmatic shifts in our understanding. Even simple binary TMOs such as nickel oxide (NiO) can be deceivingly trivial. Band theory predicts that with Ni^{2+} (a d^7 ion) having a partially filled outer shell it would be a metal. In reality, however, it behaves as an insulator. Many new or alternative theories have evolved as a result of such "contradictions", some of which will be highlighted in 2.4. from interactions that cannot be understood solely from the behaviors of individual constituents [26].

2.2.2   Interactions between orbitals

The role of d-orbital electrons is closely related to how they interact with each other and their surroundings. The d-orbitals can host a total of 10 electrons, distributed between five orbitals of different symmetries, shown in Figure 2.3. In free space, these are degenerate in energy and the electrons will occupy them according to Hund's rules of maximizing spin and orbital angular

momentum. In a solid, however, the presence of ligands perturbs the once uniform surrounding by imposing a crystal field whose symmetry depends on the ligand coordination to the central atom. As a result, some orbitals will experience stronger repulsion from the ligand orbitals and be lifted to a higher energy, thus breaking the original degeneracy. The energy difference between the non-degenerate energy levels depends on the ligand's electrostatic field strength.
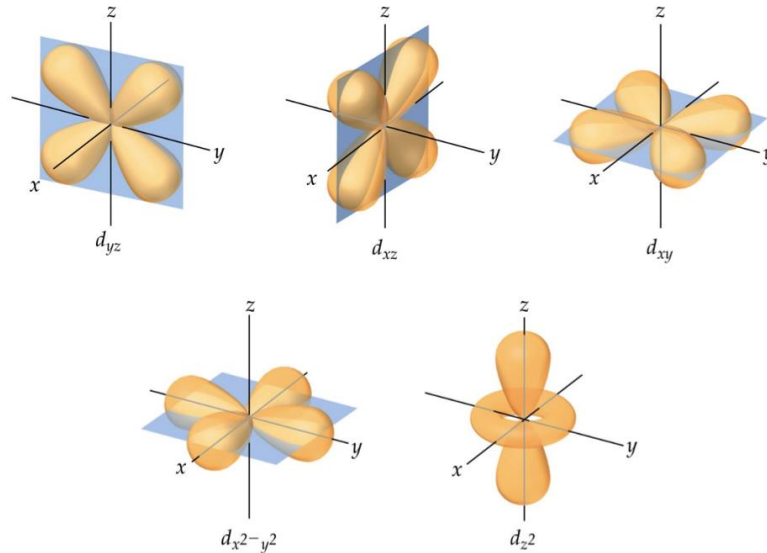
Figure 2.3 The spatial symmetries of the different d-orbitals. Reproduced from [28].

In TMO perovskites it is the interaction between oxygen p-orbitals and transition metal d-orbitals that lifts the degeneracy. Since the B-cation sits in a cage comprised of six oxygen ions, *i.e.*, octahedral coordination, the d-orbitals along the coordination system axes (e_g) will be repelled more strongly by the p-orbitals and end up with a higher energy than the t_{2g} orbitals. The two sets of orbitals (3 t_{2g} and 2 e_g) become separated by a crystal field splitting energy, typically denoted Δ_O.

Given the directionality of the interactions, there will be a more significant orbital overlap between oxygen p-orbitals and transition metal e_g d-orbitals, allowing them to hybridize. This effectively forces mobile electrons to move via intermediate oxygen ions [29], making electronic transport properties and magnetic exchange interactions sensitive to the d-p overlap and perturbations that can affect the overlap strength, *e.g.*, octahedral tilts and rotations. Essentially, this is equivalent to the discussion of the B-O-B bond angle where B is now a transition metal with d-electrons that have potential for strong electronic correlations. The result is that new or modified properties and behaviors often emerge in families of transition metal ABO_3 compounds. A notable example of this is the rare-earth nickelate series.

2.3   Rare-Earth Nickelates

2.3.1   The rare-earth nickelate phase diagram

The rare earth nickelates, RENiO$_3$, are a family of transition metal oxides in which Ni occupies the B-site and the A-cation is a trivalent rare-earth element, RE = {La, Pr, Nd, …, Lu} (also includes Sc and Y in some contexts). Rare earth nickelates have been a topic of considerable interest over the past decades owing to their rich phase diagram with multiple transitions of interest. All members except for LaNiO$_3$ display a remarkable metal-insulator transition that occurs concomitantly with a structural transition at the T_{MIT}. There is also a magnetic transition from paramagnetic (PM) to antiferromagnetic (AFM) that takes place at $T_{Néel} < T_{MIT}$, with the exception of NdNiO$_3$ and PrNiO$_3$ whose transitions occur at $T_{Néel}$ = T_{MIT}. LaNiO$_3$ is the only member that remains a paramagnetic metal at all temperatures. Finally, an optical transition takes place at the MIT, principally changing the materials from transparent (in the insulating state) to black (in the metallic state).

As can be seen in the phase diagram reproduced in Figure 2.4, the T_{MIT} increases from 0 to 600 K with decreasing rare-earth cation size (from La to Lu, respectively). This can also be parametrized using the Ni-O-Ni bond angle (top axis) or the Goldschmidt tolerance factor (bottom axis), with the relation being that smaller rare-earths (smaller t) require stabilization by structural distortions that manifest as octahedral rotations. Corner-connectivity is maintained, so rotations cause the Ni-O-Ni bond angle to deviate more from the ideal 180 ° and the orbital overlap that, for instance, enables electron hopping becomes reduced. Consequently, the nickelates with larger rare-earths and less distortions retain metallicity down to relatively low temperatures, whereas small rare-earth nickelates transition to the insulating state at higher temperatures.
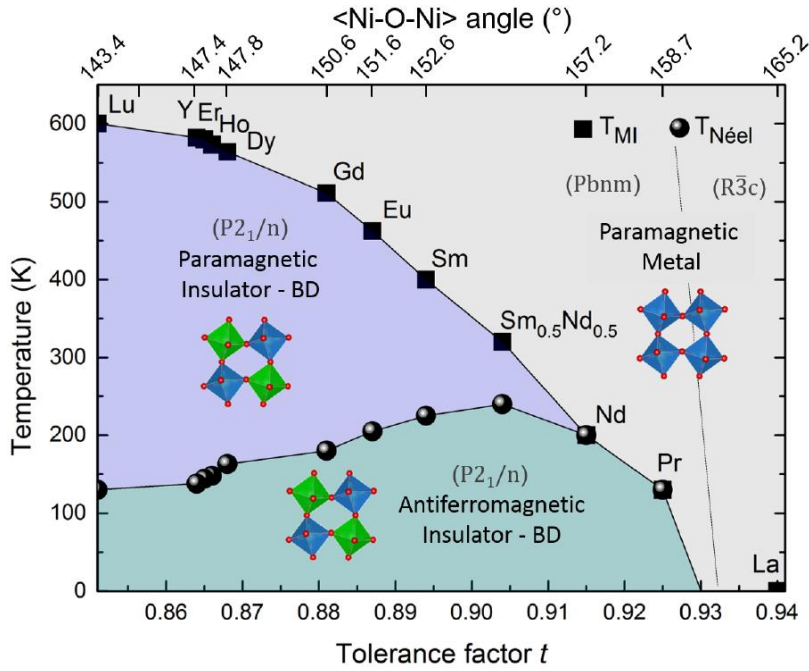
Figure 2.4 Phase diagram for the rare-earth nickelate family showing the structural, electronic and magnetic phases of the members at different temperatures. The metal-insulator transition and magnetic transition are parametrized by the structure's tolerance factor (bottom x-axis) and the Ni-O-Ni bond angle (top x-axis). Obtained from [5].

2.3.2 Description of the electronic, structural, and magnetic transitions

Since the transitions of interest in the rest of the rare-earth nickelates do not pertain to LaNiO$_3$, its exclusion from the following discussion will be implicit (even in cases that discuss the family as a whole).

Lowering the temperature across the T$_{MIT}$ triggers a simultaneous structural and electronic transition. In the high-temperature regime (> T$_{MIT}$), rare-earth nickelates crystallize in a metallic, orthorhombic phase described by space group *Pbnm*. The reduction in symmetry from the parent cubic aristotype arises as a result of anti-phase rotations of oxygen octahedra in the *x*- and *y*-directions, as well as in-phase rotations in the *z*-direction [30]. In Glazer notation this is denoted as *a⁻a⁻c⁺*. Nevertheless, it is common to use *pseudo*cubic (*pc*) notation that transforms the orthorhombic unit cell into a representative *pseudo*cubic one, with all vectors and lattice parameters related by a transformation matrix. This allows for more direct structural comparisons across different symmetries. For instance, the orthorhombic lattice parameters of NdNiO$_3$ are a = 5.389 Å, b = 5.382 Å, and c = 7.6101 Å, and this can be expressed as a$_{pc}$ = 3.807 Å. The latter is much easier to compare to SrTiO$_3$ (STO), a commonly used substrate with cubic symmetry and a = b = c = 3.905 Å.

At the T$_{MIT}$, symmetry is reduced from orthorhombic to monoclinic (space group *P2$_1$/n*) and the electronic transport regime evolves from metallic to insulating. The most distinct evidence of the latter is an abrupt change in the material's resistivity over several orders of magnitude. This often appears

in conjunction with hysteresis if the sample is both cooled and heated across the T_{MIT}, which is indicative of the first-order transition that the MIT is.

Observations of structural changes are more diverse. In addition to symmetry-lowering, a cooperative breathing mode has been observed to accompany the MIT [31, 32]. This appears as a three-dimensional checkerboard arrangement of alternately contracted and expanded NiO_6 octahedra, depicted in Figure 2.5. The activation of this breathing mode cannot be attributed merely to structural stabilizations, as was the case for the symmetry transition, but might be rooted in some complex charge-lattice interplay. Additionally, observations of a small and discontinuous increase in Ni-O bond lengths and overall unit-cell volume has been reported [33, 34]. This could be related to the appearance of bond-disproportioned Ni-sites leading to separate bonds of more ionic and covalent nature [35]. Distinguishing between primary driving mechanisms and secondary effects is truly at the heart of understanding the MIT and its associated transitions.
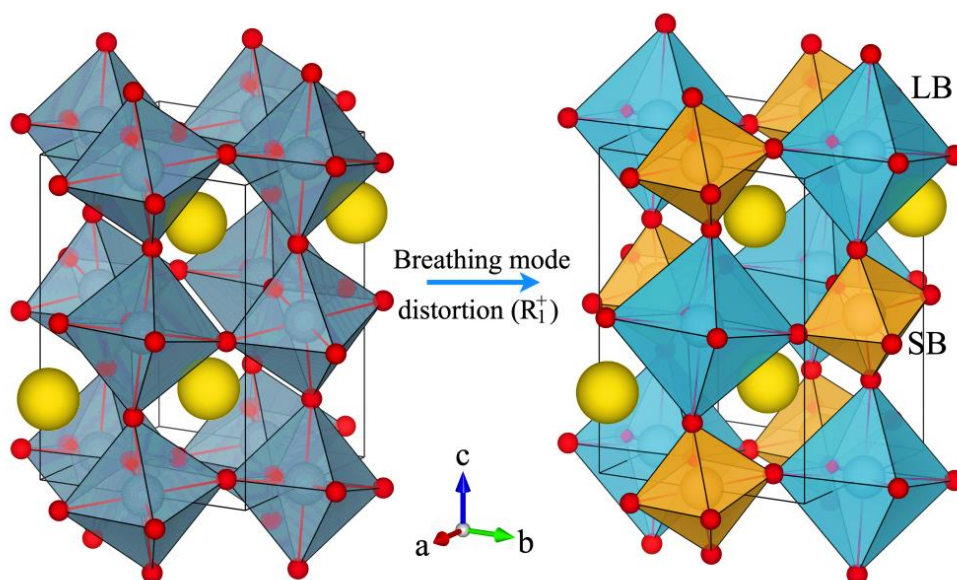
Figure 2.5 Activation of a cooperative breathing mode in a perovskite oxide. The structure adopts a three-dimensional checkerboard arrangement of alternately contracted (orange polyhedra to the right, SB = short bonds) and expanded (turquoise polyhedra to the right, LB = long bonds). Reproduced from [36].

The magnetic transition (paramagnetic to antiferromagnetic) is interesting in itself, and particularly for $NdNiO_3$ and $PrNiO_3$ whose onset coincides with the structural and electronic transitions. This has led to hypotheses concerning the contribution of magnetic interactions and ordering to the driving force for the MITs of these two compounds. Some suggest that magnetic ordering is at the heart of the transition – either driving it independently or completing what structural instabilities initiated [37]. The magnetic ordering in $NdNiO_3$ is certainly remarkable, but whether it plays such an integral role in the MIT or not has yet to be decided.

2.4 The Metal-Insulator Transition

2.4.1 Motivation and context for studying the metal-insulator transition

Despite being one of the most intensively studied phenomena in modern day solid-state physics [31], the MIT, and especially its origin, remains a highly debated phenomenon. The existence of three closely related transitions hints at a complex interplay (competition and/or cooperation) between energies of different degrees of freedom (orbital, charge, lattice, spin) that even decades of committed research has not been able to untangle. And yet, or perhaps *because* of this, the MIT has become widely recognized as fundamentally important. The reason why is two-fold.

On a philosophical level, the fact that the problem appears as unsolvable is tantalizing in itself. Our inability to explain the MIT with existing models and theories has revealed a gap in our collective knowledge; scientific inquiry becomes a quest to fill it. This resembles the decade-long debates on the fundamentals of superconductors, leading to numerous Nobel prizes over the course of the last century. In other words, studying the MIT is an opportunity to improve our fundamental understanding of the dynamics and interactions that drive it. The ripple-effects of obtaining such new-found knowledge would likely benefit other areas in solid-state physics, nanotechnology and maybe even quantum mechanics as well.

The other perspective relates to applied research. Regardless of the complexity of the underlying mechanisms, they may offer new strategies and tuning knobs for engineering the functionalities of these materials. There could, for instance, exist entirely different pathways for controlling one behavior through another than have been observed before. It has already been observed that external factors such as hydrostatic pressure [38], electric fields [39] and dynamic light control [40] can be used to tune the MIT, in addition to the more intrinsic effects of epitaxial strain [6, 41-44], isotope substitution [45], and chemical doping [46]. More important is the potential coupling between different influences; for instance, some claim that the sensitivity of oxygen non-stoichiometry to strain is universal in nickelates [47]. New strategies like these may even bridge different device technology through similar control parameters, enabling powerful and innovative ways to use them in conjunction.

2.4.2 Introduction to metal-Insulator transition theories

The pursuit of a comprehensive explanation for the driving force behind the MIT and the low-temperature ground state of the rare earth nickelates has generated a number of hypotheses, based on both experimental and theoretical work. With the evolution of new ideas and conclusions, some notions have grown stronger while others have branched off in a different direction or been rejected completely. The resulting network of theories is, to say the least, intricate.

Past and current work has mainly focused on two goals: 1) capture an accurate description of the low-temperature, insulating ground state adopted by all the rare earth nickelates (except LaNiO$_3$), and 2) explicating the driving force behind the MIT in terms of correlation effects and the various degrees of freedom that seem to be working in tandem. Although the initial approaches to these two objectives may differ, they are not really more different than the sides of a coin. To understand what triggers the MIT, it would be useful to know the characteristics (electronic structure, magnetic order) of the ground state it transitions to. In turn, knowing which parameters are integral to the mechanism and which merely accompany the transition could simplify the problem for both experimentalists and theoreticians. While there exists a number of theories for the insulating ground state, there is a general disagreement stemming from difficulties in reconciling various experimental observations as well as theoretical models. Much of this disagreement originates from the fact that the rare-earth nickelates do not conform to any of the traditionally proposed theories, such as the Mott-Hubbard model or the Zaanen-Sawatzky-Allen framework. Only recently has research seemed to reach what might resemble a form of consensus, classifying the rare-earth nickelates as site-selective Mott insulators. A brief account of the different observations that have been and the evolution of MIT theories is provided for the interested reader in Appendix 1A.1 since it is not directly relevant to this work.

This thesis does not aim to elucidate the MIT or contribute to the discussion on the side of fundamental understanding, but rather to study its potential through application-motivated research. It is, however, valuable to recognize the complexity of the system since this may hold the key to new and innovative strategies for tuning and controlling properties.

2.5   Thin films

In the world of thin films we enter the realm of heterostructure physics, where yet new factors contribute to the complicating mechanisms believed to underlie the MIT. There are primarily three effects one can expect to be present in a thin film that should be taken into consideration: substrate strain and orientation, interface dynamics, and depth-dependent variations due to relaxation. Many unpredicted and puzzling phenomena can be better understood against the backdrop of these influences and it is thus important to have a general understanding of them.

2.5.1   Substrate and strain

The substrate provides the initial surface that the thin film precursors see and interact with, and similar to a foundation's role for a building, serves as the template for the thin film's structure. If there are incompatibilities between the lattice parameters of the substrate and those of the film, they are typically resolved, if possible, by straining the unit cell of the film material. Given a cube-on-cube type
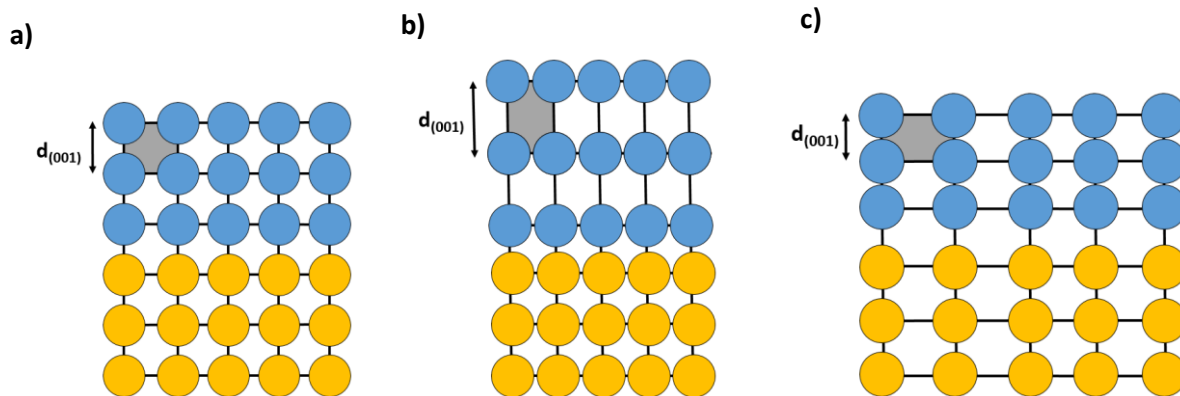
*Figure 2.6 Cartoon illustrating the effect of film-substrate lattice mismatch on the two-dimensional unit-cell volume (colored gray) and strain in the film. **a)** No lattice mismatch, the film is perfectly strained to the substrate. **b)** The substrate imposes compressive strain ($a_{sub} < a_{film}$), inducing elongation of the lattice in the out-of-plane direction. **c)** The substrate imposes tensile strain ($a_{sub} > a_{film}$), inducing compression of the lattice in the out-of-plane direction.*

of growth, the film will in this case adjust its structure so that it matches that of the substrate and adopt the lattice parameters spanning the base of the cube.

This leads to either compressive ($a_{film} > a_{substrate}$) or tensile ($a_{film} < a_{substrate}$) in-plane strain, which is typically compensated for by the converse responsive strain in the out-of-plane lattice parameter to maintain an as constant unit cell volume as possible (isovolumetric strain). Figure 2.6 demonstrates both of these cases. Depending on the degree of strain, it will propagate through the film until it exceeds the film's tolerance, after which it breaks up into domains to mitigate the energetic expense – a process termed relaxation.

The effects of strain can be understood by considering how it influences the material's structure. In addition to changing the lattice parameters of the thin film, the octahedra may rotate to adjust to the imposed distortion and stabilize instabilities regarding the cation positions. Consequently, the B-O-B bond angle and corresponding orbital overlap in perovskite oxides could be significantly affected by strain. These are often characteristic parameters for transport properties and magnetic exchange interactions, which is how strain can sometimes be effective in tuning the functionality of a thin film.

A crystalline film with a definite orientation relative to and dictated by the substrate is called *epitaxial*. Most often, this appears as biaxial alignment (in-plane and out-of-plane) with the substrate. Homoepitaxy occurs when the film and substrate materials are identical, while heteroepitaxy is between two dissimilar materials. For perovskite oxides, the latter is rather common owing to the structural flexibility and similarity between different types of perovskites. Often used in conjunction with these descriptors is the term *heterostructure*. In thin-film context this typically refers to structures that contain interfaces between layers of two (or more) distinct materials (could differ only by crystal orientation or structure).

2.5.2 Other thin film effects

In addition to lattice parameters (in terms of lattice mismatch), the substrate's crystalline orientation is also rather important. It has been found that the MIT in the rare-earth nickelates can be tuned by growing the film on substrates of different orientations (*e.g.,* $NdNiO_3$ on $NdGaO_3$(100) vs. $NdGaO_3$(111) [48]). A postulated reason is that the orientation determines which connectivity the octahedra of the exposed surface has, and this imposes different epitaxial requirements. For instance, along the (100) plane, connectivity is realized through a single apical oxygen, whereas each octahedron shares three oxygen atoms in the (111) plane. The latter is a much stricter constraint that affects the degree to which octahedra can distort through rotations.

Finally, interface effects between two materials can play an important role that should not be disregarded. This could entail symmetry breaking, depth-dependent variations in charge that can lead to surface reconfiguration, or proper charge transfer, in addition to bonding mismatches.

The numerous and at times unpredictable dynamics at play at an interface can give rise to new behaviors and exotic properties. It is not without reason that Herbert Kroemer, winner of the Nobel prize in Physics in 2000, started his Nobel lecture by saying that "*often, the interface is the device*". In this realm of heterostructure physics there are many concepts yet to be understood, and these may further our ability to tune, control and engineer effects that may not even exist in any other form or at any other place.

3 Methods

The various methods used in this work are introduced in this chapter. It begins with a theoretical survey of ALD before elaborating on some aspects of it that provide an important backdrop to the results. The characterization methods are then explained.

3.1 Atomic Layer Deposition

ALD is a chemical vapor deposition-based method that relies on self-limiting gas-surface reactions to grow thin films. As opposed to other physical deposition alternatives, such as pulsed layer deposition or molecular beam epitaxy, ALD circumvents the need for high temperatures, pressures, or voltages by instead relying on the chemical reactivity of the reactant species, called *precursors*. This has the added benefit of enabling depositions of metastable systems that may otherwise be incompatible with other deposition methods. Moreover, line-of-sight to the substrate is not required since the chemical surface reaction does not depend on the physical path of the precursor and this makes ALD superior in terms of pinhole-free step coverage of non-uniform substrates.

There are primarily three hallmarks for which ALD has become known and that make it excel:

- Conformal and uniform films, even on complex substrate geometries and high-aspect ratio substrates
- Atomic-scale control of thickness
- Low substrate temperatures

Because the growth of each layer is self-limited by chemistry, it is possible to control the thickness of the thin film down to the atomic scale, resulting in the layer-by-layer control that ALD has become known for. This has been further enhanced by the advancement of state-of-the-art technology such as *in-situ* quartz crystal microbalances or ellipsometry that enable monitoring of the film growth during deposition.

It would be natural to infer from this that ALD growth happens monolayer by monolayer; however, this picture is not entirely accurate. Even when assuming complete saturation of the surface, steric effects of the ligands will hinder precursor molecules from reaching all active sites. Any single binary reaction cycle therefore deposits a sub-monolayer of material, meaning the growth per cycle (GPC, per cation pulse) is less than a full monolayer. This does not preclude the ability to grow dense and uniform films, however, because the unreacted active sites will be exposed to subsequent pulses. Nevertheless, it means that it becomes important to consider how the different chemistries of the surface can affect the material composition, structure, and properties. This forms the basis of part of the discussion in 3.1.4.

3.1.1 The atomic layer deposition process

The ALD process consists of sequential steps (cycles) that are repeated in a cyclical manner to grow the film with the desired thickness. Differing from traditional CVD, every precursor is pulsed separately into the reaction chamber, with a purging step to remove any excess following each pulse, thus limiting gas-phase reactions between different precursors. These pulsing steps are then combined in a sequence that caters to the desired structure and the individual growth parameters for the precursors.

A common illustrative example is the deposition of Al_2O_3 thin films from trimethylaluminum (TMA, $Al(CH_3)_3$) and H_2O, which has a well-established and extensively tested ALD recipe. The general process is executed in the steps outlined below, which correspond to the cycle in Figure 3.1.
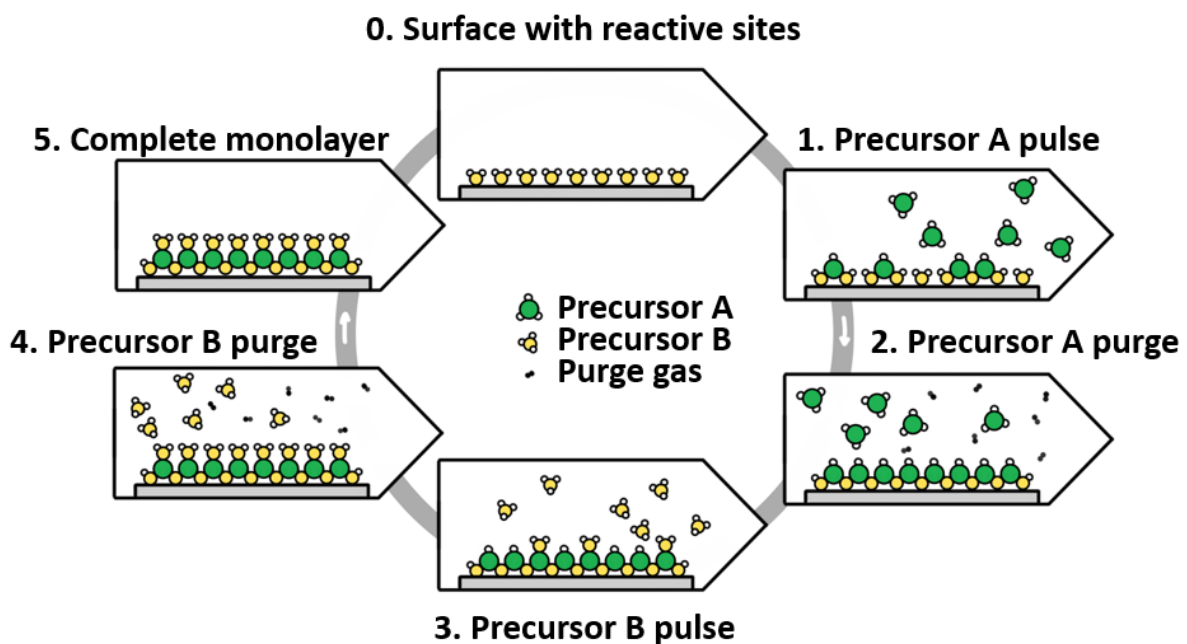
Figure 3.1 Illustrated steps in a generalized atomic layer deposition cycle for a binary oxide A_xB_y, for example Al_2O_3. The cycle consists of consecutive pulses and purges of each precursor, with self-limiting growth on the surface leading to sequential growth of monolayers. Created by [49]

0. The surface onto which the next thin film layer will be deposited.
1. Precursor A pulse. Precursor A (TMA) is pulsed into the reaction chamber and reacts with the available functional groups on the surface (substrate if first pulse).
2. the reaction chamber to carry away any excess precursor A and potential reaction by-products.
3. Precursor B pulse. Precursor B (O_3) is pulsed into the reaction chamber and undergoes the same *process* as precursor A.
4. Precursor B purge. A purge step removes excess precursor B and reaction by-products.
5. The cycle is considered complete because the next pulse (of precursor A) will see an environment similar to that in the first step and the remaining deposition can be completed by repeating steps one through four.

The approach to binary oxide processes can be combined to grow ternary and quaternary oxide thin films as well. The binary oxide processes then become subcycles in a larger supercycle that encompasses the entire sequence of the deposition. Depending on how many times a single subcycle is repeated and how often it switches from one subcycle to another, the chemical and physical structure of the film can be varied.

It is essential to ensure complete saturation of the surface with each precursor pulse; otherwise, non-uniform growth with thickness gradients will occur. Pulse durations are empirically determined as they depend on experimental parameters such as precursor sublimation temperature, substrate deposition temperature, gas flows, etc.

When the surface has become saturated, all active sites not overshadowed by steric effects have reacted with the precursor (co-reactant) layer and this leads to the self-limiting growth characteristic of ALD processes. Nevertheless, self-limiting growth is not inherent to ALD in the way that it occurs regardless and it very much depends on the properties and chemistries of the selected precursors. Much of the key to improving existing or developing new ALD processes therefore relies on identifying suitable precursor combinations that have self-limiting surface reactions.

3.1.2 Precursor characteristics

Precursor characteristics are particularly significant for ALD since the composition of the film, and thus its properties, are determined by precursor chemistry and reactivity. Certain attributes may be more suitable than others depending on the desired outcome, but generally an ideal precursor satisfies many of the following set of characteristics, where conditions i.-iii. are more stringent:

i. Sufficient reactivity with sites on the substrate and other precursor species, but inert towards itself
ii. Moderately high vapor pressure at applied temperature (volatility)
iii. Thermal stability at deposition temperature (so as not to decompose)
iv. Non-toxic
v. High density aggregate state (occupies less volume)
vi. Readily available, either from lab synthesis or commercially

Water (H_2O) is the simplest ideal precursor that exists and is standardly used as the oxygen carrier for depositions of metal oxides. However, ozone may be required in processes where water has too low reactivity or where it may result in water reservoir effects, *e.g.,* when the resulting film is hygroscopic [50].

This work uses β-diketonates, a class of metalorganic precursor, with two different types of ligands: *thd* (2,2,6,6-tetramethylheptane-3,5,-dionate) and *acac* (acetylacetonate, pentane-2,4-dione).

Depositions of the β-diketonates must occur with ozone as the oxygen source due to their poor reactivity with water. Ni(acac)$_2$ is known to be hygroscopic and it is therefore important to use it as dehydrated to avoid uncontrolled reactions.

The metal-oxygen bond strength for the thd- and acac-ligands can be estimated from the ligands' pKa values: 8.79 for H(acac) [51] and 11.6 for H(thd). It is therefore natural to assume that the metal-oxygen bonds for thd-based complexes are stronger, and hence, less reactive than acac-based ones.

The structural similarities and differences between the acac- and thd-ligands are of importance to the growth dynamics during depositions and are graphically compared in Figure 3.2. The acetylacetonate anion, (acac)$^-$, has a 5-carbon backbone with a methyl group at each end and is a bidentate ligand, in which the two oxygen atoms (red spheres in Figure 3.2a and b) bind to the metal. thd is similarly bidentate, but is larger overall with its three methyl groups at the ends, denoted as tert-butoxide (tBu) in structure drawings.
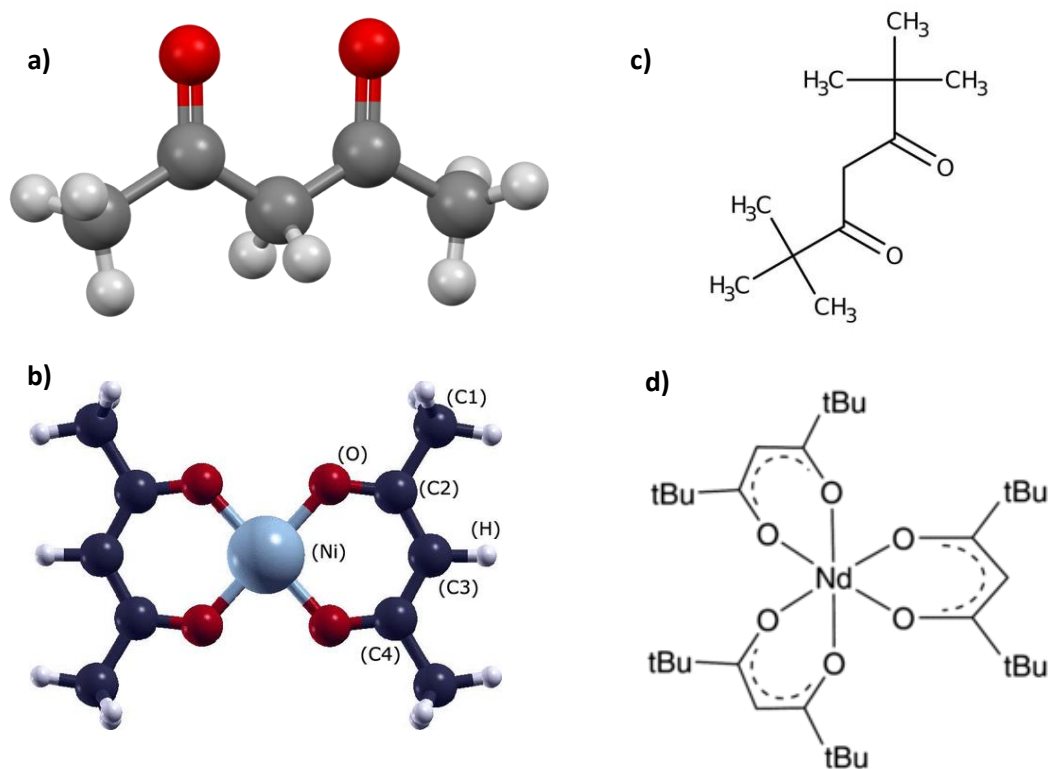

Figure 3.2 Chemical structure drawings of the ligands (top row) and full precursors (bottom row) used in depositions of NdNiO$_3$. ***a)*** *The bidentate ligand acetylacetonate (acac), from [52].* ***b)*** *Ni(acac)$_2$, from [53].* ***c)*** *The bidentate tetramethylheptane dionate (thd) ligand.* ***d)*** *Nd(thd)$_3$.*

3.1.3 Comments on the atomic layer deposition temperature window

Self-limiting growth through chemical saturation of the surface is a defining ALD feature that distinguishes it from other deposition methods. In conventional ALD literature, another characteristic is also credited with the same status: the *ALD temperature window.* The premise is that a process can be regarded as ALD if there exists a temperature range ("window") over which the GPC remains constant. At temperatures above or below this various processes can disrupt ideal ALD growth. While such effects should be minimized to the greatest extent possible, it is misleading to claim that self-limiting growth cannot take place without having a constant GPC in this temperature window [54]. It is arguably more instructive to consider how these temperature-dependent factors can influence growth and saturation for any individual system. A brief outline of the arguments follows below.

A decreasing GPC upon lowering temperature is ascribed to incomplete reactions at the surface. However, from neither a thermodynamics nor kinetics point of view is there reason to believe that the GPC would be linearly dependent on temperature. Longer precursor pulses should be able to mitigate slower, kinetically dependent reactions as long as the temperature is high enough for molecules to overcome the initial activation energy.

Condensation is used to explain how GPC at low temperatures can be higher than expected. However, this is only reasonable if the deposition temperature is lower than the sublimation temperature of the precursors, which it should not be in traditional ALD instrumentation.
Thermal decomposition at excessively high temperatures is a more probable concern and is well-known in CVD, in which deposition temperatures are generally higher. Excessively high temperatures can cause the precursor to decompose or not dissociate from its ligand, or the oxide can be deposited as normal but in a non-uniform manner since it is no longer the reactivity of the surface that dictates precursor-surface reactions.

The GPC can also decline at excessively high temperatures due to desorption. In an ALD process, irreversible chemisorption is generally considered a requisite for self-terminating growth [55]. Desorption of physisorbed species may cause saturation to slow down at higher temperatures but should ideally be limited by the precursor's affinity for the surface.

The effects of deposition temperature are not discounted, as it is decidedly an important parameter to consider. However, it seems to have become so engrained in ALD literature that the underlying dynamics that truly characterize successful ALD are easy to neglect or forget about. Above all, the interplay between temperature and saturation conditions should be at the center of optimizing an ALD process, and this may entail paying equally much attention to the behavior of precursors in different conditions as to identifying the ALD window alone.

3.1.4   Ternary atomic layer deposition and subcycle arrangement

The general ALD process outlined in Figure 3.1 illustrated the deposition steps for a binary oxide (Al_2O_3), which is the most traditional chemistry in ALD. There is, nonetheless, a growing interest and realization of ternary, quaternary, and even some quinary oxides that have wider diversity of properties with greater technological relevance.

The challenge with multicomponent systems is that their complexity increases rapidly. Going from one metal, as in Al_2O_3, to two, as in $LaAlO_3$, is simple in theory, but difficult to execute with the same control as for the binary oxide processes. Factors such as nucleation delay (due to switching processes) or precursor ligand interactions often come into play, unpredictably affecting growth characteristics of the complex oxide. This occurs because the reaction of a precursor varies for different chemical surfaces [56], and the reactive sites differ in binary and ternary processes. For example, in the deposition of $NdNiO_3$ with $Nd(thd)_3$- and $Ni(acac)_2$ pulses that do not simply alternate every time, the first pulse will see the surface of the other binary oxide, while consecutive pulses will see increasingly more of "its own" oxide. Such non-idealities complicate the behavior of the ternary system, often causing its growth rate and composition to deviate from being a linear combination of the growth rate and composition of the binary processes.

The most common strategy for depositing a ternary oxide is presumably the supercycle approach, which combines several binary cycles into a supercycle. The general philosophy is to deposit binary oxide layers in such a way that the atoms can intermix and form the ternary structure. An example that pertains to this work specifically can be found in Table X. The process might seem trivial, as it is only a matter of stacking binary oxide layers; however, the structure of the supercycle, in terms of precursor order and cycling ratio (between binary oxide cycles), not only dictates the composition of the film, but also its structure and properties.

This can be understood by considering the differences between the two most common supercycle variants. In the homogeneous approach, intermixing is promoted by frequently alternating between the binary processes. To exemplify, a supercycle consisting of La_2O_3 and NiO can switch between the binary processes after every single layer for a given number, n, of total cation pulses: $n\times \{[La(thd)_3 + O_3] + [Ni(acac)_2 + O_3]\}$. While this facilitates intermixing (the reaction takes place on a mixed cation surface because the previous layer is not completely dense [56]), it often leads to amorphous films that require annealing to become crystalline. This is because intermixing introduces structural chaos that makes it difficult for the constituents to arrange in the ternary oxide structure.

At the other end of the spectrum of is the multilayer approach, in which one or more binary processes are repeated enough times (high bilayer period) to deposit a multilayer, or lamellar-like, structure. Modifying the example from before, it can take the form of, $\{40 \times [La(thd)_3 + O_3] + 16 \times$

$[Ni(acac)_2 + O_3]$ }. To deposit the same number of total cation pulses, the total number of supercycles would have to be reduced. This approach reduces the nucleation effects that the homogeneous approach is prone to but, owing to the relatively low temperatures utilized in ALD, relies on post-deposition annealing to assist intermixing and ternary phase formation.

Recent efforts put into evaluating these effects suggest that they could become valuable in the ALD toolkit. A particularly important aspect of it concerns the spatial distribution of atoms, as determined by the deposition structure and order.

With the aim of identifying the best platform for crystalline growth, Sønsteby *et al.* [57] found that the sweet spot for the subcycle arrangement, *i.e.*, how the different binary subcycles are ordered, seems to be a combination of the two approaches. By depositing multilayer slab thicknesses close to the target structure's interlayer distance, the as-deposited crystallinity and functional properties of $LaNiO_3$ were enhanced. This occurred without significantly influencing the chemical composition, which remained within a range of 50-55 cation % Ni^{3+}. They hypothesize that it is the resemblance between multilayer slab thickness and intrinsic bond distance in the structure that allows an easier transformation to the ternary phase.

An important implication of this is that when epitaxy is the desired outcome, alternative pulsing regimes derived from multiplying the stoichiometric ratio should be explored in addition to a "regular" composition range. This is a matter of optimizing growth conditions to promote the most ideal structure, without significantly changing the overall composition. Such small adjustments represent one of the control knobs that exists in ALD to finely optimize important parameters.

3.2 Characterization Methods

3.2.1 Optical characterization: spectroscopic ellipsometry

Most ordinary light is unpolarized, meaning that its mutually perpendicular vectors, the electric field component and the magnetic field component, oscillate randomly in the plane perpendicular to the propagation direction. One way to polarize light is by reflecting it off a surface so that there is a 90° angle between the incident and refracted beam, which occurs at a special condition for the incident angle called the Brewster angle.

In spectroscopic ellipsometry (SE), linearly polarized light emitted from the source head undergoes electronic interactions with the film that change the phases of the electric field components, causing it to emerge as elliptically polarized [58], depicted in Figure 3.3. These changes can be represented by Fresnel coefficients (p and s for parallel and perpendicular, respectively) , whose amplitude ratio and phase difference provide information about optical constants and film thickness. SE is an indirect characterization technique that measures relative changes rather than absolute intensity. It is sensitive to even nanometer-thick samples, making it exceptionally well-suited for thin films. It also means that the optical response of the sample can only be derived by performing a model analysis on the experimental measurements [59]. One of the most commonly employed dispersion models in ellipsometry, and which was used in this work, is the Cauchy model. This describes the relationship between refractive index n and wavelength λ as $n(\lambda) = A + \frac{B}{\lambda^2} + \frac{C}{\lambda^4}$, where A, B and C are optical fit parameters [60]. In addition to optical constants it is possible to obtain precise measurements of film thickness and surface quality using SE. The fact that it's a non-invasive and non-destructive technique with a relatively simple instrumental setup makes SE a preferred optical characterization method for fast surveys of the thickness and refraction index of layered samples.
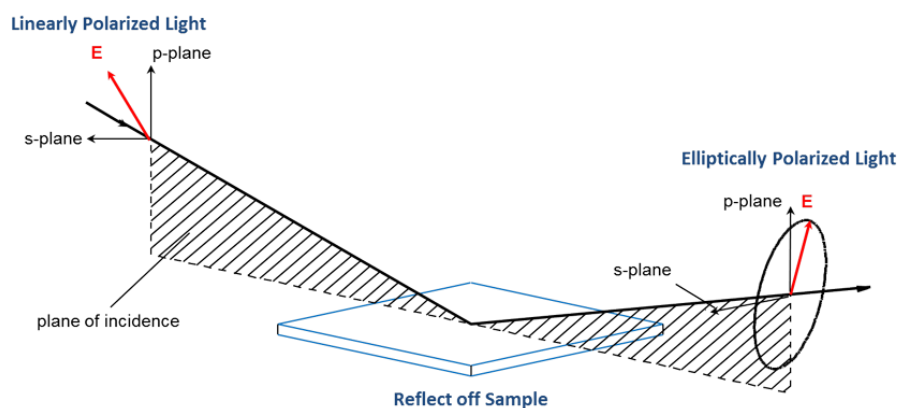

Figure 3.3 The main principle of spectroscopic ellipsometry. Incident, linearly polarized light interacts with the sample and is reflected as elliptically polarized. The relative change in the electric field components can be used to derive information about thin film thickness, refractive index, and absorption coefficient. Picture obtained from [61].

3.2.2   X-rays for materials characterization

X-rays have become a vital/essential radiation source in numerous characterization methods owing to the energy (wavelength) range they occupy in the electromagnetic spectrum. With a wavelength on the same order of magnitude as interatomic distances in a lattice it is possible to discern the spatial arrangement of atoms in a crystal structure, which is essential for structural analyses. For instance, they may be used to determine crystal structure and crystallite size (X-ray diffraction, XRD), probe surface roughness and density profiles (X-ray reflectivity), and study electronic and geometric structure (X-ray absorption spectroscopy). Additionally, the X-ray energy is comparable to that of an atom's electron energy levels, which can be utilized in electronic interactions with a specimen to reveal chemical information such as average elemental composition (X-ray fluorescence, XRF) or binding energy and oxidation state (X-ray photoelectron spectroscopy, XPS). The fact that X-rays are typically non-destructive for the sample is one of the reasons X-ray techniques are a standard go-to characterization method.

X-rays tend to have a relatively long penetration depth, which can pose a challenge for thin films. However, so-called grazing incidence X-ray diffraction measurements circumvent this problem by directing the X-rays nearly parallel to the sample surface to tune the penetration depth. Many recent advances further showcase the full potential of X-rays for characterization, including X-ray absorption near edge spectroscopy (XANES) and extended X-ray absorption fine structure (EXAFS). Since these are not pertinent to the task at hand, they will not be described here.

3.2.3   Chemical characterization: x-ray fluorescence and x-ray photoelectron spectroscopy

X-ray fluorescence

X-ray fluorescence is a spectroscopic characterization method in which the emission of fluorescent ("secondary") X-ray photons is used to analyze the (average) chemical composition of a specimen. An X-ray source is used to generate continuous and characteristic radiation that is directed towards a sample of the material. If a photon has sufficient energy (greater than the sample's ionization energy) it will excite a core electron and, in the process, leave behind a vacancy/hole, as illustrated in Figure 3.4. This leaves the ionized atom in a metastable state – one that can be mitigated by filling the vacancy with a higher-energy level electron. In doing so, the corresponding energy difference is released either as a photon that can be detected (XRF) or as radiation that immediately ionizes a valence electron, called an Auger electron (used in Auger electron spectroscopy, AES).

In the case of the former, the energy of this radiation is directly proportional to the energy difference associated with the transition (taking into account the work potential). Since the allowed transitions are governed by quantum mechanical selection rules, these energies are unique to each element (overlap is still possible) and can thus be used to identify a contributing element by Moseley's law:
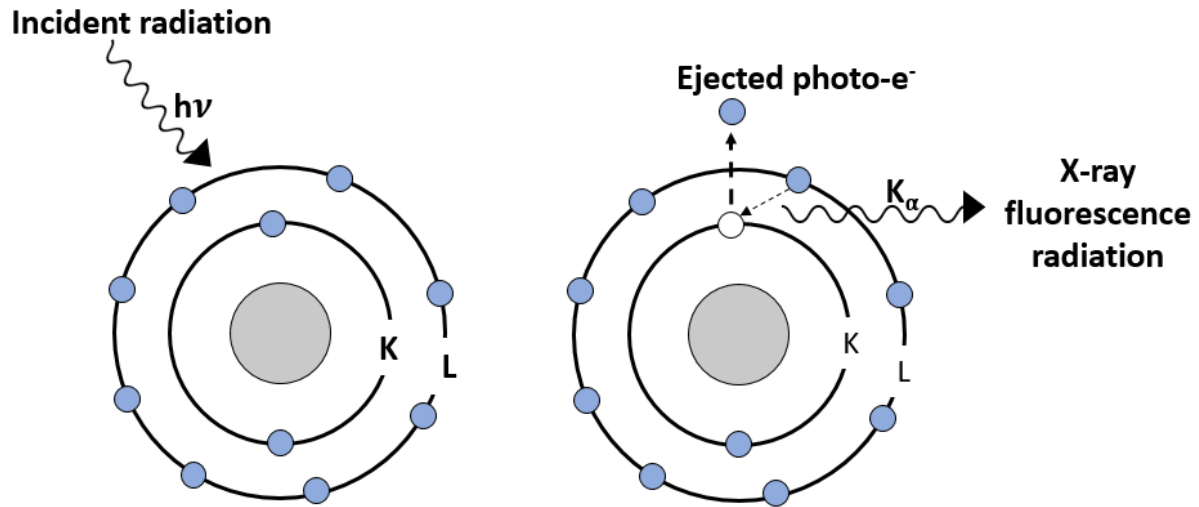
$$\frac{1}{\lambda} = K(Z - \sigma)^2,$$

Figure 3.4 X-ray fluorescence analyzes the chemical composition of a sample by stimulating the emission of x-ray fluorescent radiation, whose energy depends on the electronic transition and characteristic of the element it was emitted from.

where K and σ are constants and Z is the atomic number.

The dependence on Z/atomic number also has a practical implication: fluorescent X-rays from elements lighter than Na are generally too low in energy to be detected. However, apart from that, the relative intensities of the obtained spectrum are directly proportional to the relative amounts of each element in the material, which is how the average composition can be determined from XRF-data.

X-ray photoelectron spectroscopy

X-ray photoelectron spectroscopy is a photoemission spectroscopy that resembles XRF in several ways. Both methods use incident X-rays to induce a "response" in the sample, from which the elemental composition can be determined. With a penetration depth of ~1 μm (compared to an element-dependent depth that can range from μm up to as much as cm in XRF), XPS is primarily considered a surface-sensitive technique. However, it does offer some additional abilities that can make it more powerful/valuable for certain purposes. In addition to elemental composition, XPS can also be used to derive the chemical state and environment of a specific element, as well as the material's electronic structure.

XPS makes use of the photoelectric effect in the following way. By irradiating the sample with X-rays of a known energy (E = hv), some electrons will gain enough energy to overcome their binding energy, E_B, (the energy needed to bring an electron the Fermi level) as well as their work potential (material specific, bringing the electron from the Fermi level to the vacuum level, and keep it there). These electrons then leave the material with a kinetic energy of E_K, which is measured by the XPS detector.

This process is captured by the photoelectric effect equation, from which the binding energy can be derived and used to identify the element:

$$E_K = h\nu - E_B - \Phi$$ Eq. 2

3.2.4   Structural characterization: x-ray diffraction and reciprocal space mapping

Reciprocal space

The notion of reciprocal space has been highly convenient/effective for the treatment of crystal lattices and their related phenomena, such as diffraction. While principally a mathematical result of the Fourier transform of the crystal lattice, it also provides a useful tool for conceptualizing the physical process of diffraction.

The application of reciprocal space is most relevant *for* the holy triad comprising the Bragg equation, the Ewald sphere (a two-dimensional version of Bragg) and the Laue condition. As a side note, reciprocal space is commonly also referred to as momentum space, angular space, or k-space, but the relations between each are outside the scope and relevancy of this thesis.

X-ray diffraction

XRD utilizes elastic scattering of X-rays by electrons to reveal microstructural information about crystalline compounds. When atoms are arranged in a periodic array, such as a lattice, waves will be coherently scattered in a regular pattern and this may result in constructive (in-phase) or destructive (out of phase) interference. Amorphous materials lack this periodicity and therefore cannot be structurally characterized using XRD.

Whether constructive or destructive interference occurs depends on the difference in path length travelled by two interfering waves (reflected from different planes in the lattice). If the difference is an integer (half-integer) number of wavelengths, then waves will interfere constructively (destructively). The mathematical condition for this is stipulated through Bragg's law of diffraction: $n\lambda = 2d\sin(\theta)$, and is shown geometrically in Figure 3.5. Here λ is the X-ray wavelength, θ the angle between the incident X-ray and the atomic plane, d the interplanar distance, and n the order of reflection (integer number).

For a powder sample without preferential orientation, it can be assumed that the crystalline grains statistically are oriented in all possible directions. In this case there will for all families of crystallographic (hkl) planes in a phase be some angle that satisfies the Bragg condition, yielding a diffraction peak. If there is preferential orientation, however, crystal planes with particular orientations might be favored and appear more prominent (intense) in the diffractogram than is representative of the actual sample. Since powder diffraction is often used to identify phases of a

material through their diffraction "fingerprint", preferential orientation is advised against and avoided during sample preparation.
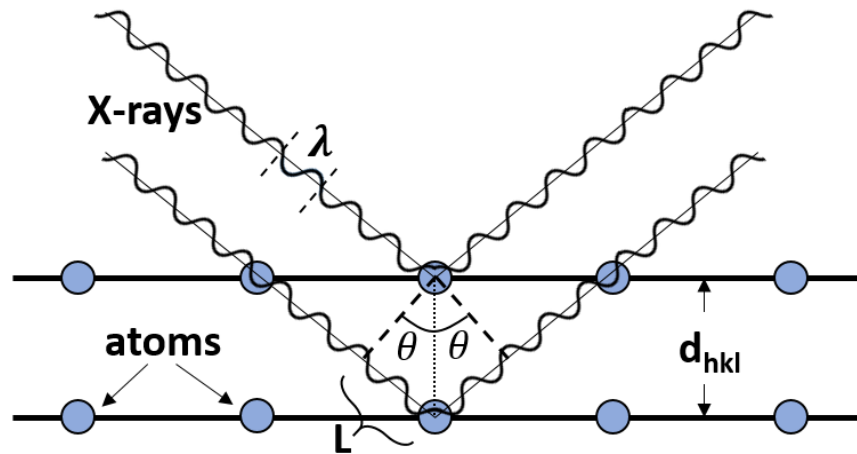

Figure 3.5 X-rays diffracting at atomic planes according to Bragg's law. Constructive interference occurs when the path difference, 2L, is an integer multiple of the wavelength, λ.

Sometimes, however, that is not really possible or even beneficial. Thin films always exhibit preferential orientation to some extent, assuming they are not amorphous. This is because the structural template of the substrate dictates the orientation of thin film growth, *e.g.*, the [001]-direction. If epitaxial growth is the desired outcome, as it often is, then evidence of well-aligned crystal planes would be a goal in itself.

It is important to be aware of how this affects thin film diffractograms, especially when performed with a powder-diffraction setup. Under symmetric conditions, as in Bragg-Brentano geometry (θ-2θ), the scattering vector, labeled $\vec{Q}$ in Figure 3.6, is always perpendicular to the sample surface owing to the coupled movement of source and detector. Therefore, only out-of-plane oriented planes (*i.e.*, they are parallel to the sample surface) will fulfill the Bragg condition and appear in the diffractogram, while others consistently do not contribute to scattering.

If a sample is polycrystalline, then individual grains/domains may be oriented such that crystal planes that are not strictly out-of-plane oriented still scatter to the detector. Conversely, a single-crystalline sample (or one that consists of grains with the same orientation) will only have reflections in the diffractogram that result from out-of-plane oriented crystal planes. Two examples are compared in Figure 3.7. The latter is typically a good indicator of single-oriented films because out-of-plane orientation seldom occurs without the substrate being epitaxially related to the substrate. However, the in-plane relationship can only be inferred from a θ-2θ scan and must be assessed independently through other methods, such as reciprocal space mapping (RSM).
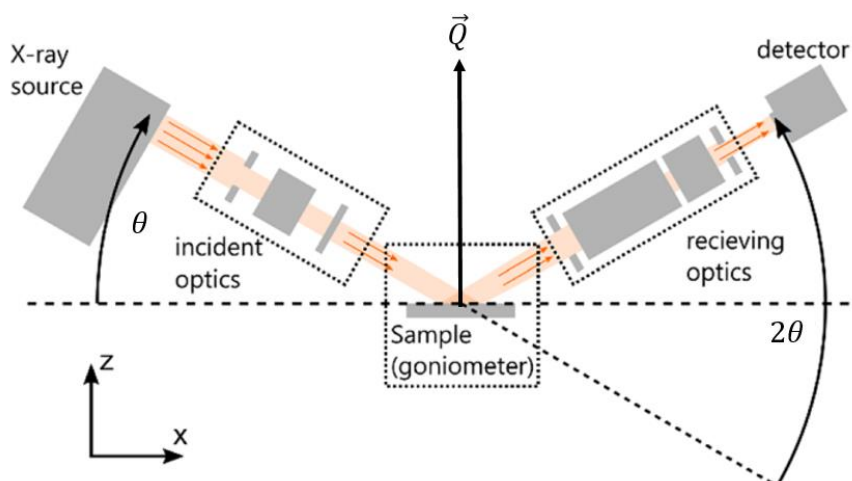
Figure 3.6 Diffraction components and set-up in the Bragg-Brentano (θ-2θ) geometry. Due to the coupled movement of source and detector, the scattering vector $\vec{Q}$ remains perpendicular to the surface throughout the scan. Reproduced from [62].
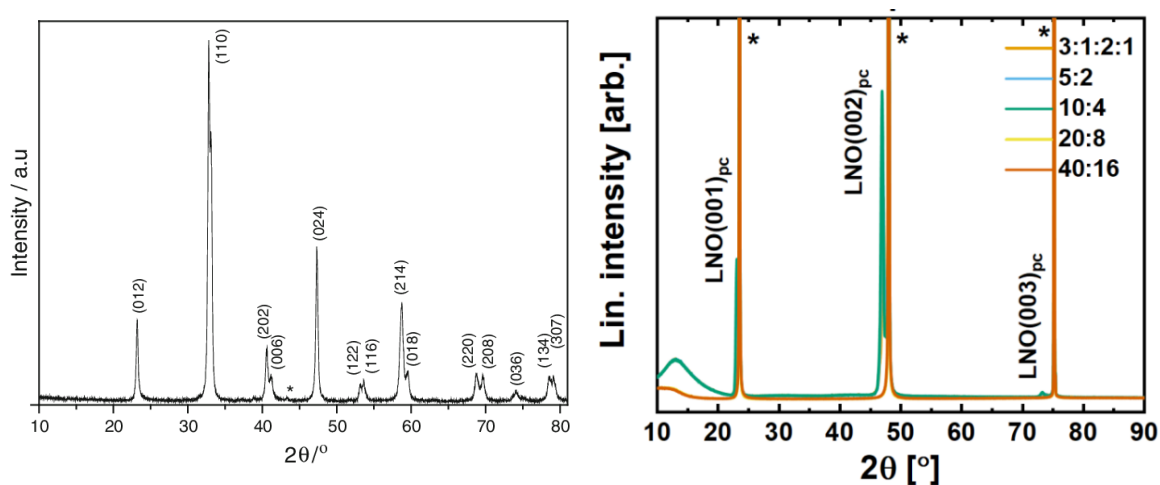
Figure 3.7 $\theta - 2\theta$ diffractograms for powders [63] (right) and single-oriented thin films [57](left) of LaNiO₃ to demonstrate the subset of Bragg reflections that appear for samples with preferred orientation. Owing to symmetric conditions in the Bragg-Brentano geometry, only out-of-plane oriented crystal planes generate Bragg reflections. In epitaxial films all crystallites have the same orientation and only one crystal family appears in the diffractogram; meanwhile, a polycrystalline film will have many more reflections as a result of several possible crystal plane orientations satisfying the Bragg condition simultaneously.

Reciprocal space mapping

To assess both in- and out-of-plane alignment, it is useful to map out a section of reciprocal space that contains non-specular reflections, meaning not only from planes that are parallel to the surface. As its name conveys, reciprocal space mapping does exactly that. It enables diffraction data to be collected

31

around whichever reflection(s) is/are available (sometimes limited by instrumental angular ranges) and produces a two-dimensional diffractogram with the intensity as a function of both $Q_{\parallel}$ and $Q_{\perp}$.

The general procedure for obtaining a reciprocal space map consists of three main steps. First, the instrument is calibrated to the sample, adjusting the sample stage height and the initial source and detector positions. Then the position of the chosen reflection must be calculated with respect to the three angles used to parametrize reciprocal space, graphically defined in Figure 3.8. Practically, this means setting the appropriate 2θ-angle between source and detector and performing a 360 ° survey scan around the ϕ-axis (perpendicular to surface) to determine the corresponding ϕ-angle for the reflection (as well as check the alignment of the system). The ϕ-scan will show a number of maxima that depends on the number of in-plane variations of that reflection for the sample's crystal symmetry and out-of-plane orientation. With the angular parameters set, the instrument is ready to measure diffraction intensity over a small range of 2θ for a given value of ω, which is gradually adjusted within a set range.
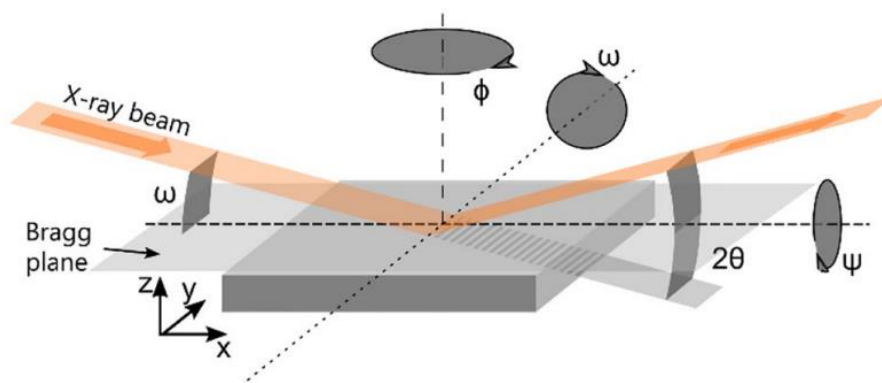
Figure 3.8 Definition of relevant angles for a reciprocal space map scan. The φ-axis is perpendicular to the sample surface, 2θ is the angle between source and detector, and ω is varied gradually throughout the measurement. Refer to the text for the relation between these. Figure reproduced from [62].

3.2.5 Electrical characterization: four-point probe and physical property measurement

Four-point probe for resistivity measurements

The four-point probe is a commonly used instrument for determining the electrical resistivity (or resistance) of a material. Based on the same principles as the two-point probe, this method gives more accurate results by separating the sense and source connection. In this setup, a current is sent between the two outer probes while the voltage is measured across the two inner probes. By themselves, the two voltage probes draw an insignificant amount of current, thereby eliminating the electrical contact resistance of the wires [64]. This makes it possible to separate the added, parasitic resistance from the true, intrinsic resistance of the material.

The four-point probe typically measures the sheet resistance, which is the lateral resistance across the length of a theoretical (imaginary) square. A more useful quantity to obtain is the inherent electronic property of resistivity (bulk), related to the sheet resistance by the film thickness: $\rho = R_s t$. From the voltage difference ΔV and current I, the resistivity can be deduced for a film of thickness t:

$$\rho = \frac{\pi t}{\ln 2} \frac{\Delta V}{I}$$

Resistivities were measured with a confidence limit of 2 V, above which a reading would be considered invalid. A correction factor that takes into account the geometry of the sample could give more accurate results [65], but are not as important for experiments where relative (qualitative) changes are the main feature of interest.

A four-point probe instrument was further developed (in house) to be able to measure temperature-dependent resistivities from room temperature and up to 300 ℃. It was first tested and made use of for this thesis work. The experimental setup is shown in

Figure 3.9.
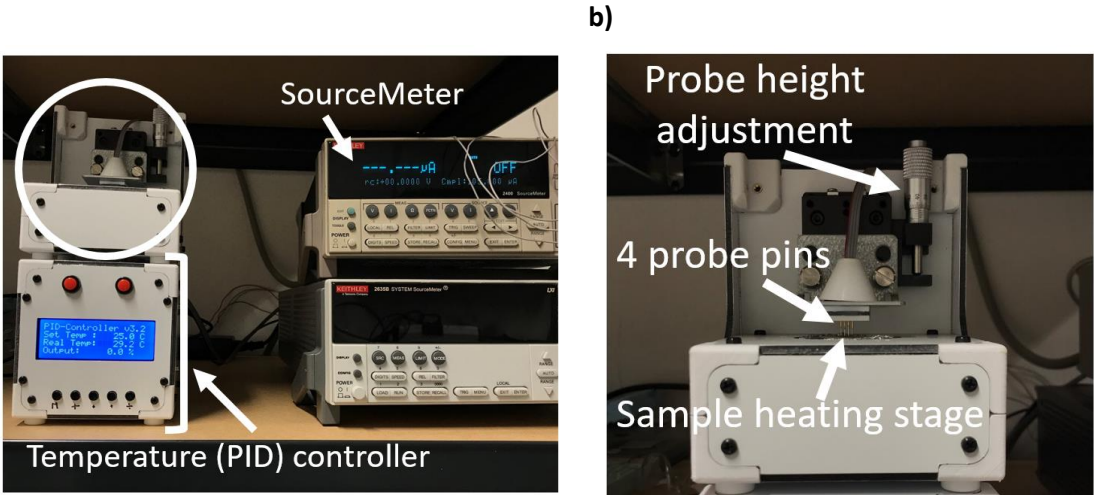
Additionally, a 25-point probe was also experimentally tested for the first time to determine more local gradients with respect to resistivity. The 25 probe pins are arranged in a 5×5 matrix (with a probe spacing of 1.67 mm) and a current is measured between pairs of these for a set applied voltage, with the overall system being controlled by a multiplexer. The analytical program (also developed in-house) produces a gradient plot showing the resistivity for the programmed configuration of pin measurements.
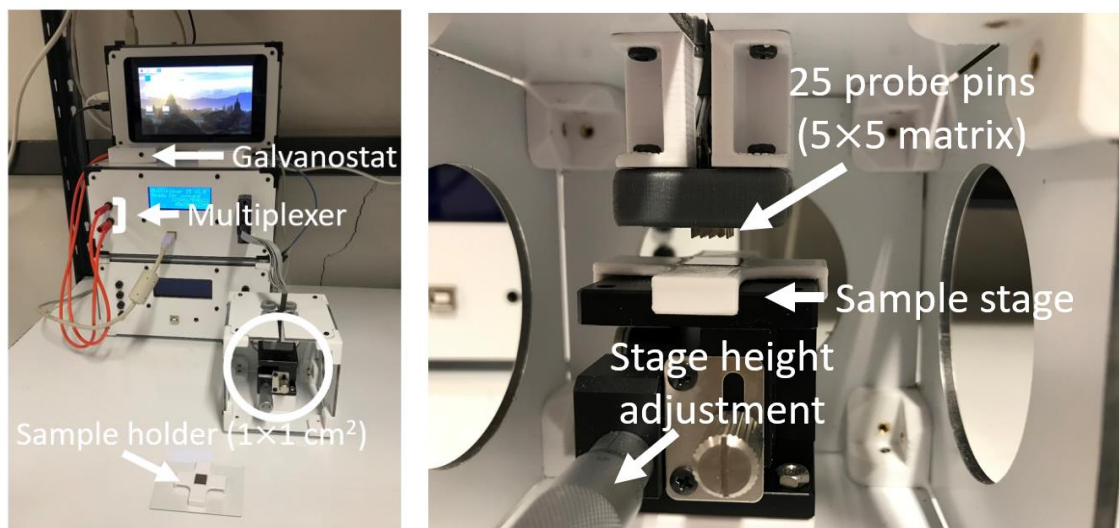
Figure 3.10 The 25-point probe, also developed in-house. The multiplexer controls a 5x5 grid of probe pins that measure the current between pairs of these in a programmed configuration.

Physical property measurement system

The physical property measurement system (PPMS) is a multifunctional tool that enables the study and measurement of various material properties under well-controlled conditions. For this thesis it was used for low-temperature resistivity measurements based on the same physical principles as described for the four-point probe. However, the sample connectivity and measurement setup differ slightly from the conventional four-point probe. For instance, probes are not directly *inserted* into the film surface to create electrical contact; instead, the sample is mounted on a measurement puck. This puck contains pre-defined current and voltage input pads, to which ohmic contact with the sample through metal-to-metal bonds needs to be established. One way to achieve this is by attaching leads (wires) between contacts and anchoring them with Ag paint. To improve ohmic contact on the sample, metal contact pads can be evaporated onto the surface with, for example, a thermal evaporator. It should be noted that the connection of the leads both at the puck and the film surface does introduce resistance that will contribute to the nominal value measured by the PPMS. The data should hence be normalized (to the initial 4-point probe resistivity measurement) prior to making comparisons between data sets. The sample should be insulated from the puck surface since it's conducting.

4   Experimental

This chapter recounts the experimental processes behind thin film depositions and subsequent characterizations. Details and information regarding chemicals and measurement instruments are provided here.

4.1   Atomic Layer Deposition

4.1.1   The reactor

All thin films were deposited using an F-120 Sat ALD reactor (ASM Microchemistry). The reactor contains six glass-pipes that are collectively enclosed by an outer glass tube and horizontally sectioned into eight temperature zones. Table 4.1 shows a schematic of a deconstructed reactor, with the external connection of the O_3 gas line and the position of each solid phase precursor in their respective precursor tube and temperature zone. The appropriate zone was determined from the sublimation of the precursor as reported by [66] and are summarized in Table 4.1. Precursor tube A and C were used for Nd(thd)$_3$ and Ni(acac)$_2$, respectively, and the second rare earth was placed in tube B for depositions with substitutions.

The reaction chamber containing the substrates was effectively positioned in zone 7, corresponding to a deposition temperature of 225 °C, which was maintained for the entire deposition. Initial tests for determination of GPC and composition were performed on Si(100) substrates. These were cut from larger Si-wafers into $1 \times 1\ cm^2$ and $3 \times 3\ cm^2$ squares, blown free of dust with pressurized air and positioned on a microscope glass slide in the reaction chamber as depicted in Figure 4.1 b). Since these substrates were not etched prior to depositions there was a 2-3 nm thick native SiO$_2$ amorphous layer on them. Films to be structurally and electrically characterized were also deposited on single-crystal SrTiO$_3$(001) (a = 3.905 Å, space group Pm$\overline{3}$m) (Crystal GbmH) to facilitate epitaxial growth. These were either $1 \times 1\ cm^2$ or $0.5 \times 0.5\ cm^2$ in size.

O_3 was supplied through a gas line from an AC-2505 (In USA) ozone-generator providing ca. 15 % O$_3$ in O$_2$ to inlet F in the reactor. Two pumps, both produced by vacuum engineering company Edwards, were used to attain an initial pressure of 2.4 mbar prior to all depositions; first an RV12-pump down to approximately 20 mbar, then an iH600-pump down to and maintaining 2.4 mbar. The inert carrier gas (N$_2$ purified by a Mykrolis purifier) flowed continuously against the exhaust direction in the outer tube and with the exhaust direction through the inner pipes at 200 cm³/min and 300 cm³/min respectively.
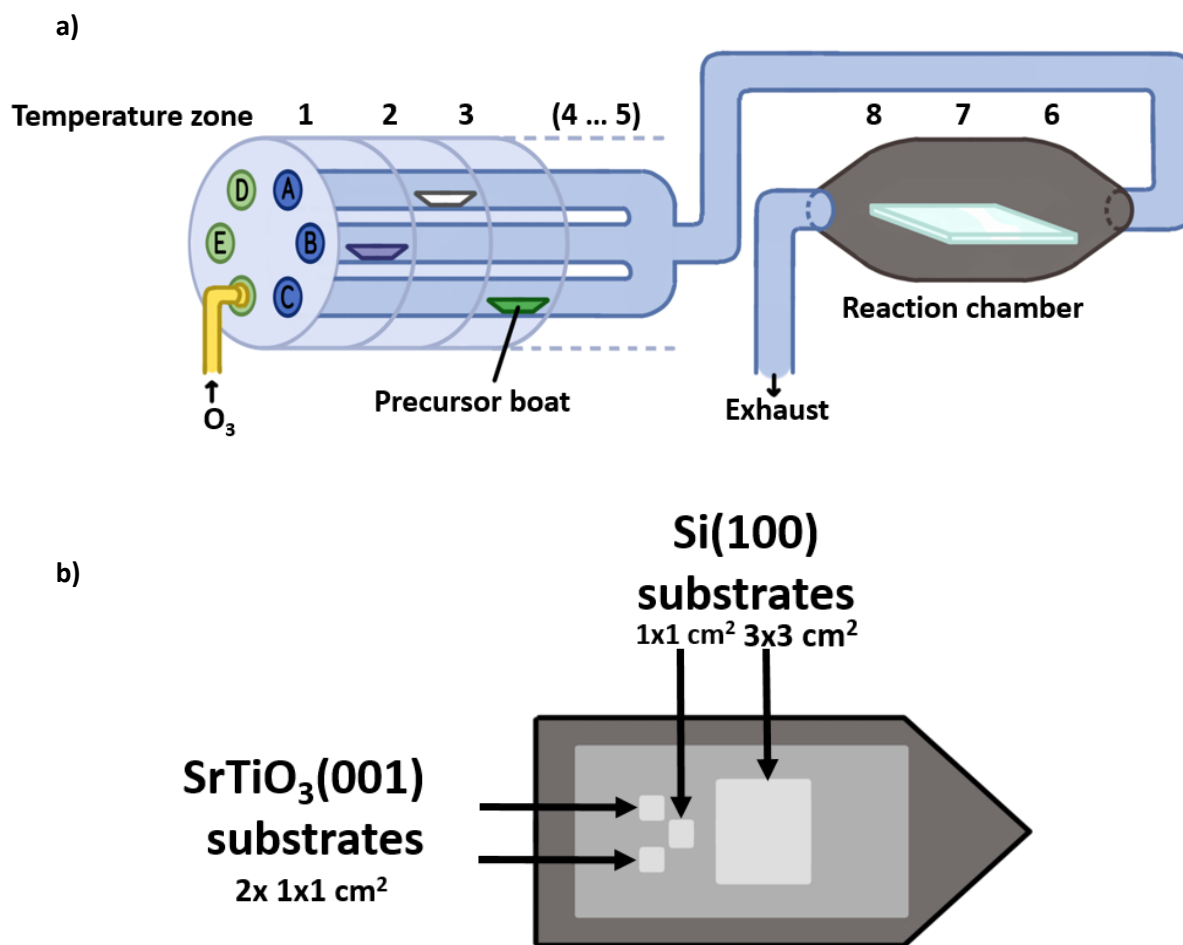
*Figure 4.1 Annotated schematic of a deconstructed ALD reactor. **a)** Precursor boats are placed in the appropriate temperature zone for sublimation, except for O_3, which is supplied through a gas line to inlet F (unlabeled). N_2 is used as both carrier and purge gas for the sublimated precursors (inlet not drawn). During a pulse, the net gas flow carries the precursor upstream to the reaction chamber, with excess leaving through the exhaust. **b)** Sizes and types of substrates used in certain depositions. The 3x3 cm_2 Si(100) substrate was always placed upstream, i.e., closest to the flow inlet.*

4.1.2 Precursors and chemicals

An overview of the precursors and other chemical species used for depositions is provided in Table X, with CAS number, manufacturer, purity, and sublimation temperature. All precursor except for Ni(acac)$_2$ were used directly as provided by the supplier.

Ni(acac)$_2$ was pre-deposition processed by re-sublimating it at 185 °C onto a cold finger in a Büchi oven.

Table 4.1 Details of the precursors and gases used for depositions of NdNiO₃ (RE,Nd)NiO₃ thin films. Precursors are listed with CAS number, manufacturer, purity and the temperature at which they were sublimated.

General formula	CAS number	Manufacturer	Details and purity [%]	Sublimation temperature [°C]
Precursors				
$Nd(thd)_3$	15492-47-4	Strem Chemicals (Volatec)	99 (unspecified)	160
$La(thd)_3$	14319-13-2	Strem Chemicals	99	185
$Pr(thd)_3$	15492-48-5		99	160
$Sm(thd)_3$	15492-50-9		99	160
$Eu(thd)_3$	15522-71-1		99	150
$Gd(thd)_3$	14768-15-1		99	140
$Tb(thd)_3$	15492-51-0		99	150
$Dy(thd)_3$	15522-69-7		99	135
$Ho(thd)_3$	15522-73-3		99	135
$Er(thd)_3$	35733-23-4		99	135
$Tm(thd)_3$	15631-58-0		99	130
$Yb(thd)_3$	15492-52-1		99	135
$Ni(acac)_2$	3264-82-2	Sigma Aldrich	97	185
Gases				
O_3	N/A	N/A	15 % O_3 in O_2	N/A
N_2			Purified by Mykrolis purified	
Note: (thd) = 2,2,6,6-tetramethylheptane-3,5,-dionate, (acac) = acetylacetonate, pentane-2,4-dione				

4.1.3 Rapid thermal processing for annealing thin films

Rapid thermal processing was used to prepare samples for further characterization following spectroscopic ellipsometry. It was chosen as the annealing method owing to the control of ramp rate and atmosphere this technique provides. Thin films were heated up to 650 °Cat a rate of 40-50 °C per minute and annealed at this temperature for 15 minutes in air before cooling back to room temperature.

4.2 Characterization Methods

4.2.1 Spectroscopic ellipsometry

The thickness and refractive index (measured at a wavelength of 632.8 nm) of the films deposited on Si(100) substrates were measured using an α-SE^{TM} from J.A. Woollam Co. equipped with a quartz tungsten halogen light source (incident angle of 70 °). A Cauchy-function from the CompleteEASE software was used to fit the measured data, in the selected range of 400-800 nm for the wavelength.

4.2.2 X-ray fluorescence

Average chemical composition for $NdNiO_3$, $(Sm,Nd)NiO_3$ and $(La,Nd)NiO_3$ samples was measured using an Axios mAX's X-ray fluorescence instrument (PANalytical), equipped with a 4 kW rhodium tube. The instrument was calibrated for the relevant samples according to Omnian standards and the data analyzed with the Stratos software. XRF analysis of other samples than the ones mentioned above was inhibited by a lack of calibration standards for the system.

4.2.3 X-ray photoelectron spectroscopy

Additional chemical analyses were carried out on a Theta Probe Angle-Resolved XPS (Thermo Scientific), with an Al $K\alpha$ source (E = 1486.6 eV). Survey scans and detailed scans (around O 1s and Ni 2p) were conducted using a pass energy of 200 eV and 60 eV, respectively, and analyzed with the Thermo Avantage software. The pressure in the analysis chamber was maintained at approximately 10^{-8} mbar during measurements.

4.2.4 X-ray diffraction

A D8 Discover X-ray diffractometer from Bruker with a Lynxeye strip detector and a Cu-Ka source (λ = 1.5406 Å) was used to structurally characterize select thin films both as deposited and post-annealing. The samples were mounted on thin-film XRD sample holders and scanned over a 2θ - range from 10 ° to 90 °, with a step-size of 5 s per increment.

4.2.5 Reciprocal space mapping

Reciprocal space mapping was performed on a PANalytical Empyrean diffractometer with a Cu $K_{\alpha 1}$ source powered at 45 kV and 40 mA and a Pixcel 3D detector. A hybrid monochromator (two Ge(220) and Cu-mirror) was used in tandem with a ¼ inch slit and 10 mm mask. Soller slits on the diffracted side were inserted to limit the vertical divergence of the beam.

4.2.6 Probe measurements

Resistivity measurements at room temperature were obtained with a Jandel four-point probe with probe spacing of 1 mm and curvature of the probe tips of 0.5 mm.

The resistivity measurements at elevated temperatures were performed using a home-made 4-point probe based on gold-coated pogo pins with 1.6 mm spacing and a current range ensuring a potential drop less than 2 V. The heating stage was home-built and based on a 50 W heating cartridge and a home-built PID controller.

The 25-pin probe was home-built based on gold-coated pogo pins in a 5x5 array with 1.67 mm spacing between the tips of the pins. The measurements were performed with a galvanostat based on Ref [67].

4.2.7 Physical property measurement system and gold-contacts

Temperature-dependent resistivity measurements were obtained using a Quantum Design Physical Property Measurement System. One cooling-heating cycle was performed, in which the sample was cooled from 300 K to 20 K and heated back up, at a rate of 5 K per minute. Four 20 nm thick gold contacts were deposited along the diagonal of the film surface using a thermal evaporator (Balzers BAE 250) and copper masks. The contacts were 1 mm in diameter and spaced 1 mm apart. The sample was positioned in an AC transport puck and the Au-contacts connected to its electrodes through gold wire and secured with Pelco conductive silver paint (Ted Pella) at both ends.

4.3 Research Plan

Having introduced the theoretical and practical preface of the work that was carried out, it is instructive to present the research plan more comprehensively and to discuss some decisions that were made before or during the experimental work phase.

Figure 4.2 presents the overall workflow, illustrating the integral feedback loop between deposition and characterization. Results from the various characterization methods were used as pointers for following depositions to tune thin film properties. Each colored section corresponds to the objectives of the thesis, outlined in 1.3.

4.3.1 Testing deposition temperatures

Two deposition temperatures, 225 °C and 275 °C, were tested for the deposition of Nd_2O_3. Previous experience with $LaNiO_3$ and $SmNiO_3$ in the research group indicates that a deposition temperature within this range is appropriate for as deposited epitaxy of the rare-earth nickelates. As was discussed in 3.1.3, the lower bounds for the deposition temperature is set by the highest sublimation temperature of the cation precursors, while the upper bound is determined by the temperature stability of the precursors. Within this range, the choice of deposition temperature ultimately becomes a question of balancing temperature with pulse duration.

As outlined in 1.2, low-temperature synthesis routes are compatible with conditions for industrial processes and could enable monolithic integration, especially with the structural similarities of perovskite oxides. The goal is not necessarily to find the lowest temperature possible, but rather one that maximizes use of precursor and applies to the different materials systems that a monolithic device stack may consist of. This ensures the best efficiency and functionality of the process, so lower temperatures could have been attempted but are pivotal for the work here.

① **ALD Process**

Deposition temperature:
225 °C and 275 °C

Pulse and purge durations:
$Nd(thd)_3$, $Ni(acac)_2$ and O_3

Composition tuning

Goal: Obtain stoichiometric films

Subcycle arrangement variations

Goal: Optimize properties

② **Characterization**

| Optical | Chemical | Structural | Electronic |

Composition tuning

Subcycle variations

Rare-earth substituted

Select samples

Spectroscopic ellipsometry

X-ray fluorescence

X-ray diffraction

4-point probe

X-ray photoelectron spectroscopy

Reciprocal space mapping

Temperature-varying 4-point probe

20 - 300 K   298 - 573 K

③ **Rare-earth Substitution**

(RE,Nd)NiO$_3$

Goal: Tune the T_{MI} by substituting rare-earths for Nd
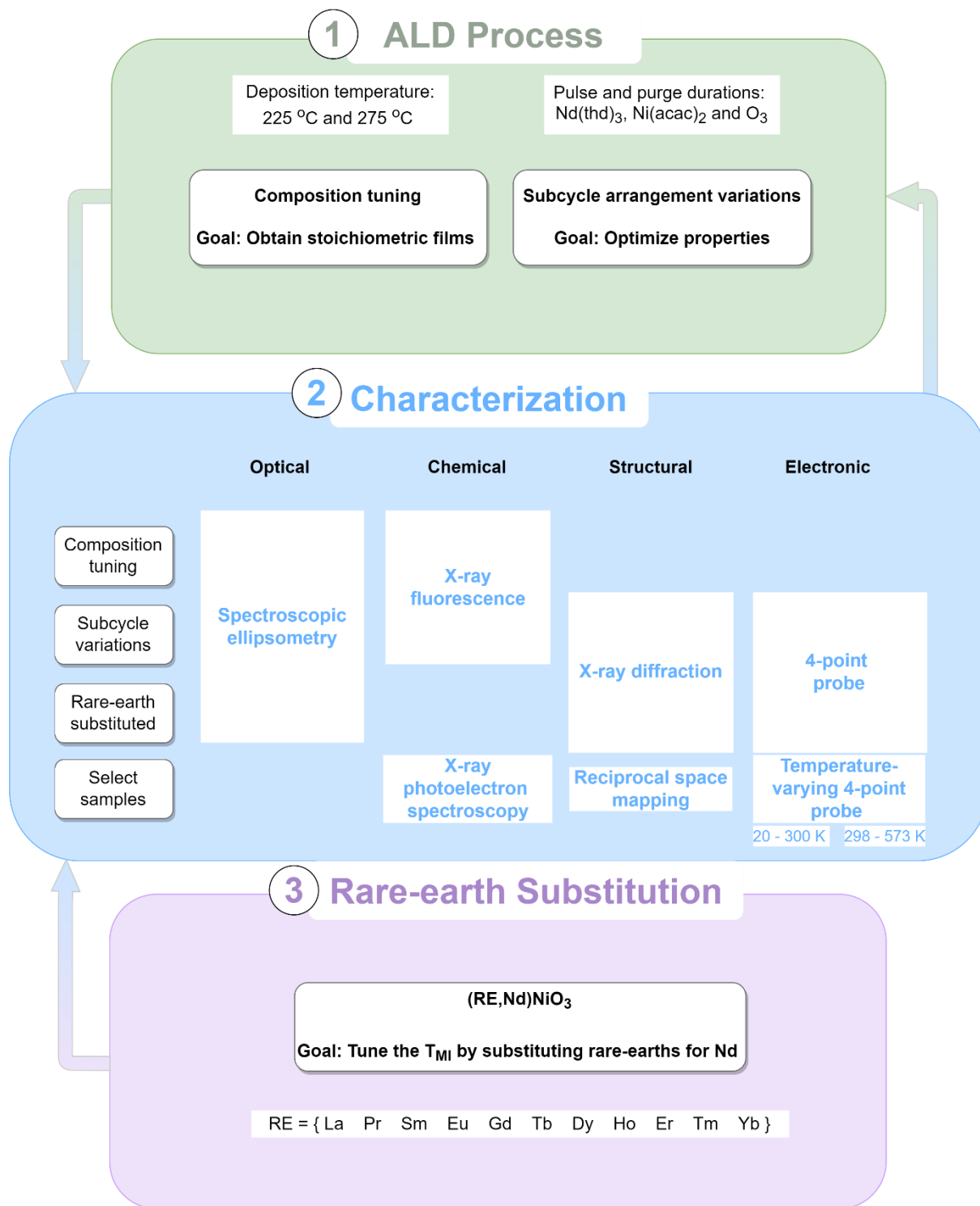
RE = { La Pr Sm Eu Gd Tb Dy Ho Er Tm Yb }

Figure 4.2 Schematic research plan showing how the work is structured in alignment with the stated thesis objectives. Each colored section corresponds to a different focus, with arrows indicating the primary workflow.

4.3.2 Considerations about the Ni-precursor

The choice of Ni-precursor depended on several factors, some of which regard general precursor characteristics as described in 3.1.2. While Ni(thd)$_2$ could have been an option, it has been shown to have relatively low gas phase stability [68]. Moreover, H(acac) is more acidic than H(thd) (based on their pKa values of 8.79 [51] and 11.6, respectively), meaning that its M-O bond is weaker and more likely to dissociate.

Interestingly, Ni-containing precursors may catalyze their own decomposition when pulsed in excess, as was the proposed hypothesis in a study by Nilsen *et al.* [69]. Since the study was conducted with Ni(thd)$_2$ it is unknown whether similar effects occur with Ni(acac)$_2$, but it is worth being aware of during the investigation.

Re-sublimation of Ni(acac)$_2$ was implemented to remove impurities and/or water residue, which is important for the anhydrous species. It facilitates the formation of its octahedrally coordinated trimeric form [Ni(acac)$_2$]$_3$, which contains near-ideal Ni-O-Ni bonds [17]. This has been hypothesized to play a crucial role in achieving as deposited low-temperature epitaxy.

4.3.3 Selecting rare-earth elements for substitution

The most common oxidation state for the rare-earth elements is +3 and their strong preference for this is integral to the stability of Ni^{3+} in the ternary phase. However, some of the rare earths *can* have other oxidation numbers, *e.g.,* +2 for Eu, Tm, Sm, and Yb, although it is very unlikely in an environment that is as strongly oxidizing as O$_3$. There is a greater chance that Ce, Pr, Tb, and Dy adopt their +4 state, and Ce^{4+} is particularly stable because it reaches the full electronic configuration of Xe. For this reason, Ce was not included in the rare-earth substitution. Lutetium also does not appear in the selection because of availability.

4.3.4 Deposition structure for ternary and quaternary oxides

Table X shows the approach to structuring a deposition program for a general ternary (including only precursors A and B) or quaternary (precursors A, B and C) oxide. Parameters a, *b* and c specify how many times each binary oxide subcycle is repeated and thus the binary oxide layer thickness. These also define the ratio that is used in this work to refer to the overall pulsing scheme. In the pure Nd-Ni-O system, different samples or series of samples will be referred to as NNO*a:b* The number *x* of total repetitions of the entire sequence of subcycles, which is the supercycles, determines the film thickness.

Table 4.2 Generalized deposition recipe for a ternary or quaternary oxide. Exemplifies the use of supercycle and supercycle.

	Subcycle repeated *l* number of times	Precursor A + oxygen source	
Supercycle repeated *x* number of times		Pulse	Purge
	Subcycle repeated *m* number of times	Precursor B + oxygen source	
		Pulse	Purge
	Subcycle repeated *n* number of times	Precursor C + oxygen source	
		Pulse	Purge

A sample program structure is provided in Table 4.3 below for the deposition of $(Sm,Nd)NiO_3$ where Sm is substituted into the stoichiometric 3:1 regime to yield the 1:2:1 substitution scheme. The notation *RE*-NNO*x:y:z* will be used to denotes these samples, in which *x:y:z* is the pulsing ratio and *RE* is the substituting rare-earth element. To maximize mixing, the rare-earth pulse is sandwiched between two Nd-pulses. The number of repeated supercycles is adjusted so that the total number of cation pulses is as close to 1000 as possible. For clarity, the binary oxide that is deposited is written in brackets, and the standard pulsing cycle below corresponds to pulse – purge (precursor A), pulse – purge (precursor B).

As opposed to the deposition structure above, this aims to enhance mixing of the precursors by incorporating the single Eu_2O_3 layer in between two subcycles of Nd_2O_3. All the pulsing regimes for the rare-earth substituted thin films followed this approach to ensure that the interactions between $Nd(thd)_3$ and $Ni(acac)_2$ remained as constant as possible. This only pertains to the substituted thin films because fully mixing Nd and Ni in a 3:1 ratio becomes equivalent to merely alternating between them, *i.e.*, the potential effect of stacking oxide subcycles and building thicker binary oxide layers becomes lost.

Table 4.3 Deposition recipe for $(Sm,Nd)NiO_3$ with a fully mixed 1:2:1 (RE:Nd:Ni) pulsing scheme.

Supercycle	Subcycles	Precursors [Binary oxide]	
Cycle 250	Cycle 1	$Nd(thd)_3 + O_3 [Nd_2O_3]$	
		$3-3$ (Nd)	$3-3$ (O_3)
	Cycle 1	$Sm(thd)_3 + O_3 [Sm_2O_3]$	
		$3-3$ (Sm)	$3-3$ (O_3)
	Cycle 1	$Nd(thd)_3 + O_3 [Nd_2O_3]$	
		$3-3$ (Nd)	$3-3$ (O_3)
	Cycle 2	$Ni(acac)_2 + O_3 [70]$	
		$2-2$ (Ni)	$3-3$ (O_3)

5 Results

The obtained experimental results are presented and analyzed in this chapter. It is sectioned according to the main thesis objectives introduced in 1.3, beginning with the development of an ALD synthesis route for NdNiO$_3$ thin films. Then follows the results obtained from chemical, structural and electrical characterization, before a summary of the rare-earth substituted variants is presented.

5.1 Atomic Layer Deposition of Stoichiometric NdNiO$_3$ Thin Films

The first objective was to map out and acquire control of the ALD synthesis route for NdNiO$_3$. Conventionally, a ternary complex oxide is deposited by combining the processes for its constituent binary oxides and NdNiO$_3$ is ideally obtained by depositing layers of Nd$_2$O$_3$ and NiO that together will form the ternary phase.

This chapter presents the stages of the experimental work and the results that led to the development of an ALD recipe for stoichiometric NdNiO$_3$ thin films.

5.1.1 Growth characteristics and deposition parameters

Nd(thd)$_3$ was sublimated from its precursor boat in the reactor at 160 °C and, in separate depositions, pulsed into the reaction chamber for varying durations of time, followed by an O$_3$ pulse and purge. The standard pulsing cycle was x s pulse of Nd(thd)$_3$, 4 s purge, 4 s pulse of O$_3$, 4 s purge, hereafter written as (x-4)-(4-4) with respect to Nd(thd)$_3$ and O$_3$. The thickness and uniformity of the resulting Nd$_2$O$_3$ films were measured using spectroscopic ellipsometry, with the results shown in Figure 5.1 for deposition temperatures of 225 °C and 275 °C.

The error bars show the standard deviation from the average GPC for a single thin film sample, based on the thickness measured at nine different points. As such, it is not a measure of the deviation between replicated depositions, but rather an indication of the film uniformity in a single deposition. For depositions at 225 °C, there is a clear saturation of the GPC for 2 s pulses. The slight decrease (increase) in GPC with 3 s (8 s) long pulses is considered negligible as they could be due to variations in the wafer's native silicon oxide layer, limitations to measurement precision and consistency, or even environmental factors such as water content or contaminations. As such, they were deemed experimental variations. A 3 s long Nd(thd)$_3$ pulse was thought to best guarantee that the saturation threshold was met without compromising resource and time effectiveness. With this pulse duration, the GPC of the binary oxide thin film was approximately 0.23 Å/cycle.
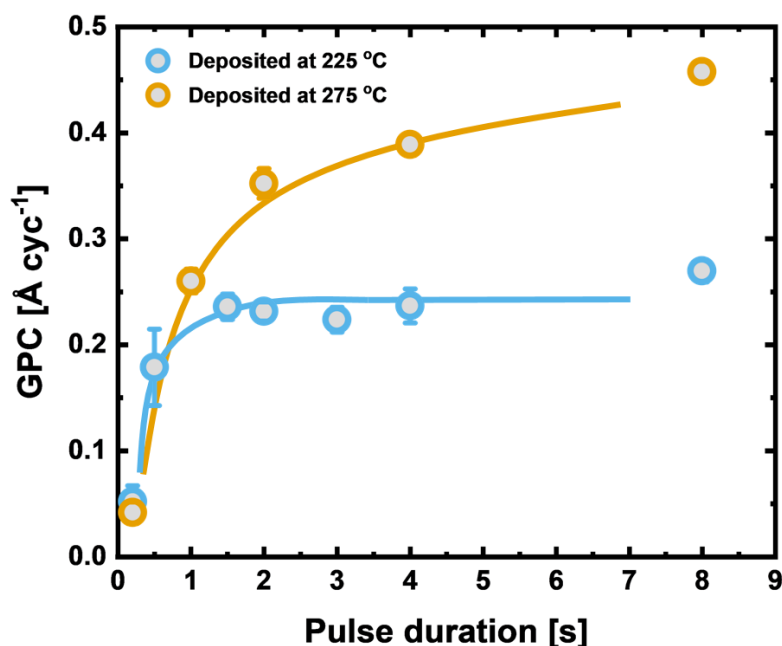
Figure 5.1 Growth per cycle (GPC, per cation pulse) of Nd_2O_3 thin films for varying pulse durations of $Nd(thd)_3$. The two curves correspond to two different deposition temperatures: 225 °C (blue) and 275 °C (orange), with fitted curves shown as lines. Error bars indicate the standard deviation from the average GPC for each thin film sample. A standard pulsing cycle of x s pulse of $Nd(thd)_3$, 4 s purge, 4 s pulse of O_3, 4 s purge was employed for all depositions while varying x.

At 275 °C, no such clear saturation plateau is observed, presumably owing to CVD-type growth (gas-phase reactions) by thermal decomposition. The significant discrepancy between depositions at 225 °C and 275 °C shows that self-saturating growth is enabled by the low temperatures used in ALD.

It should be noted that in depositions in which a precursor pulse or purge duration was varied, all other pulse and purge parameters that had not yet been experimentally determined were kept constant and excessively long. It was known from previous experience with these systems that 4 s pulses and purges would be sufficient to isolate the effect of the parameter in question, at least as long as self-limiting behavior had been confirmed.

The pulse and purge durations were similarly determined for $Ni(acac)_2$, in the ternary $NdNiO_3$ system. The pulsing cycle was given by (3-3)-(*l*-3)-(4-4) for $Nd(thd)_3$, $Ni(acac)_2$ and O_3, respectively, where *l* was the varied pulsing time for $Ni(acac)_2$. As given in Figure 5.2, the GPC displays the same type of dependency on precursor pulse duration as $Nd(thd)_3$. A 2 s pulse was considered sufficient since there was not a significant difference in GPC with 4 s. The purge was also investigated and set to 2 s.

The film growth is nearly independent of O_3 pulse duration and within the expected range of experimental uncertainty. Excepting the film with the shortest O_3 pulse, uniformity is excellent and mostly owing to natural variations. A 3 s pulse was deemed appropriate, and was later found to result in NiO films with an average GPC of 0.4 Å per cycle.
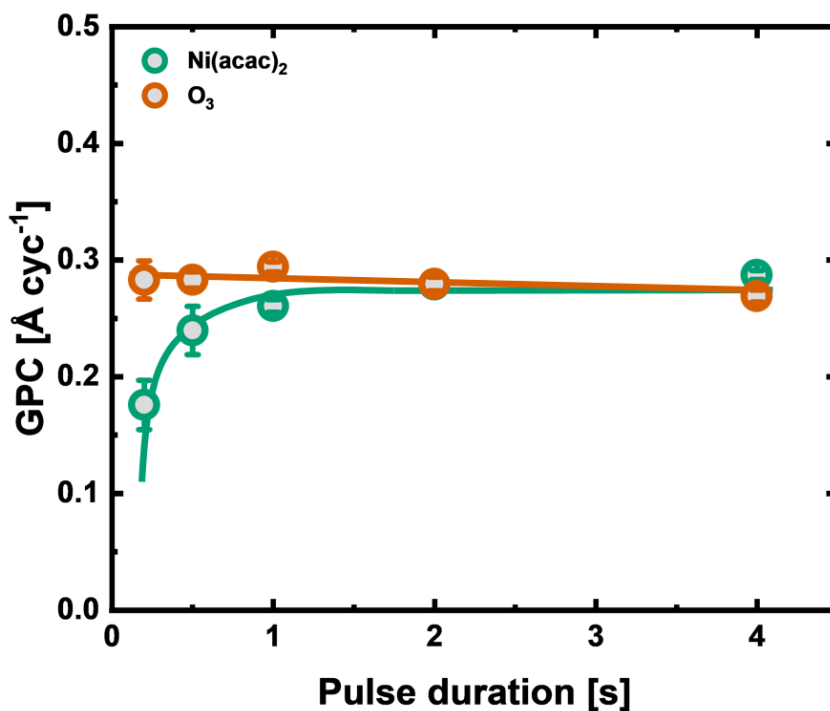
Figure 5.2 Growth per cycle (GPC, per cation pulse) of NdNiO$_3$ thin films deposited at 225 °C for varying pulse durations of Ni(acac)$_2$ (green) and O$_3$ (orange), with error bars showing the standard deviation from the average GPC for each film. Other precursor pulses and purges were kept in excess while testing each of these separately.

5.1.2 Chemical composition range

Having determined the appropriate pulse and purge durations for the precursors involved in ALD of NdNiO$_3$, it was necessary to identify the pulsed ratio of Nd(thd)$_3$ to Ni(acac)$_2$ that would give a stoichiometric 1:1 ratio of Nd:Ni in the film. This can only be done empirically by observing the growth relationship between the two precursors.

A composition range was mapped out by pulsing Nd(thd)3 and Ni(acac)2 in the ratios 7:1, 5:1, 3:1, 2:1, 1:1, 1:2, 1:3 and 1:5 (Nd:Ni) to see what film composition each ratio resulted in. The relative amounts of Nd$_2$O$_3$ and NiO in the film were measured with XRF and converted into atomic percentage of the cations based on the amounts of the binary oxides reported by the instrument. Figure 5.3 shows this plotted against the amount of pulsed Nd. The curve is slightly concave, meaning there is less incorporation of Nd in the film per precursor pulse compared to the same for Ni. This is to be expected since the three thd-ligands surrounding Nd will lead to greater steric hindrance than the two acac-ligands on Ni. It is therefore necessary to pulse more Nd than Ni per cycle to achieve a 1:1 ratio in the film. This is underpinned by the relative difference in binary oxide GPCs: 0.23 Å cyc^{-1} for Nd$_2$O$_3$ and 0.40 Å cyc^{-1} for NiO, with the GPC of the ternary oxide in the range of 0.25 - 0.27 Å cyc^{-1}.

Based on the rule of mixtures, a predicted Nd content can be calculated from the growth characteristics of the binary oxides:

$$\frac{P_{Nd} \times GPC_{Nd}}{(P_{Nd} \times GPC_{Nd}) + (P_{Ni} \times GPC_{Ni})},$$

where P is the amount of pulsed precursor given as a percentage of total amount of cations pulsed, and the GPC is for the binary oxide. This corresponds to the orange data points in Figure X.
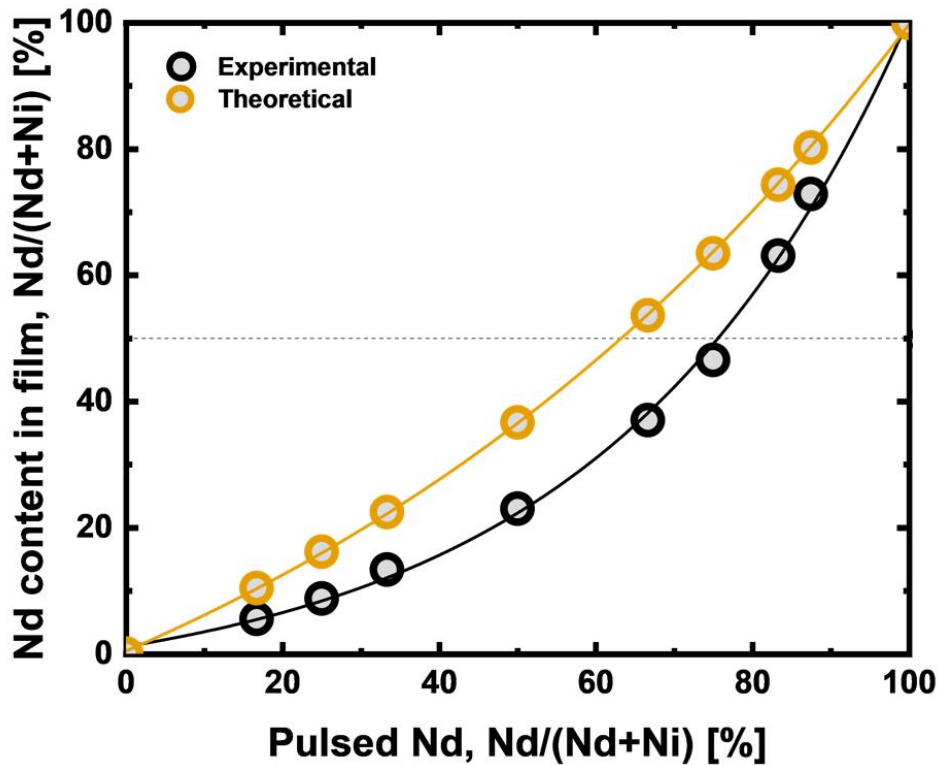
Figure 5.3 Composition range obtained for different pulsing ratios between Nd(tdh)$_3$ and Ni(acac)$_2$ using x-ray fluorescence. Both Nd content in film and pulsed Nd are given as percentage of total cation content. Experimentally obtained data (black) and theoretically predicted data (orange) are shown with nonlinear curve fits.

Interpolating the best-fit line to 50 % Nd in the film (shown as a dashed line in Figure X) shows that a 3:1 pulsing regime results in the composition closest to stoichiometric (with 46.6 % Nd in the film). Although it is not exactly 50 %, the intention is to fine-tune this later using variations in the pulsing regime as described previously in 3.1.4. For simplicity, the 3:1 pulsing regime is hereafter referred to as the stoichiometric pulsing regime or ratio.

Even with the stoichiometry of Nd and Ni confirmed with XRF, it could be possible to have mixed oxidation states for Ni (+2 and +3) if oxygen vacancies were introduced. Since oxygen non-stoichiometry would affect the oxidation state of Ni, XPS analysis around Ni $2p_{3/2}$ was performed on a 3:1-pulsed sample before annealing to assess this possibility. The results from the scan reproduced in Figure 5.4. The core level photoelectron peak occurs at a binding energy of 854 eV and is not a

multiplet-split, as would be expected with mixed oxidation states. It is therefore most likely that Ni stays in its +3 oxidation state for thin films deposited with the same conditions.
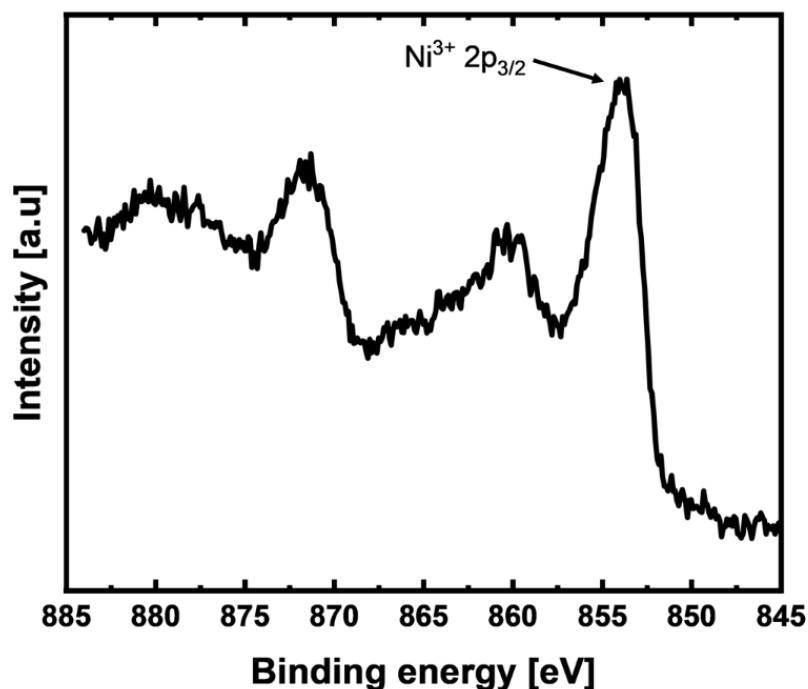
Figure 5.4 X-ray photoelectron spectroscopy scan of Ni 2p. The most intense peak at a binding energy of ~854 eV corresponds with Ni being in the +3 oxidation state.

5.1.3 Subcycle arrangement and stoichiometric variations

As was discussed in 3.1.4, exploring the effects of subcycle arrangement is key to realizing the control and quality of epitaxial thin films that would make ALD excel. With the aim of tuning and improving conductivity, small variations were made to the cycle arrangement in the deposition recipe.
Films were thus deposited using pulsing ratios that correspond to multiples of the 3:1 (stoichiometric) pulsing ratio, namely 6:2, 12:4 and 24:8 (while keeping the total number of cation pulses at 1000). This can be recognized as varying degrees of multilayer approach since the individual binary oxides are deposited in thicker layers.

Additional variations to these multilayer (stoichiometric ratio multiples) pulsing schemes were also made to deposit thin films that should be very chemically similar to their stoichiometric/multilayer counterparts but may be structurally different enough to affect their electronic transport. The pulsing regimes for these stoichiometric ratio multiple variations consisted of either one additional or one less Nd(thd)$_3$-pulse than the stoichiometric multiple ratios, excluding 24:8. This means that the chemical composition range was extended with four additional regimes: 5:2, 7:2, 11:4 and 13:4, which are referred to as stoichiometric ratio multiple variations. The grouping of the different series and their relations is summarized in Table 5.1.

One Nd(thd)₃ pulse less	Stoichiometric and multilayers	One Nd(thd)₃ pulse more
	3:1	
5:2	6:2	7:2
11:4	12:4	13:4

Figure X shows the GPC for the films of different pulsing ratios (labeled next to each data point). There is a general decline in the GPC as the amount of pulsed Nd increases, with some slight deviations for the 11:4 and 7:2 ratios. Both of these exhibit a more rapid growth than would have been expected based on the general trend. The decrease in GPC for the multilayer series aligns well with the mapping of the chemical composition range, as Nd(thd)₃ is expected to grow more slowly than Ni(acac)₂. Thus, even though the ratio of the precursors remain the same, the growth of the ternary oxide is dependent on the arrangement of their pulses in the deposition.
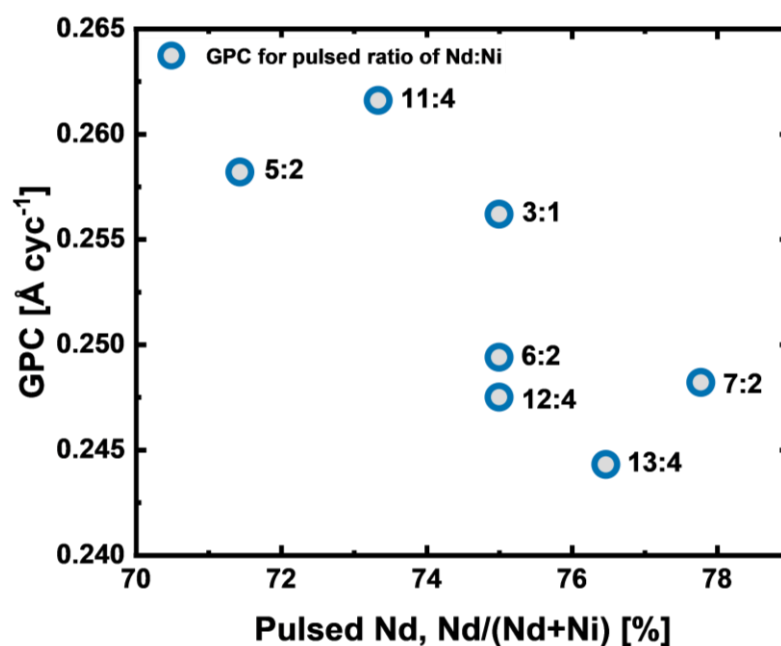
Figure 5.5 Growth per cycle (GPC, per cation pulse) for NdNiO₃ thin films on SrTiO₃(001) pulsed with different pulsing regimes.

This also becomes evident when considering the amount of Nd incorporated into the film for each pulsing scheme. The amount of Nd relative to Ni should in theory remain constant, but that assumption does not appear to hold true given the data in Figure 5.6. As the number of sequential precursor pulses (in a row) increase (from 3:1 to 12:4), the amount of Nd incorporated in the film is seen to increase correspondingly, paralleling the observation for GPC in a reverse order. This behavior hints at one of the more *interesting* and lesser explored phenomena/attributes of ALD: that the composition of individual pulses and their ordering can have a profound effect on the resulting material (and implicitly, its properties).
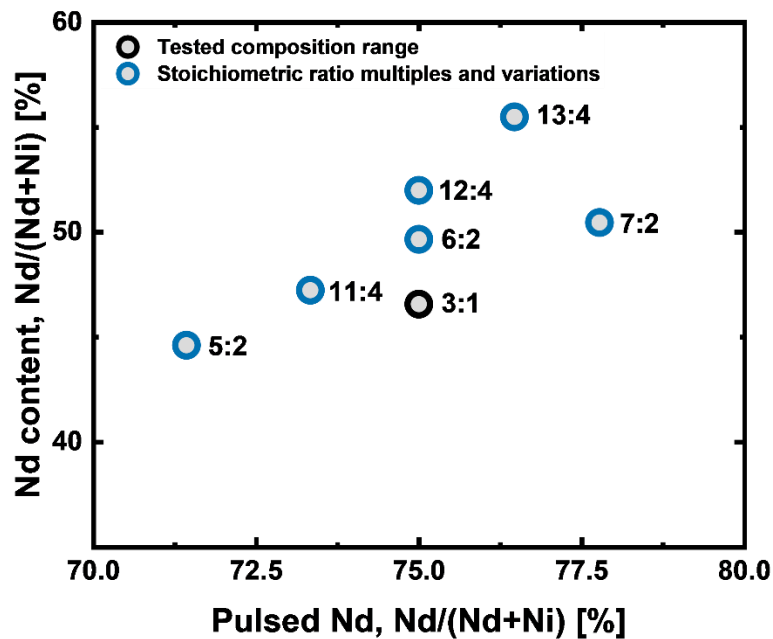
Figure 5.6 Compositional variation in Nd content in film for different amounts of Nd pulsed, given by the different pulsing schemes (labeled).

Notably, the Nd content in the film increases proportionally with the amount of Nd pulsed, with the 7:2 pulsing regime being the only exception. While this is not surprising given that the overall trend was the same for the first composition range, it cannot be taken for granted that such small variations would have a directly transferable effect. This demonstrates that a high degree of control in terms of chemical composition can be achieved for this ALD process.

5.1.4 Summary

With the empirically optimized pulse and purge parameters to ensure self-limiting growth, uniform and stoichiometric NdNiO$_3$ thin films were obtained at 225 °C. Chemical composition could be varied using the pulsed ratio between Nd(thd)$_3$ and Ni(acac)$_2$, with a 3:1 pulsing regime resulting in the desired 1:1 stoichiometry. Stoichiometric ratio multiples and variations of these changed the Nd-content in the film within a range of $\pm$ 5 %, demonstrating the ability to more precisely tune composition with subcycle arrangement. The fact that the growth characteristics of the ternary system did not follow the rule of mixtures based on the growths for the binary oxides demonstrates the deviation from "ideal" behavior that often characterizes complex oxide ALD. This is crucial knowledge when tuning process parameters towards optimal film functionality.

5.2 Characterization of Physical Properties

Having identified an ALD synthesis route for stoichiometric NdNiO$_3$ thin films, the next step was to probe the structural relationship between the film and substrate. The electronic properties of the thin

films were then characterized by measuring their room-temperature resistivity to elucidate any potential relationships between structure and electronic properties.

Both structural and electrical characterization was conducted on films deposited on STO-substrates, since the films on Si-substrates were amorphous and the conductivity of the substrate would interfere with measurements. This was confirmed with XRD (diffractogram can be found in Appendix 1A.2) and four-point probe measurements. The samples did not crystallize or conduct regardless of thermal treatment, presumably due to the native, amorphous SiO_2 layer on the substrate surface.

5.2.1 Structural characterization

XRD was standardly used to gauge the crystallinity (or lack thereof) of the thin film samples, as out-of-plane orientation can easily be confirmed against the substrate reflections.

A representative sample diffractogram obtained for a NNO3:1 thin film is shown in Figure 5.7. Since the substrate (STO(001))is effectively one large single crystal, its reflections dominate the diffractogram and a logarithmic scale is needed to distinguish the reflections from the thin film. Except for one sample, XRD scans of as-deposited stoichiometric 3:1-pulsed films all exhibited thin film diffraction peaks that correspond to the (001), (002) and (003) crystal planes at approximately $2\theta =$ 23.5 °, 47.8 ° and 75.1 °. These were deduced by calibrating the diffractogram pattern according to the known angles for the substrate reflections and then reading the angle at the maximum thin film peak intensity.

Compared to the Bragg reflection angles ($2\theta =$ 23.3 °, 47.7 ° and 74.7 °) for bulk $NdNiO_3$, the thin film reflections from the (*00l*) family of crystal planes are shifted to the right, which means that they have contracted in the out-of-plane direction compared to the bulk unit cell. This corresponds well with the in-plane tensile strain that STO imposes.

The (001)-reflection in diffractograms obtained for all of the different pulsing regimes is shown in Figure 5.8 for the series 3:1, 6:2, 12:4 (multilayers, top), 5:2, 6:2, 7:2 (NNO*x*:2, middle), and 11:4, 12:4, 13:4 (NNO*x*:4 series, bottom), with differences between the films as deposited (AD) and after annealing (AA) for each pulsed ratio.
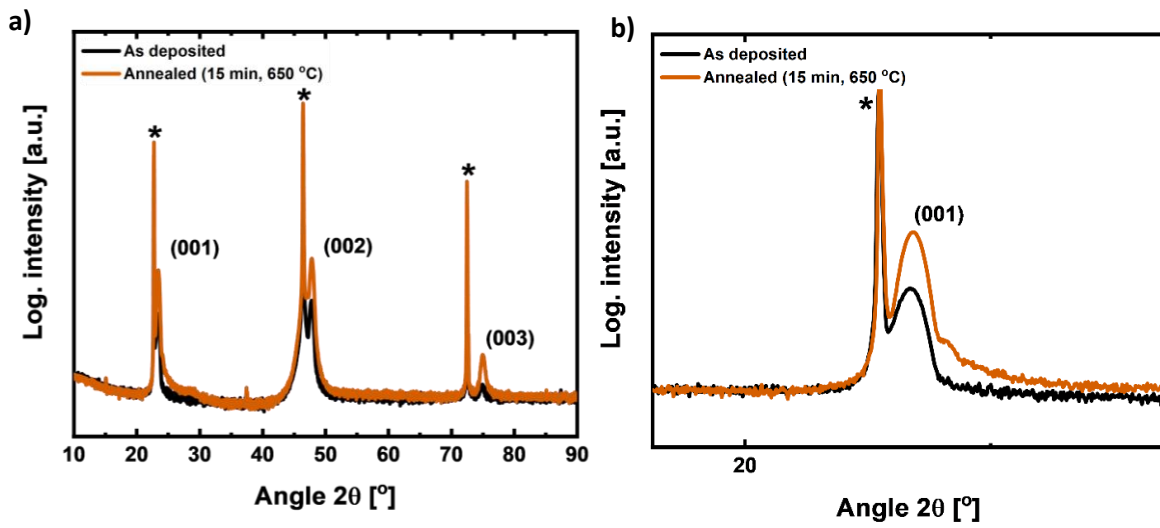
Figure 5.7 X-ray diffractogram for stoichiometric (3:1-pulsed) NdNiO₃ thin films on SrTiO₃, as deposited (black line) and after annealing in air for 15 minutes at 650 ℃ (orange line). **a)** *The most intense reflections stem from the substrate, marked with asterisks, with NdNiO₃ reflections appearing to the right of each, labeled as (hkl).* **b)** *Zoomed-in version of the (001) peak and visible fringes from the thin film after annealing.*
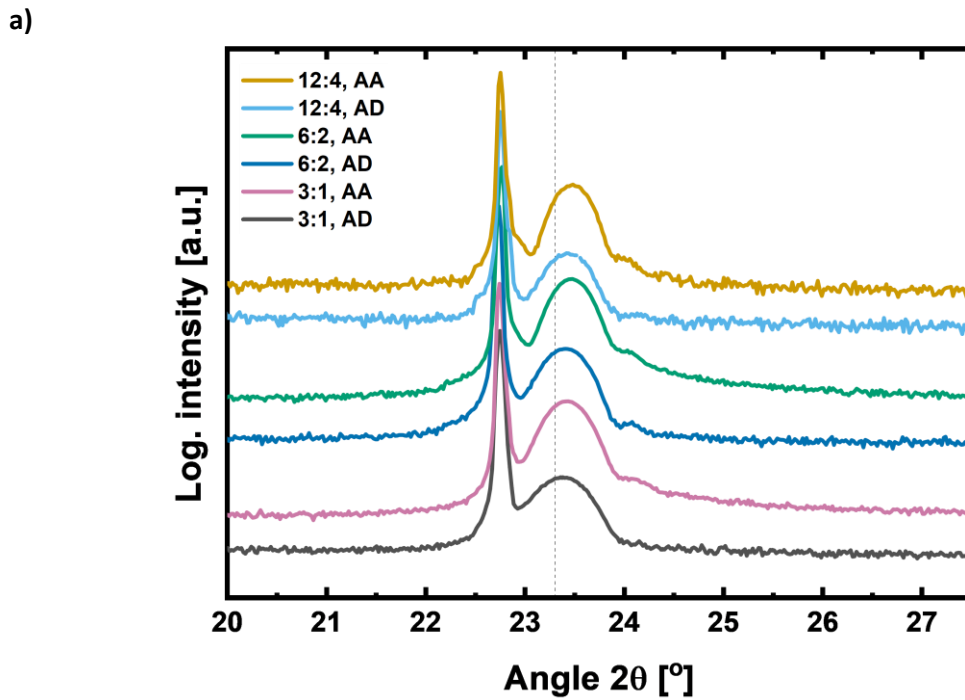
b)
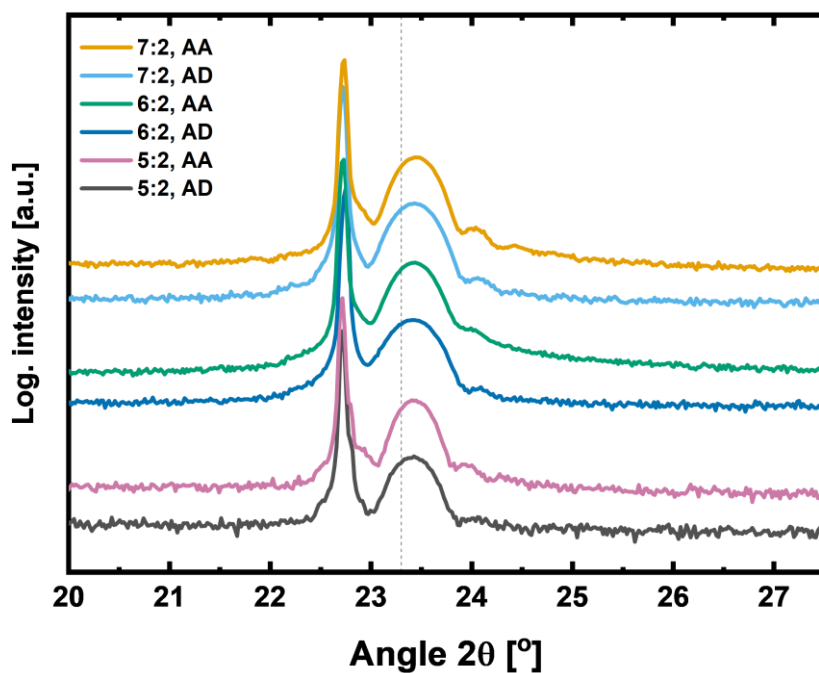
c)
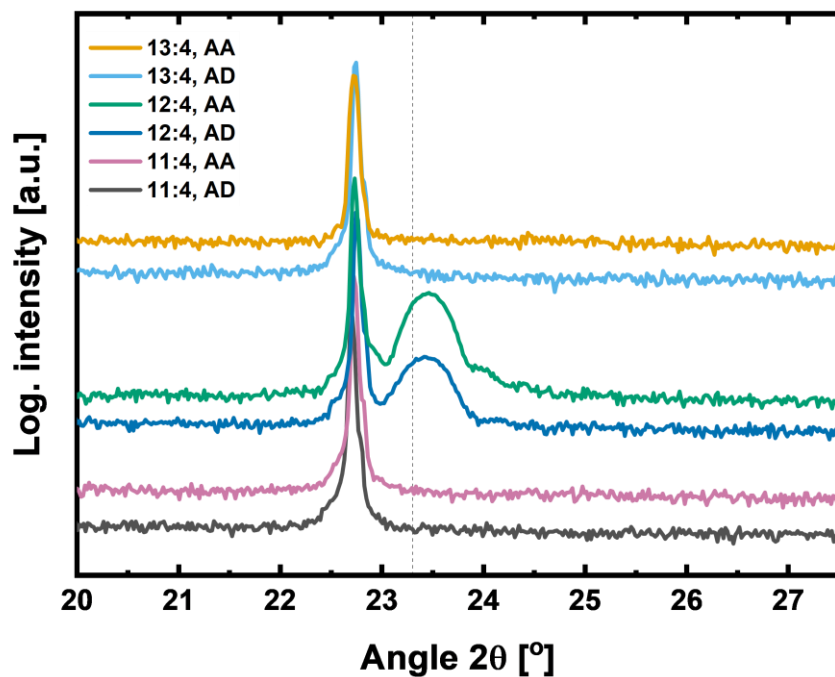
*Figure 5.8 Comparisons of x-ray diffractograms around the (001)-reflection for three series of NdNiO$_3$ thin films on STO(100), deposited with different pulsing ratios of Nd:Ni: **a)** multilayer series, **b)** NNOx:2 series (variations around 6:2 ratio), **c)** NNOx:4 series (variations around 12:4 ratio). AD denotes films as deposited and AA after annealing in air for 15 minutes at 650 °C.*

Films in the multilayer series and the NNO*x*:2-series all exhibit clear thin film diffraction reflections whose positions shift to slightly higher angles when annealed. The intensity can also be seen to increase marginally and a thin film interference fringe becomes more prominent after annealing. This

indicates that the initial compression in the *c*-direction is enhanced. For the purpose of comparing the diffraction behavior of crystalline films, the one and only 6:2 sample that became crystalline was used in this series. The other NNO6:2 thin films did not exhibit any reflections in their diffractograms.

In the NNO*x*:4-series, only the 12:4-pulsed film became sufficiently crystalline to exhibit thin film reflections. One may be able to discern a slight broadening or shoulder to the right of the substrate reflection for NNO11:4 , which could stem from overlap with a very small thin film reflection at lower angles than observed for the other series.

The data table in Appendix 1A.3 specifies the result for each thin film in all the different pulsing ratios, and is briefly summarized in Table 5.2:

Table 5.2 Summary of all deposited NdNiO$_3$ thin films, emphasizing the number of samples (out of total ones deposited) that exhibits thin film reflections in their diffractogram.

Series	Pulsed ratio (Nd:Ni)	Number of samples with thin film reflections present in diffractogram
Stoichiometric ratio	3:1	5 out of 6
Stoichiometric ratio multiples	6:2	1 out of 4
	12:4	2 out of 3
	24:8	Outlier
Stoichiometric ratio multiple variations	5:2	1 out of 2
	7:2	2 out of 3
	11:4	Outlier
	13:4	0 out of 1

The pulsing ratios 6:2 and 13:4 did generally not result in crystalline thin films, while the 11:4- and 24:8-pulsed films showed thin film reflections but at unexpected angles. Instead of diffraction from NdNiO$_3$(*00l*)-planes, they instead showed a strong reflection at ~43.3 °, as seen in
Figure 5.9. This corresponds perfectly with the (200) Bragg angle for NiO with NaCl structure-type.

All of the films that generated thin film diffraction reflections are out-of-plane oriented since only the subset of (00*l*) reflections appeared in the diffractogram. Although out-of-plane orientation is unlikely to occur without in-plane orientation, the latter cannot strictly be confirmed with this measurement geometry (refer to 3.2.4 for an in-depth explanation). Results should thus be substantiated by further structural characterization, such as RSM.
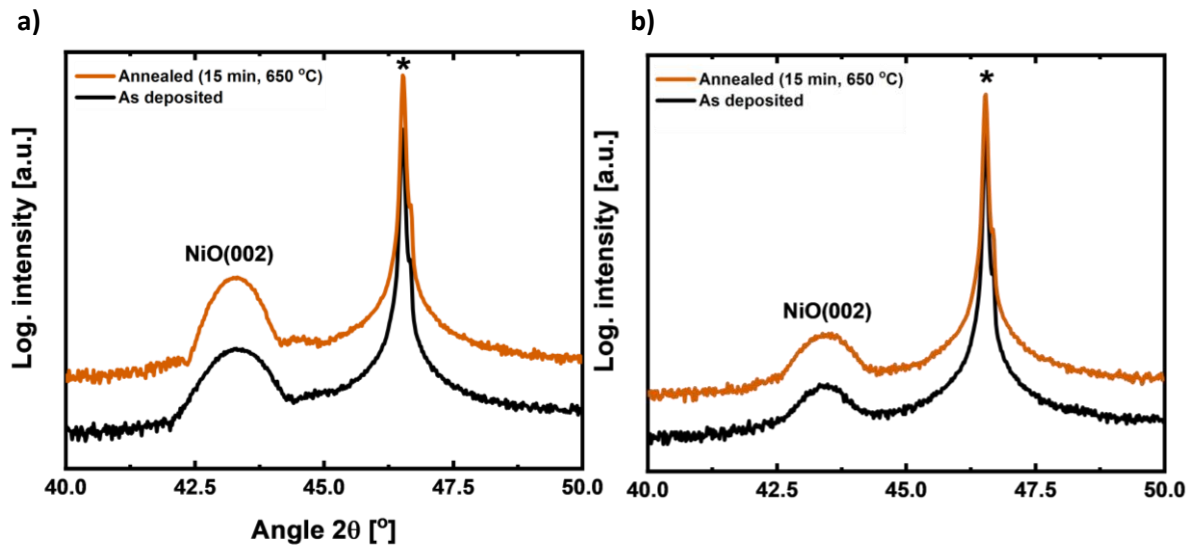
*Figure 5.9 X-ray diffractogram for **a)** 11:4-pulsed and **b)** 24:8-pulsed NdNiO₃ thin films on SrTiO₃(001), as deposited (black line) and after annealing in air for 15 minutes at 650 °C (orange line). The most intense reflections stem from the substrate, marked with asterisks, with an NiO(200)-reflection at 43.3 °, labeled as (hkl).*

To confirm whether the observed out-of-plane orientation was a result of epitaxy or not, the in-plane alignment of lattice planes was investigated with RSM for the non-specular (103) reflection. Figure 5.10 shows the results from a 7:2-pulsed sample, which was chosen for the purpose of being able to compare the RSM results before and after annealing. The reciprocal space map obtained for the 3:1-pulsed thin film whose diffractograms are shown in Figure 5.7 can be found in Appendix 1A.4.

The substrate reflection is the most intense and is not centered around the exact same $q_{||}$ value as the thin film reflection, meaning the film is partially relaxed both before and after annealing. The red x on each reciprocal space map indicates the expected center of the thin film reflection for bulk NdNiO₃, which occurs at higher $q_{||}$ and lower $q_{\perp}$ than for the thin film. This is yet another good indicator that the films are in-plane stretched out-of-plane compressed compared to a bulk unit cell.

The intensity of the thin film reflection visibly increases, which can be quantified by the full-width at half-maximum value (FWHM) for the reflection in the regular θ-2θ diffractogram. For the film as deposited, FWHM = 0.661, whereas after annealing it decreases to 0.605, corresponding to a narrower peak with less angular variation.
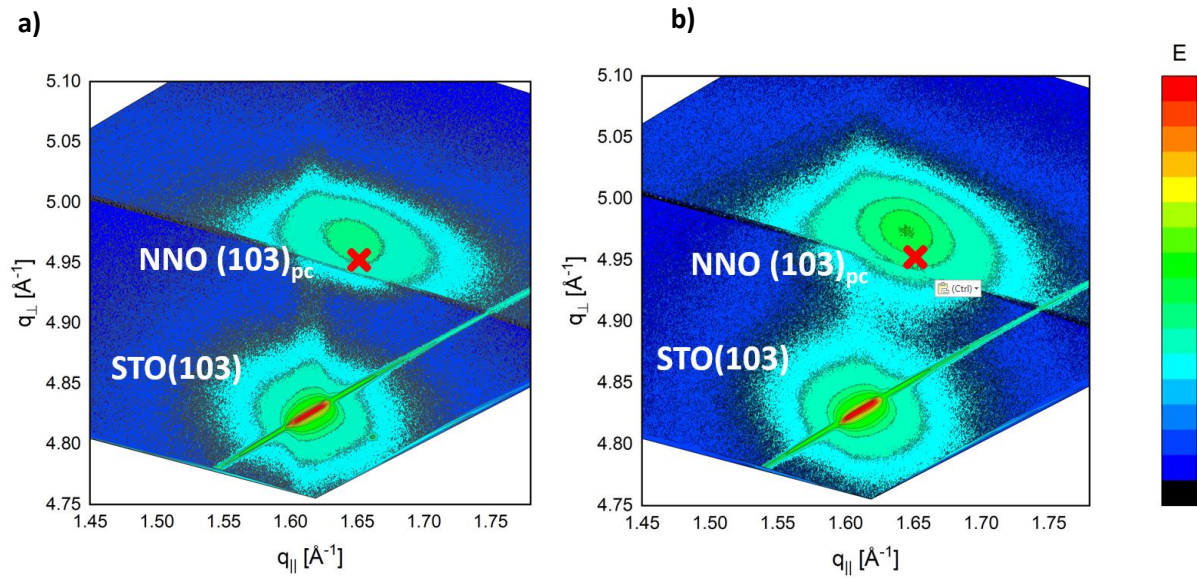
*Figure 5.10 Reciprocal space maps for the (103) reflection of NdNiO₃ on SrTiO₃(001), **a)** as deposited and **b)** after annealing in air for 15 minutes at 650 °C (right). The q∥ values for the substrate and thin films reflection differ, indicating that the film is partially relaxed. The red x marks the center of the reflection as calculated for the bulk.*

Another feature of RSM is that, when converted from Q_x and Q_y to $Q_∥$ and $Q_⊥$, respectively, it decouples the in-plane and out-of-plane lattice parameters so that they can be deduced individually. In the reciprocal space maps for the (103) reflection, the value of $Q_∥$ at the maximum intensity corresponds to the a and b lattice constants, which are equal since STO is cubic, and the value of $Q_⊥$ at maximum intensity equals one third of the c lattice constant in real space.

Calculations revealed that the in-plane lattice constants (a = b) were 3.818 Å for both the as-deposited and annealed samples. The out-of-plane lattice constant was 3.797 Å and 3.792 Å for the as-deposited and annealed sample, respectively. Compared to its unit-cell in bulk (a_{pc} = 3.807 Å), the thin film is 0.29 % in-plane tensile strained and -0.45 % out-of-plane compressive strained. With respect to the STO-substrate (a = 3.905 Å), however, the in-plane tensile strain is 2.23 %.

This aligns well with expectations since an in-plane elongation must be compensated for by an out-of-plane compression to maintain a nearly constant unit-cell volume. It is also plausible that compression is significantly larger because the in-plane strain is applied in two directions and contraction occurs only along one axis. Although this largely preserves the volume, it presumably affects bond angles to a greater extent since such a change imposes *changes* for the octahedra. That is why strain has been identified as an effective tuning knob for functionalities in structure-dependent materials such as the rare-earth nickelates.

The in- and out-of-plane strain derived lattice parameters from the reciprocal space map is more macroscopic in nature since they concern the thin film as a whole. The crystallite strain can be deduced from Williamson-Hall analysis of the regular θ-2θ diffractogram, which also makes it possible to calculate an estimate for crystallite size.

Williamson-Hall analysis is based on the contribution of instrumentation, crystallite size and crystallite strain to the broadening (β) of the XRD peaks, which can be regarded as summative:

$$\beta_{total} = \beta_{instrument} + \beta_{size} + \beta_{strain}. \hspace{3cm} \text{Eq. 3}$$

By assuming that the instrumental contribution is negligible the observed peak broadening becomes a direct result of crystallite strain and size. The full derivation of this to the expressions is provided in Appendix 1A.5.

$$\beta_{observed} \cos\theta = \frac{k\lambda}{D_C} + 4\epsilon \sin\theta. \hspace{3cm} \text{Eq. 4}$$

This resembles a linear equation of the form y = a + bx in a plot of $\beta_{observed} \cos\theta$ vs. $4\sin\theta$, where the y-intercept ($4\sin\theta$ = 0) can be used to solve for the crystallite size, D_C, and the slope gives the strain, ϵ. The broadening is estimated as the full width at half maximum (FWHM) of a Gaussian model fitted to of each diffraction reflection.

The result of the Williamson-Hall analysis for the same 7:2-pulsed sample that RSM scans were made on, is shown in Figure X for the three reflections that appeared in the diffractogram. Strain is equivalent to the slope, which is 1.78×10^{-3} [dimensionless quantity] and the crystallite size was calculated to be 31.9 nm.

In this context, the Williamson-Hall estimated crystallite size is the thin film thickness, assuming that crystallites traverse from interface to surface. 31.9 nm exceeds the experimentally measured thickness (using SE), which averaged around 25 nm. This size overestimation can have some possible causes. First, thin film thicknesses were measured with the spectroscopic ellipsometer, while Williamson-Hall analysis is based on X-ray diffraction data obtained from thin films on single-crystal STO. It is not unreasonable to expect that STO, being a perovskite, could facilitate different growth that results in thicker films than those measured on Si. The other factor to consider is the dimensionless shape factor 'k' in the calculation for size. This shape factor is a constant of proportionality that depends on the assumed crystallite shapes –but has been shown to approximately equal unity. The accuracy of this, however, diminishes the more the crystallite shape deviates from perfectly symmetrical (imagine a sphere). For a thin film, with highly directionally defined axes, k would be smaller than 1 and thus lead

to a smaller predicted size. The exact and correct value for thin films has never been experimentally determined, so the effect it would have on the actual result is speculation.
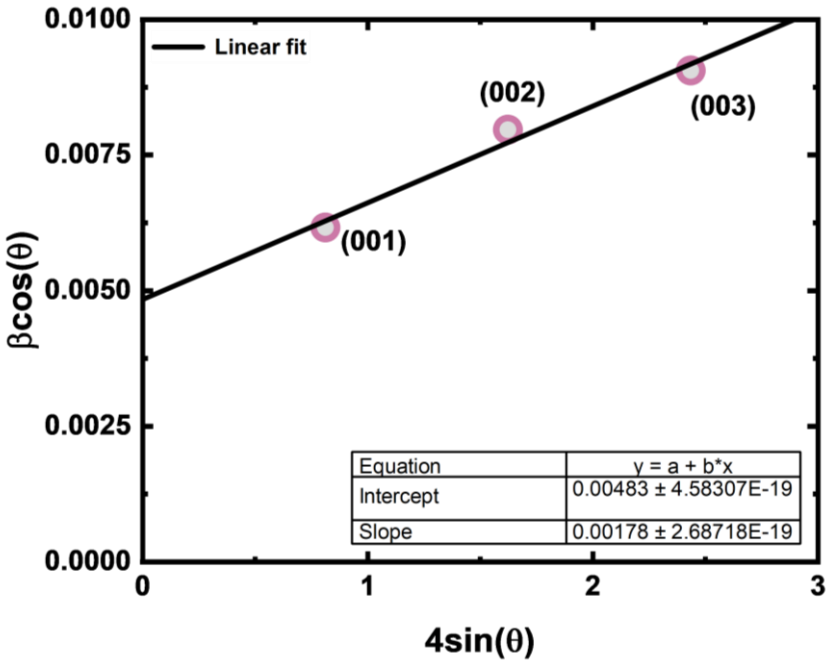
Figure 5.11 Williamson-Hall plot for a 7:2-pulsed thin film, with a linear fit fitted to the (001), (002) and (003) reflections of the thin film. The linear equation can be used to deduce the crystallite size (y-intercept) and strain (slope) can be deduced. The positive slope is in agreement with the tensile strain imposed on the sample.

5.2.2 Electrical characterization

Electrical characterization was performed by measuring room-temperature resistivity for all films and temperature-dependent resistivity with the PPMS for one of the NNO3:1 samples. Unless otherwise specified, the experiments were carried out at room temperature.

While four-point probes measure resistivity with a high degree of accuracy, using a single reading to represent the whole sample is not necessarily as accurate. Since the physical and electronic topography of the thin film surface depend on a variety of factors during the deposition process, they are expected to exhibit local variations. The landscape of sheet resistances across the film surface was probed with the 25-point probe for different pairs of pins, indicated by the arrows in Figure 5.12 a). The real three-dimensional electronic topography is visualized in Figure 5.12 b), where a cut-off limit has been implemented to remove anomalies that distorted the scale.

a)

b)
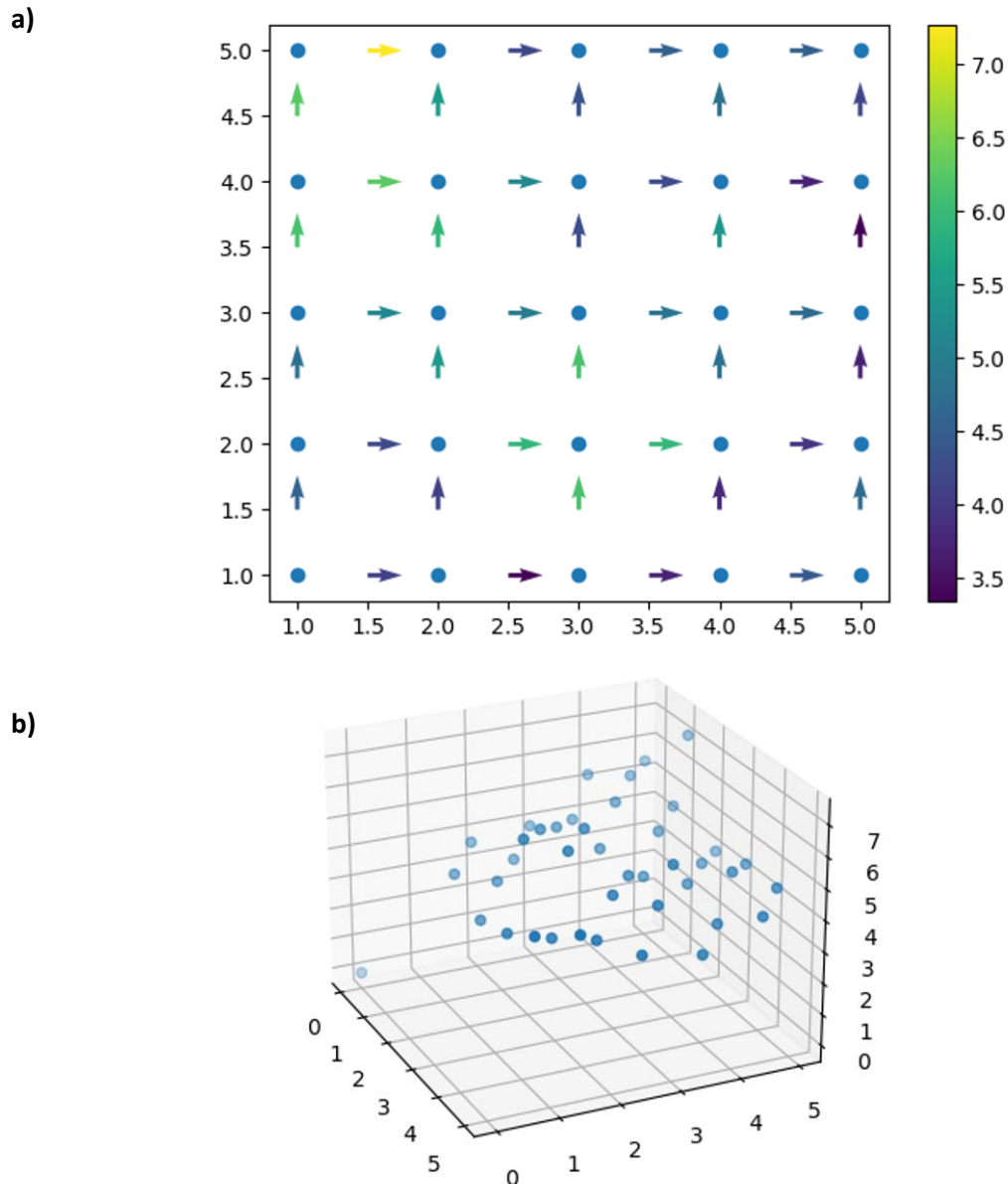
*Figure 5.12 Results from a 25-point probe measurement on a 7:2-pulsed NdNiO₃ thin film on SrTiO₃(001) illustrating the variation in thin film conductivity on the surface. **a)** 2D contour plot showing the logarithmic sheet resistances between pairs of probe pins, with the measurement direction given by the arrow. **b)** 3D plot visualizing the electronic topography of the thin film's logarithmic sheet resistance. Logarithmic values were used to better gauge the variation on a scale that applies to the thin films in this work.*

The measured data was plotted logarithmically to get a better impression of the intrinsic variations rather than the absolute values at each point on the film. It should also be noted that the point close to (0,0) in Figure 5.12 b) is programmed to be there to extend the axes down to zero.

There are indeed variations in the sheet resistance that are expected to have influenced regular four-point probe measurements, as the resistivity would depend on where the probes were placed on the surface. For example, a band of higher resistances seem to stretch across the diagonal of the film, meaning that measurements performed across or parallel to this band may differ noticeably. It is interesting to see that edge effects cannot be discerned to the extent that might be expected.

While 25-point probe data could have been used to complement the remaining electrical characterization, it is presented here mostly to provide a lens to see the following results through. It is also helpful in getting a more intuitive sense of the intrinsic variations that exist at the surface, and to recognize that these will always form the backdrop for four-point probe results even when they are not made explicit.

The resistivity of stoichiometric (3:1) thin films on single-crystal STO was generally low, in the range of 10^{-3} to 10^{-1} Ωcm as deposited, which was reduced to 10^{-4} Ωcm after annealing. Figure 5.13 a) shows the range of resistivities that was obtained with the stoichiometric ratio multiples and ratio variations as well. The different ratio multiples of the stoichiometric composition tended to result in films with resistivities on the same order of magnitude, except for NNO13:4 and NNO24:8, whose annealed film resistivities were comparable to the other films' as deposited resistivities. The variation in resistivity for films as deposited was reduced after annealing, but they do not become as uniform as the logarithmic scale gives the impression of. In Figure 5.13 b), one can see the differences for annealed films more clearly with a linear y-axis. Note that NNO13:4 and NNO24:8 were excluded from this figure because the magnitudes of their resistivities warped the scale.

One of the NNO3:1 thin films had an as-deposited resistivity (purple symbol) that was almost as low as the other film resistivities after annealing. It is an anomaly that would be worth looking into.

Whereas Figure 5.13 shows the resistivity as a function of the nominal composition of the film (in terms of pulsed ratio), it would be more interesting to see if there is a relationship between resistivity and actual film composition.
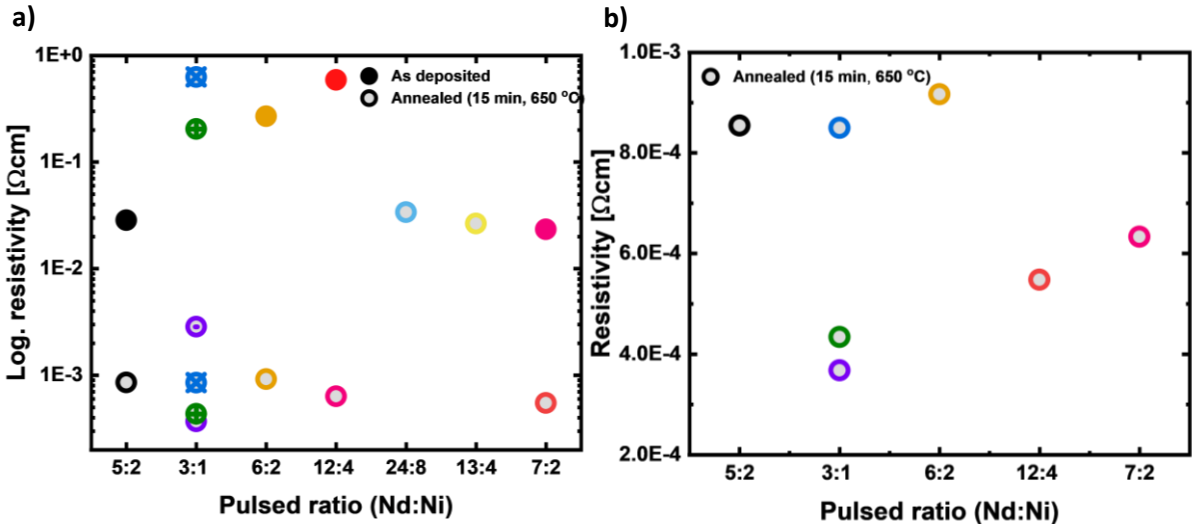
Figure 5.13 Comparison of the room-temperature resistivities in NdNiO₃ thin films deposited on SrTiO₃(001) with different pulsing ratios between Nd(thd)₃ and Ni(acac)₂. Filled symbols represent the samples as deposited and open symbols after annealing at 650 °C for 15 minutes in air. Different symbols were used for the 3:1-pulsed films to be able to better distinguish them from one another. Figure to the right shows the resistivities of annealed films (excluding 13:4 and 24:8) on a linear scale.

Based on Figure 5.14, which describes the composition through the Nd content as a percentage of total cation content, no such dependency seems to exist. The decrease in resistivity upon annealing the film also does not seem correlated with Nd content or film composition. This suggests that while the specific arrangement of the precursor pulses, in the form of pulsing ratio and order in the deposition, can facilitate compositional tuning and crystallinity, it does not directly affect electronic properties. Structural considerations may be a more important consideration for that.
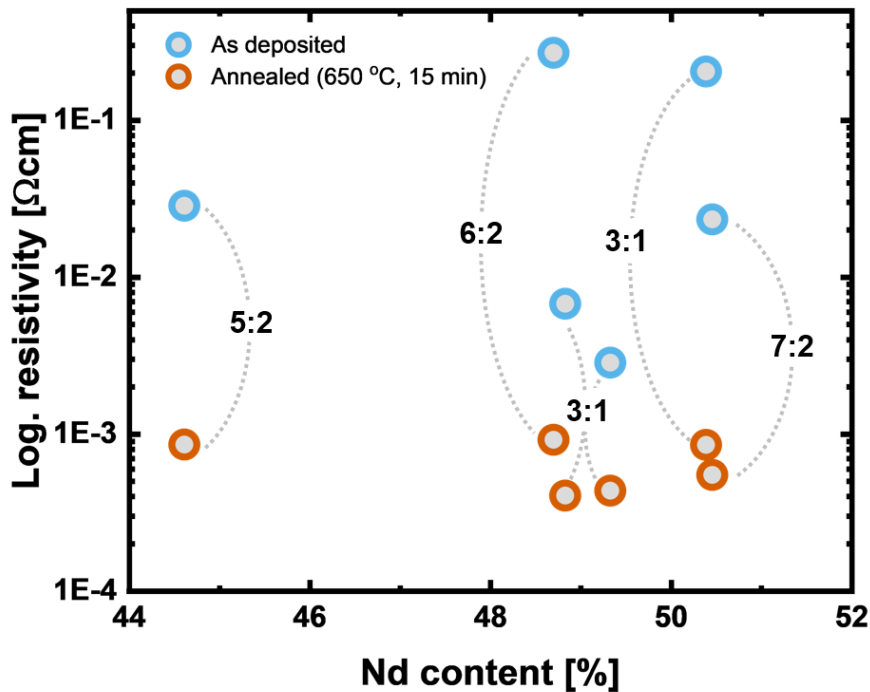
Figure 5.14 Room-temperature resistivity as a function of deposited Nd content (% of total cation content), in which the latter was determined with x-ray fluorescence.

Well-conducting films, *i.e.*, low resistivities, correspond well with the anticipated metallic state that $NdNiO_3$ should exist in at room temperature. Temperature-dependent resistivity was obtained to be certain that this is the case.

A stoichiometric 3:1-pulsed thin film (whose room-temperature resistivity is denoted by the green symbols in Figure 5.13) was heated to 225 °C and cooled down to 25 °C at increments of 50 °C. This was done for the as-deposited sample and repeated after annealing, with the resulting differences shown in Figure 5.15 a).

There is a fairly linear increase in resistivity with temperature both before and after annealing. The overall resistivity decreases significantly after annealing, which is in agreement with the trend observed for all the thin films.

Displaying only the resistivity of the annealed sample, as in Figure 5.15 b), it is evident that the temperature-dependence is perfectly linear both upon heating and cooling. The discrepancy in resistivity in these two states diminishes as the temperature increases, with the cooled sample being slightly less conductive.
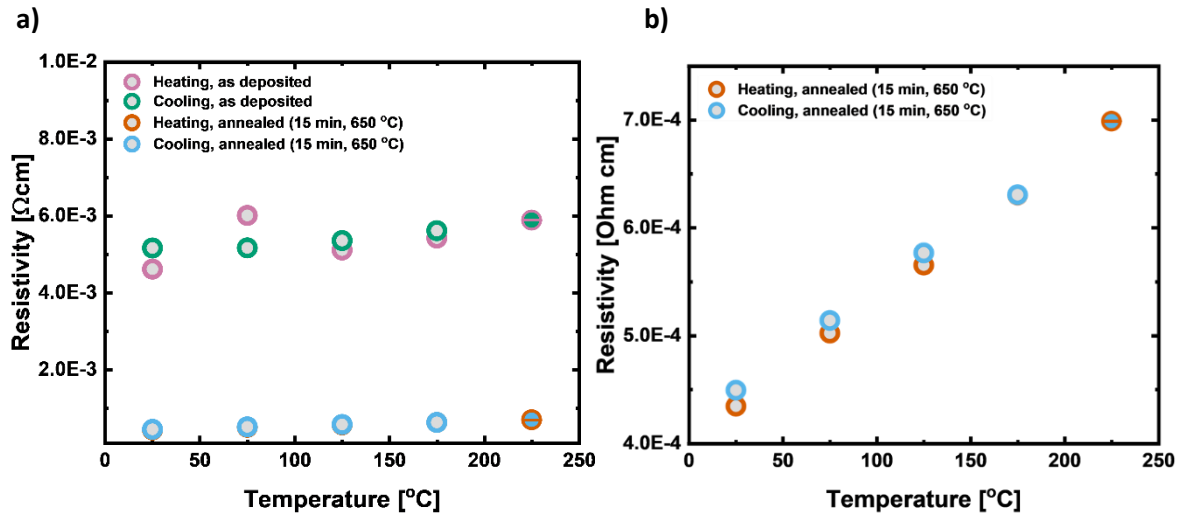
Figure 5.15 Temperature-dependent resistivity measurements (obtained with a temperature-varying 4-point probe) for stoichiometric (3:1-pulsed) NdNiO₃ thin films on SrTiO₃(001). **a)** *The resistivity of as-deposited (squares) and annealed (circles) thin films was measured from 25 ℃ to 225 ℃ and back down at increments of 50 ℃. Annealed samples were heated at 650 ℃ for 15 minutes in air.* **b)** *Enlarged version of the resistivities for the annealed sample.*

The lack of a drastic change in resistivity (typically several orders of magnitude) confirms that the sample is metallic and the MIT must occur below room temperature. PPMS measurements were conducted on another stoichiometric 3:1-pulsed sample after annealing to see if any signs of the MIT could be discerned and, if so, at what temperature.

Figure 5.16 shows the normalized resistivity as a function of temperature, with an abrupt change in resistivity that signifies the onset of the MIT. The temperature at the inflection point of $d\rho/dT$ corresponds to the T_{MIT} and was found to be 140 K during cooling. Measurements of other samples (one as-deposited and one annealed 7:2-pulsed thin film) were intended, but had to be indefinitely postponed due to a breakdown of the instrument (still down as of completing the thesis).

There is clear evidence of hysteretic behavior around the MIT region, with the resistivity at a given temperature depending on whether the sample is being heated or cooled. This is indicative of a transition's first-order nature. During both heating and cooling the resistivity changes by slightly more than one order of magnitude. The greatest change is seen while heating the sample back to room temperature, accompanied by a noticeable upward "shift" in the T_{MIT}, from 140 K to 175 K.
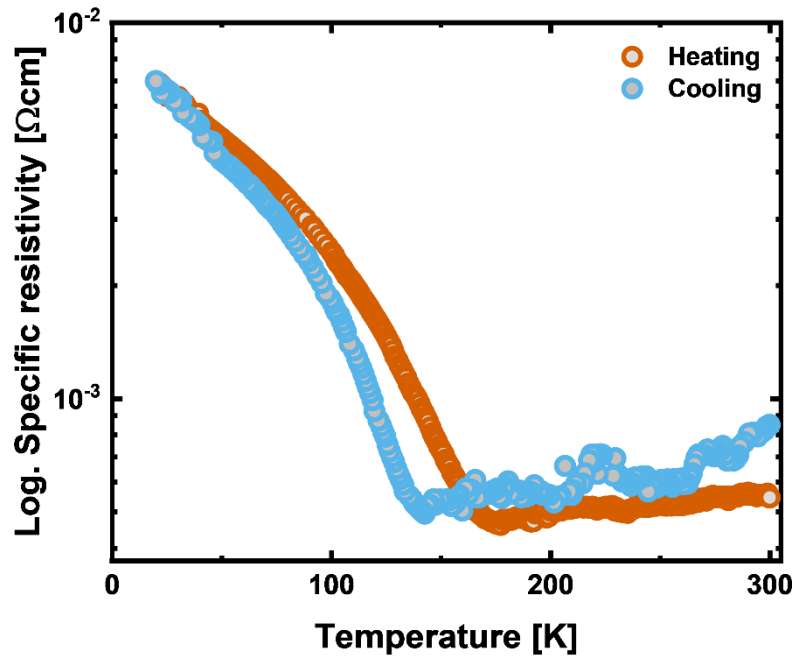
Figure 5.16 Normalized temperature-dependent resistivity (obtained with the PPMS) in a 3:1-pulsed NdNiO$_3$ thin film on SrTiO$_3$(001), measured while cooling (blue circles) to 20 K and heating (orange circles) back up to 300 K at a rate of 5 K min^{-1}. The sample had been annealed at 650 °C for 15 minutes in air.

5.2.3   Summary

The strong structure-property relationship in perovskites could clearly be observed in the structural and electrical characterization data for stoichiometric NdNiO$_3$ thin films and their stoichiometric ratio multiple variations.

Thin film conductivity was strongly correlated with crystallinity and improved after annealing on the order of two to three magnitudes. Annealing promotes crystallinity by increasing mobility of the constituents and enabling them to rearrange and form the most optimal structure. Grain boundaries can hence be reduced, removing structural defects that otherwise impede electron transport.

Although all crystalline thin films were out-of-plane oriented, RSM studies indicate that they are likely not be fully strained in-plane and can therefore not be concluded epitaxial.

One of the best conducting films was deposited with a 3:1 ratio, but this pulsing scheme did not consistently yield the lowest resistivities. No relationship between resistivity and Nd content in the film could be discerned for films of different pulsing schemes.

From the PPMS results, there is an evident MIT at 140 K with significant thermal hysteresis.

5.3 Tuning the Metal-Insulator Transition Temperature with Rare-Earth Substitution

An MIT was successfully demonstrated in one of the stoichiometric 3:1-pulsed samples, but with a T_{MIT} of 140 K (at cooling), which is significantly lower than ideal (room temperature). The third aim was therefore to map the effects of rare-earth substitution of Nd to see if this could tune the T_{MIT}.

5.3.1 Rare-earth substitution schemes and chemical composition

A range of rare-earth elements was substituted into $NdNiO_3$ by replacing one Nd pulse in the original 3:1, 5:2, and 7:2 (Nd:Ni) pulsing regimes to create new deposition pulsing ratios: 1:2:1, 1:4:2, and 1:6:2 (RE:Nd:Ni), respectively. These pulsing ratios were chosen because they proved suitable for crystalline, low-resistivity thin films of $NdNiO_3$ and were thus the most promising basis to begin from. The suitable pulse durations for each of the rare-earth elements were experimentally determined in a similar way as described in 5.1.1, with the data provided in Appendix 1A.6.

The relative amount of substituted Nd varies in these pulsing regimes, making it possible to observe the effect of substitution at varying degrees. From the total cation content the substitution schemes correspond to 33 % (1:2:1), 17.5 % (1:4:2), and 12.5 % (1:6:2) substitution. Substituting into the 6:2 pulsing ratio was not attempted since films in the pure Nd-Ni-O system did neither conduct nor become crystalline for this subcycle arrangement.

Unfortunately, the chemical composition of the thin films could not be quantified with XRF due to a lack of calibration standards for the binary rare-earth oxides. Results are therefore presented semi-qualitatively in terms of substitution degree and rare-earth element.

There are two exceptions, however: La_2O_3 and Sm_2O_3, for which calibration standards exist, making it possible to measure the average chemical composition of $(La,Nd)NiO_3$ and $(Sm,Nd)NiO_3$. The results for these samples pulsed with a 1:2:1 ratio are shown in Table X.

Table 5.3 Average chemical composition of $(RE,Nd)NiO_3$ samples (RE = La, Sm) pulsed with a 1:2:1 ratio (RE:Nd:Ni), obtained from XRF measurements.

$(RE,Nd)NiO_3$	RE cation content [RE/(RE+Nd+Ni) as %]	Nd cation content [Nd/(RE+Nd+Ni) as %]	Ni cation content [Ni/(RE+Nd+Ni) as %]
$(La,Nd)NiO_3$	27.5	28.9	43.6
$(Sm,Nd)NiO_3$	28.0	29.1	42.9

Even though the rare-earth element substituted one third of the original Nd-pulses, there is for all practical purposes equal amounts of RE and Nd in the films. Moreover, the total rare-earth content (RE+Nd) in the two samples is remarkably similar, with 56.4 % for $(La,Nd)NiO_3$ and 57.1 % for

(Sm,Nd)NiO₃. This suggests that similar growth processes characterize both systems, which seems reasonable considering that their cation radii are rather similar as well.

5.3.2 Room-temperature resistivity of (RE,Nd)NiO₃ thin films

The 1:4:2 (RE:Nd:Ni) pulsing scheme was explored first through structural (XRD) and electrical (4-point probe) characterization. Resistivities before and after annealing are shown in Figure 5.17 a), with asterisks to denote samples whose diffractograms contained visible thin film reflections. For reasons discussed in 4.3.3, this did not include all the rare-earth elements but the selection RE = La, Pr, Sm, Eu, Gd, Tb, Dy, Ho, Er, Tm, Yb.

Interestingly, there appears to be some trend for the resistivity of as-deposited thin films, which is shown separately in Figure 5.17 b) for better clarity. From RE = La to Ho, the resistivity increases by more than two orders of magnitude before suddenly dropping again, marking Ho as some turning point. Since many of the substituted samples did not conduct as deposited, it is uncertain whether the pattern is coincidental or can be extrapolated to the other rare-earths as well.
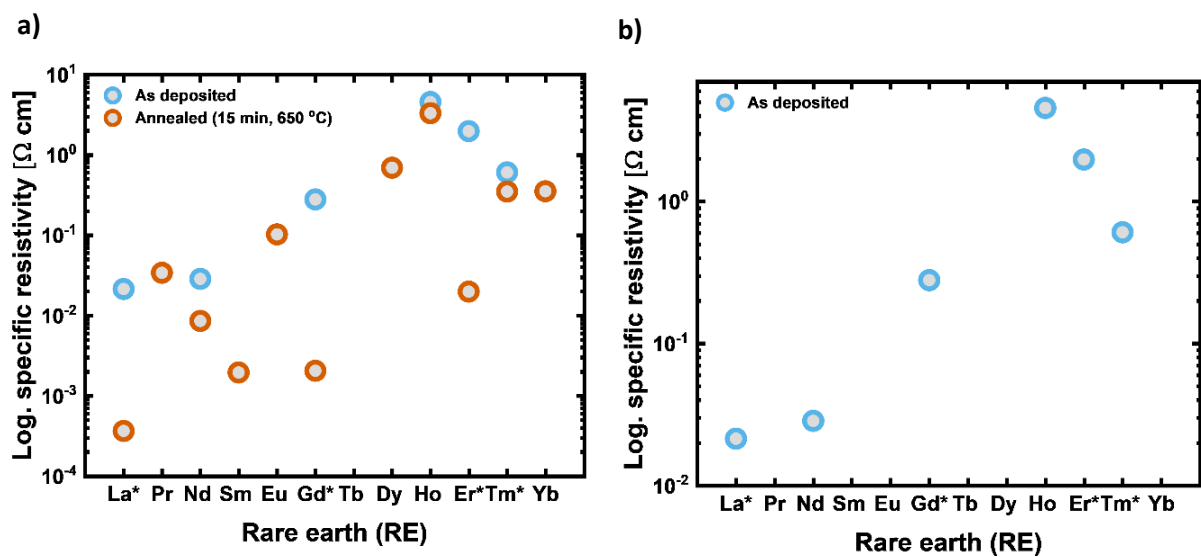
Figure 5.17 Room-temperature resistivity of rare-earth-substituted (RE,Nd)NiO₃ thin films deposited with a pulsing scheme of 1:4:2 (RE:Nd:Ni) on SrTiO₃(001). The rare earth is given on the x-axis. Samples were measured as deposited (blue symbols) and after annealing (orange symbols). The latter is also shown on a linear scale on the right. Rare earth cations with an asterisk exhibited thin film diffraction reflections before annealing.

Only a selection of the most interesting combinations was substituted into the 3:1 and 7:2 pulsing scheme. The evaluation was based on the criteria that films should *preferably* 1) conduct both as deposited and after annealing, and 2) be relevant for eventual T_{MIT} tuning. These two are not always compatible, but it was considered important to have a broader representation of the rare-earth elements than focusing on only the T_{MIT} would allow.

Figure 5.18 compiles all the resistivities for the different pulsing regimes to allow for more direct comparison. Note that this only includes annealed samples since as-deposited conductivity was very limited in the 1:2:1 and 1:6:2 pulsing schemes, but their resistivities can be found in Appendix 1A.7. $NdNiO_3$ is included to provide a benchmark for the other substituted thin films.
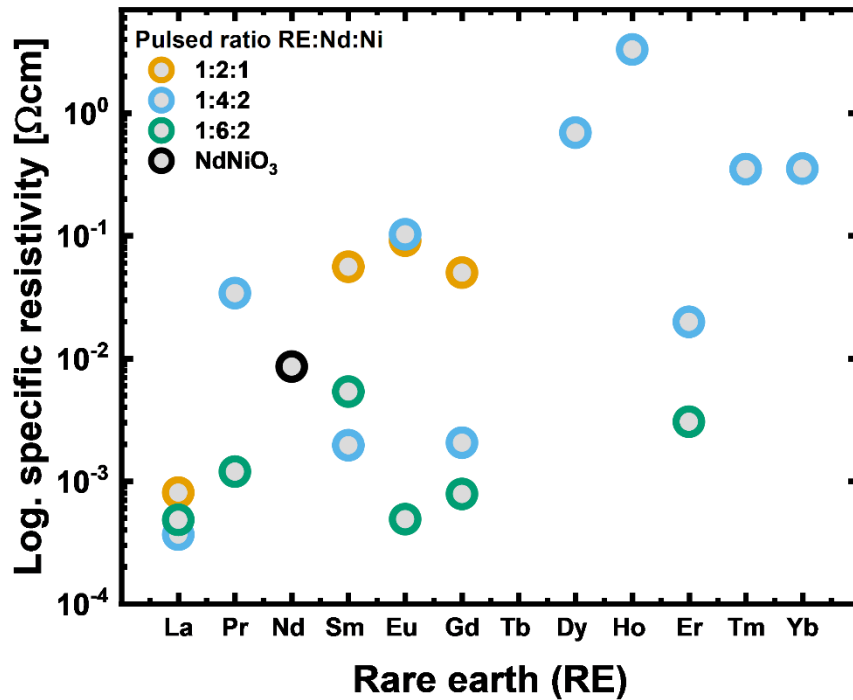
Figure 5.18 Room-temperature resistivities for $(RE,Nd)NiO_3$ thin films on $SrTiO_3(001)$ pulsed with the ratios 1:2:1 (yellow), 1:4:2 (blue), and 1:6:2 (green). The resistivity of $NdNiO_3$ (black) is shown for reference. All thin films have been annealed in air for 15 minutes at 650 °C.

From a general overview, it can be seen that the resistivity in films pulsed with the same ratio tend to be higher the greater the rare-earth substitution degree. That is, films pulsed with a 1:2:1 regime conduct relatively poorly compared to 1:4:2, and 1:6:2-pulsed films have the lowest resistivities with the exception of $(La,Nd)NiO_3$. However, the latter is somewhat of an anomaly compared to the rest of the substituted variants because it seems to conduct rather well for all pulsing regimes. Considering that $LaNiO_3$ is the one rare-earth nickelate member that does not undergo an MIT and remains a metal at all temperatures, this is neither unreasonable nor unexpected.

The sudden jumps and dips in resistivity between films with similar-sized rare-earth substituents in the 1:4:2 and 1:6:2 pulsing scheme is almost unpredictable enough to resemble a pattern. For 1:4:2-pulsed films a nearly linear increase was pointed out for the as-deposited films between RE = La and Ho. The resistivity of annealed films follows a much more erratic zig-zag behavior, but overall it too does increase from the smaller to the larger rare-earth elements.

The trend for 1:6:2-pulsed films could be qualitatively described as "wavy", as the resistivity increases from $(La,Nd)NiO_3$ to $(Sm,Nd)NiO_3$ before repeating itself in a similar way from $(Eu,Nd)NiO_3$ to $(Er,Nd)NiO_3$. Without having data that includes all possible rare-earth substitutions, and at least for the same ones here, it must be stressed that these observations are made on a very limited basis. With the 1:6:2 scheme, the resistivity is lower compared to the two other pulsing schemes, which may be a result of low rare-earth substitute content (theoretically 12.5 % of total cation). All of the diffractograms for this series exhibited clear thin film reflections both as deposited and after annealing (see Appendix 1A.7). This could suggest that the film behaves as a $NdNiO_3$ material with some degree of dopant that is small enough to not disrupt the average structure.

The 1:2:1 substitution scheme did include Er, but there is no data point for it since the thin film did not conduct, even after annealing. This contrasts strongly with the same sample in the 1:4:2 ratio where it was both crystalline and conducted as deposited. In fact, only $(La,Nd)NiO_3$ conducted as deposited in this pulsing regime. Even after annealing, all the resistivities remained significantly higher than in the two other substitution scheme, with the exception of $(Eu,Nd)NiO_3$ which is comparable to and slightly lower than with the 1:4:2 pulsing regime.

These films did not exhibit the same excellent crystallinity as previous stoichiometric films. Diffractograms are provided in Appendix 1A.8. For Sm-NNO1:2:1 there was a slight shoulder on the (001) reflection that was attached to the substrate reflection, but it was not as distinctly separate that it resulted in an individual thin film reflection. La-NNO1:2:1 and Gd-NNO1:2:1 had thin film reflections but at lower angles than pure $NdNiO_3$.

It is likely that the large degree of substituted Nd interrupts the structural integrity required to exhibit the desired electronic properties that were observed for the stoichiometric, ratio multiples and variations. This highlights the extreme difficulty of depositing a quaternary compound with ALD, as minute changes in growth parameters lead to drastic changes in the sample composition. *i.e.*, a new recipe must be fine-tuned for each single new compound.

Being able to see the resistivity data in terms of the actual amount of substituted Nd (equivalent to amount of RE incorporated) would make it easier to distinguish any relationship between the two.

5.3.3 Temperature-dependent resistivities for rare-earth substituted thin films

Compositions containing Nd and a rare-earth element larger than it are expected to have a higher T_{MIT} since it scales with the rare-earth cation size, as seen in their phase diagram. Temperature-dependent resistivity measurements were made on conducting $(RE,Nd)NiO_3$ films of the various substitution schemes.

Some of these were cycled, meaning the heating and cooling sequences were repeated several times to deduce whether the thermal history of the sample could lead to hysteretic effects or not. One such film was as-deposited $(Sm,Nd)NiO_3$ pulsed with a 1:6:2 pulsing regime, for three consecutive cycles between 25 ℃ and 125 ℃. Nickelate films consisting of Nd and Sm are especially relevant for T_{MI} tuning since their separate T_{MIT}s occur below and above room temperature, respectively.

Figure 5.19 shows how the thin film's resistivity at different temperatures ($\rho(T)$) varies in the three cycles. The graphs are constructed such that the last data point for the cooling cycle equates to the first data point in the following heating cycle.
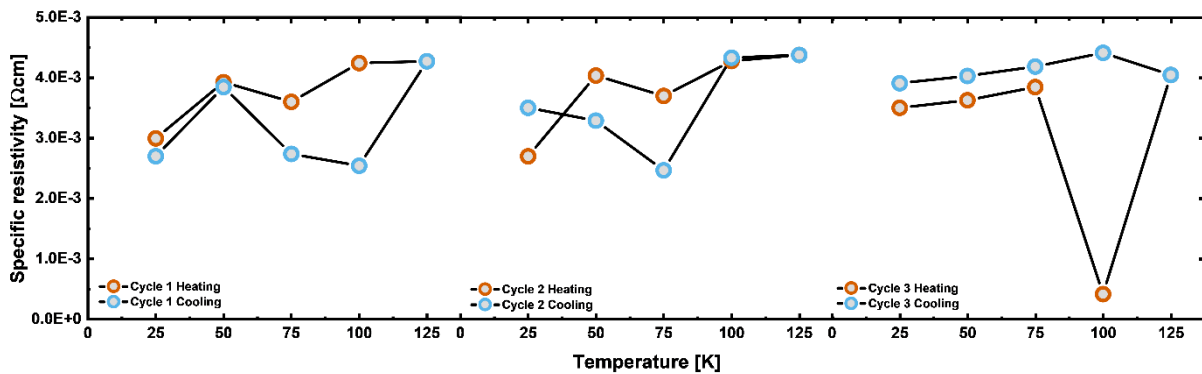
Figure 5.19 Three heating and cooling cycles from 25 to 125 °C for (Sm,Nd)NiO₃ deposited with a 1:6:2 pulsing scheme, prior to annealing. The last data point in a cooling cycle corresponds to the first data point for the successive heating cycle.

The resistivity remains on the same order of magnitude for all temperatures, with one anomaly in the third heating cycle, but the behavior is not very consistent otherwise. There is a certain similarity between the first and second cycles, but these in turn differ significantly from the third one. For instance, the resistivity upon heating follows the same pattern and is generally higher than when cooling the sample. This is possibly a result of Ohmic heating. In the third cycle, however, these parallel each other much more except for the sudden drop at 100 °C, and cooling the sample leads to a higher resistivity. It would not be unexpected that the thermal history of the film affects the film's electronic transport, but unfortunately it cannot be concluded based on this data alone.

During a regular temperature-dependent resistivity cycle from 25 °C to 300 °C (for the same sample as above) it was noticed that consecutive measurements made at the same temperature spanned a significant range, as can be seen from Figure 5.20. The lack of a systematic shift in the values obtained with measurement 1, 2, and 3 indicates that this variation is due to instrumental and measurement uncertainty rather than physically underlying phenomena. As such, this provides a picture of the random error one can expect in this type of measurement. In fact, when considering the maximal difference that exists in these measurements (approximately ±0.01 Ωcm) and applying these two the three cyclical ones, all of the data would overlap.
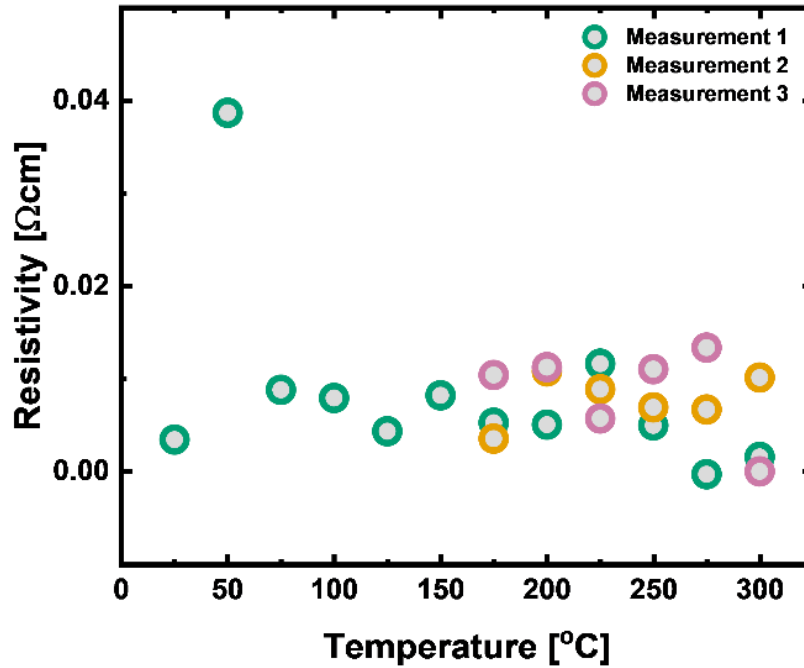
Figure 5.20 Variation in consecutive (not cyclical) resistivity measurements for 1:6:2-pulsed and annealed (Sm,Nd)NiO₃. The resistivity was measured three times in a row at higher temperatures in the order of 1 (green), 2(orange), and 3 (pink), as given in the legend.

Similar measurements were conducted for the other rare-earth substituted samples but exhibited the same type of somewhat erratic behavior. Consequently, most of the analysis becomes qualitative and a question of reliability.

Moreover, none of the resistivity-temperature curves displayed any signs of an MIT, *i.e.*, a drastic change in the resistivity.

5.3.4 Summary

Partial substitution of Nd with another rare earth cation seems to induce changes to the thin films that manifest in the structure and resistivity, with the significance depending on the degree of substitution. There was clearly an effect of the chemical disruption, and although the dependency on rare-earth size was not nearly as evident as in the rare-earth nickelate phase diagram, there were some interesting features and parallels that emerged. Temperature-dependent resistivities proved difficult to interpret reliably and lacked any signs of the MIT. A series of experiments on temperature dependent resistivity at temperatures lower than RT using the PPMS would likely shed light on the existence of an MIT.

5.4   Results Overview

Figure 5.21 shows an overview of the results that have been presented, set in the context and framework of the research plan from 4.3.
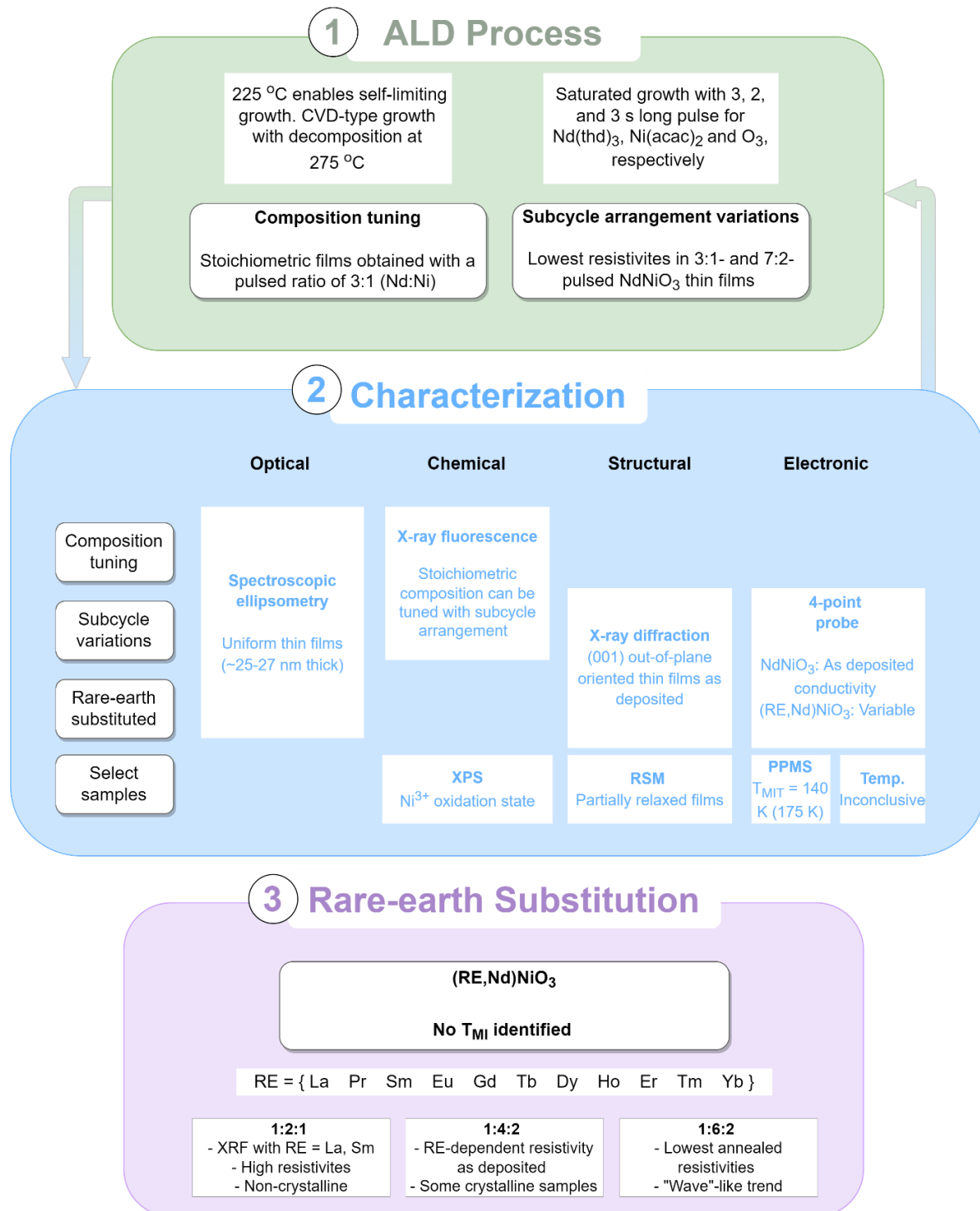
Figure 5.21 Schematic research plan as presented in 4.3, but updated with the work and main outcomes that have been presented.

6 Discussion

This chapter elaborates on the results that have been presented and draws parallels between findings in this work and that from previously published literature. Limitations, connections, and questions are brought up and made relevant for the objectives of the thesis.

6.1 Atomic Layer Deposition of Stoichiometric NdNiO$_3$ Thin Films

6.1.1 Multilayers and pulsing variations

The complexity and unpredictability of complex oxide depositions emerged quite readily when studying the effects of subcycle arrangement and pulsing ratios. Varying the pulsed ratio between Nd and Ni induced changes to the growth characteristics that manifested in the thin films' chemical, structural and electronic properties – all of which are closely related. The significance of precursor interactions and their changing environment in complex oxide processes has been emphasized repeatedly, and becomes very evident in the trends observed for the different pulsing schemes and series that were deposited.

Although the 3:1 ratio was deemed the most suitable for stoichiometric NdNiO$_3$ films from the original composition range, it can be seen from Figure 6.1 (which superimposes Figure 5.5 onto Figure 5.6) that NNO6:2 is the closest to a perfect stoichiometric composition. With 49.7 % Nd in the films it would be natural to expect these films to exhibit the best crystallinity and conductivity. Yet, the majority of deposited NNO6:2-samples (3 out of 4) was not crystalline enough to generate visible Bragg reflections in the diffractogram or conduct as deposited. The "neighboring" pulsing variations of 5:2 and 7:2 yielded low resistivities in the film and the Nd-content in NNO7:2 is almost the same as for NNO6:2 (with 50.46 % Nd). There are two possible conclusions to draw from this: either, the 6:2-depositions were particularly prone to experimental uncertainties ("bad luck") and the single crystalline sample is more accurate and representative of the series than it appears, or the average chemical composition can be a pointer towards optimal functionality but is not necessarily sufficient for tuning material properties.

Given how NNO11:4 is also an outlier from its *x*:4-pulsed series, it is likely that pulsing regime has a significant effect although it may not be entirely responsible for all observed variations. The fact that four consecutive Ni-pulses is enough to promote the NiO-phase in NNO11:4 but not NNO12:4 can almost seem too unlikely and it should be acknowledged that the film could merely be an experimental outlier. However, it only really appears as such after obtaining phase knowledge from diffraction studies and comparing its GPC to the rest of the series; based on Nd content alone it would be difficult to predict its discrepancies.
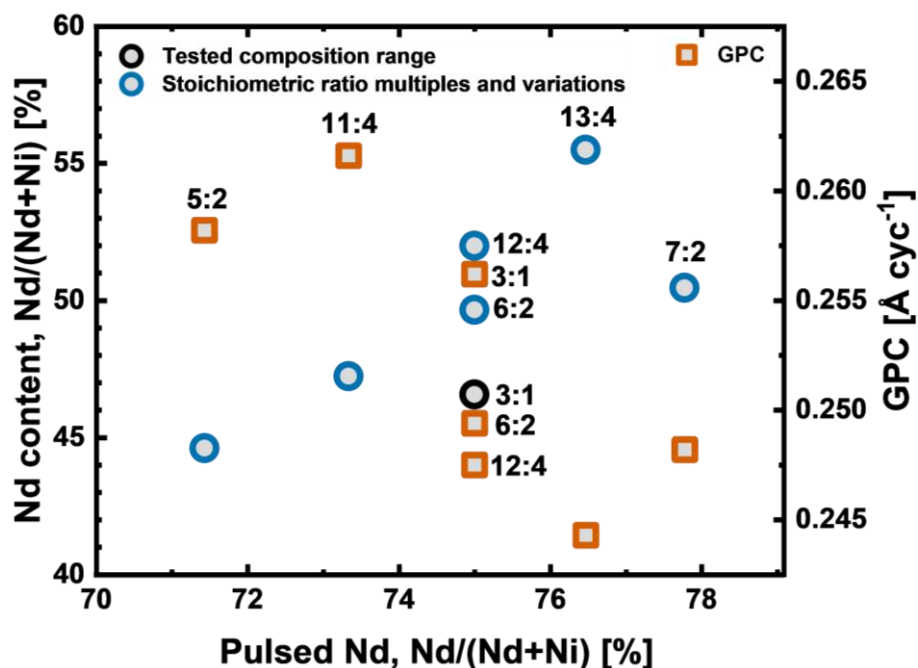
Figure 6.1 Compilation of two earlier figures (Figure 5.5 and Figure 5.6) for the purpose of comparing observations regarding the Nd content in the film (left y-axis) and growth per cycle (GPC per cation pulse, right axis) for different pulsed rations.

There is also a possibility that this exact pulsing scheme signifies some outer boundary for optimal ternary structure formation, whereupon the Ni-precursor molecules struggle to find active sites in the crystal that facilitates sufficient intermixing and diffusion to form the perovskite structure. NNO12:4 and NNO13:4 could, hypothetically, build up the layers in such a way that they more closely simulate an optimal structure, thereby also leading to lower GPCs. This indirectly points to one of the limitations of ALD: excess precursor that enters the chamber does not have any way to "escape" as long as there are available functional groups for it to react with, even if that results in an unfavorable stoichiometry that necessitates phase separation. This means that consecutive pulses of a single precursor will leave a footprint on the film, which can be both a benefit and a drawback. While it offers strategies for tunable properties, it also becomes necessary to be aware of and, ideally, control these parameters.

6.1.2   Previous atomic layer deposition of NdNiO$_3$

As mentioned in History and Prior Art (1.3), there are currently two published studies that have used ALD for deposition of NdNiO$_3$ thin films [3, 21]. These form a natural, albeit small, basis for comparison that is especially worth discussing considering how new the ALD route for NdNiO$_3$ is.

The studies resemble one another in that they employ highly reactive, liquid precursors (Nd(iPrCp)$_3$ (iPrCp=i-propylcyclopentadienyl) and Ni(tBu$_2$-amd)$_2$ (tBu$_2$-amd=N,Ndi-t-butylacetamideinato)) at low temperatures (160 °C) to deposit thin films. This temperature is outside of the possible range that can be explored in our depositions (due to the sublimation of Ni(acac)$_2$ at 185 °C), but they in turn rely on

post-deposition annealing to achieve crystallinity. While using highly reactive species can be beneficial from a temperature-perspective, it may be more difficult to realize the type of self-controlled composition that can be realized in optimal ALD processes [71]. Additionally, requiring post-deposition annealing conditions reduces the value of the inherent ALD characteristics that make it so attractive and unique for industrial process implementation, such as low temperature and the possibility of monolithic integrated circuits.

There are two points regarding the deposition temperature that should be addressed. First, their deposition temperature coincides with the reported evaporation temperature of the Nd-precursor in [21] and the Ni-precursor in [3]. Only Sun *et al*. discuss the rationale for choosing this temperature, which was the identification of a very narrow ALD window between 160 °C and 180 °C [21]. However, with equal deposition and sublimation temperatures the chance of precursor condensation (as opposed to chemical reaction) becomes a much more realistic problem. The temperature uncertainty is not stated, but there would likely be fluctuations that can cause the actual substrate surface temperature to deviate a few degrees above or below the set temperature.

Second, the specified ALD window is deduced from the growth per cycle for the binary oxides, rather than $NdNiO_3$ directly. Knowing that chemistry and growth of a ternary system often deviate from a linear combination of its binary processes, it is not certain that the same ALD window would be identified for $NdNiO_3$. As was discussed in 4.3.4, precursor interactions can change the dynamics of the ternary system, with remarkable evidence of this found in [72]. The decomposition of $Mn(thd)_3$ at 240 °C would be expected to define the upper applicable temperature range for the deposition of $La_{1-x}Ca_xMnO_3$; however, with the incorporation of La and Ca, the Mn-precursor was stabilized at higher temperatures, possibly due to the other metals relieving it of its ligands and preventing thermal decomposition. This truly illuminates the importance of investigating more complex systems independently, rather than as a superposition of constituent processes.

With the ALD process for $NdNiO_3$ being in the early stage of development, it is important to be aware discrepancies (and similarities) from other studies and try to reconcile the mechanisms and processes underlying the different results.

6.1.3 NdNiO₃ on Si-substrates

Crystalline and eventually epitaxial $NdNiO_3$ on Si-substrates would be the ultimate end-goal in terms of making RNOs (and other perovskite oxides) compatible with and fully integrated in transistors. It was shown in 5.2.2 that $NdNiO_3$ deposited directly on Si(100) with its native SiO_2 layer intact resulted in amorphous films regardless of annealing. This was really what was expected since SiO_2 is amorphous and does not provide the structural template that single-crystal substrates, such as STO, do.

However, epitaxial NdNiO$_3$ on Si(100) has been realized using different combinations of buffer layers [6]. The largest resistivity change (four orders of magnitude) was found for Si/TiN/MgO/SrTiO$_3$/NdNiO$_3$ thin films, which exhibited an MIT between 150 K and 200 K depending on the film thickness. This can be used as an inspiration for future investigations of integration on Si to assist with temperature tuning and/or complete an value step in the direction of device integration.

6.2 Characterization of Physical Properties

6.2.1 Presence of NiO

The diffractogram presented in Figure X for 11:4 and 24:8-pulsed films showed a thin-film reflection to the left of the substrate reflection, which deviated from expected and previously observed behavior. The Bragg angle was in perfect agreement with that for a NiO(200)-plane, indicating that a secondary NiO phase has been formed in the films.

For multilayer depositions such as 24:8, this can be a plausible scenario the individual layers of the multilayer structure becomes so thick that effectively two phases are deposited. The thickness of each deposited Nd$_2$O$_3$ and NiO layer becomes significant enough to inhibit sufficient intermixing between Nd and Ni to form the ternary NdNiO$_3$ phase. A pure NiO phase may thus form due to local over-stoichiometry of Ni. Technically, the same can be presumed for Nd$_2$O$_3$ layers, but it may more difficult for this material to crystallize because of its symmetry incompatibility (trigonal vs. cubic) with the surface it grows on. Amorphous growth would explain the lack of signs of this phase in the diffractogram.

Why this also occurs for 11:4 is more mysterious, especially seeing that 12:4 and 13:4 pulsing regimes do not give the same result. It would have been helpful to know the chemical composition of the films to see if perhaps the Nd:Ni ratio is more skewed in the anomalous 11:4 and 24:8 films. However, it is likely that the individual layers in the film are of greater significance than the average chemical composition since a more homogeneous approach might still allow sufficient intermixing despite over-stoichiometry of Ni.

6.2.2 Strain effects from SrTiO$_3$

Resistivity measurements had to be done with films deposited on single-crystal substrates because the films would otherwise be amorphous and not conduct, and the conductivity of the substrate would interfere. A variety of substrates could have been used to open for comparisons between compressive and tensile strain, degree of lattice mismatch, or different substrate orientations (*e.g.*, STO(100) vs STO(111)). This was not prioritized in this work, however, since it mostly focused on the ultimate goal of tuning MIT characteristics.

Nonetheless, it is of interest to know how the STO(001)-substrate that films were grown on may have influenced their properties, especially electronic transport. Such analyses were not attempted in this thesis, but can be found in a multitude of studies with this exact question in focus.

STO imposes in-plane tensile strain on $NdNiO_3$ thin films, with a lattice mismatch of +2.51 %. The actual strain found in our films with respect to the substrate was 2.22 %. In a simplistic picture, this merely induces an out-of-plane contraction to maintain the unit cell volume, which can have consequences for electronic transport and exchange interactions by changing the Ni-O-Ni bond angles. However, the tensile strain also stretches the oxygen octahedra and the cavity in which the rather small Ni^{3+} ion is located. With an already unstable oxidation state of +3, this increases the ion's instability and, with sufficient strain, reduces Ni^{3+} to the larger-sized Ni^{2+}. Charge balance is maintained by introducing oxygen vacancies, resulting in the commonly observed oxygen non-stoichiometry $NdNiO_{3-x}$ for tensile strained thin films [5, 35, 41, 42].

While there appears to be a general agreement that tensile strain is closely related to oxygen non-stoichiometry, its effect on the MIT is largely disputed. Since oxygen vacancies would act as scattering sites in the metallic state, one might expect tensile strained films to exhibit higher room-temperature resistivity and T_{MIT}.

That does indeed correspond to experimental results obtained by Heo et al. [9]. In a study of oxygen deficiency and strain in $NdNiO_3$ thin films they observe an increase in unit cell volume and a concurrent upward shift of the T_{MIT} with oxygen vacancy content. Room-temperature resistivity was also the highest for the most strained films, which was on STO. However, their argument rests on the assumption that any changes to the MIT are caused by the tensile-strain induced oxygen vacancies when this has yet to be established.

The works of Tiwari et $al.$ [73] demonstrate the conflict of such an assumption rather well. In a similar study they also found oxygen deficiency to increase the T_{MIT}, owing to reduced Ni-O-Ni bond angles and consequently less orbital overlap. However, when investigating strain-induced tuning of the MIT they found that tensile strain lowered the T_{MIT}, while compressive strain increased it [6].

Of course, there are significant differences between these studies that could lead to seemingly contradictory claims, but they are regardless difficult to reconcile. To complicate matters further, the T_{MIT} has also been found to 1) decrease for both compressive and tensile strain [10], 2) be independent of oxygen stoichiometry (which supposedly only affects the MIT sharpness) [46], and 3) vary with thin-film thickness [6, 39, 74].

Ultimately, strain-effects on the T_{MIT} may depend on a balance between oxygen non-stoichiometry and octahedral distortion affecting bond angles. As of now, it is an effective yet unpredictable tuning knob for functionality, which has implications for this work. Since its influence on the T_{MIT} is inconclusive, it is possible that it played a role for the lower than expected T_{MIT} in our films.

A central question in this aspect is, what is the relationship between oxygen non-stoichiometry and strain? Pursuing an answer to this has been outside the possible scope of the current work.

6.2.3   Reciprocal space maps and lattice parameters

Reciprocal space maps indicated that the films were not fully strained in-plane to the STO(001)-substrate but were partially relaxed towards bulk. The in-plane lattice parameter (calculated to be 3.818 Å) remained constant after annealing, whereas the out-of-plane lattice parameter decreased marginally, from 3.797 Å to 3.792 Å. From these parameters, it is possible to calculate the *pseudo*cubic film parameter of the unstrained film with an assumed Poisson's ratio (v) of 0.3 (the elastic constant of NdNiO$_3$ is unknown [43]). The relation is given by Equation 5:

$$a_{pc} = \frac{2va_{\parallel} + (1-v)a_{\perp}}{1+v},$$ Eq. 5

 where $a_{\parallel}$ and $a_{\perp}$ are the in-plane and out-of-plane lattice parameters, respectively. The result is a$_{pc}$ = 3.808 Å (rounded), practically identical to bulk.

This aligns well with a simple *pseudo*cubic unit-cell volume calculation that, based on the RSM-obtained lattice parameters, comes out to be 54.9 Å^3, equivalent to a 0.5 % decrease from the bulk unit-cell volume of 55.2 Å^3. In other words, there has been a slight compression of the average unit cell, but it is rather small compared to the degree of lattice mismatch, and hence, tensile strain. For instance, with fully strained NdNiO$_3$ films on STO, the out-of-plane lattice parameter was 3.75 Å, yielding an increase in the unit-cell volume by 3.6 % [75]. These films were thinner (30 unit cells thick) and less prone to strain-relaxation than our thicker films [74].

The energetic expense of the strain is likely to have been mitigated by the formation of domains or defects, such as dislocations. A particularly interesting possibility are Ruddlesden-Popper (RP) faults, named after the discovery reported by [76]. Using the formulation of [77], these can be defined as antiphase boundaries at which the perovskite phase changes locally to the rock-salt type. Not only is the introduction of RP faults in perovskites recognized as a tensile strain-relieving mechanism [77-79]; they have also been observed specifically in NdNiO$_3$ thin films on STO(001) [80]. The reason they are closely associated with tensile strain in particular is that they lead to local lattice enlargement, much in the same way that oxygen vacancies do, and can thus help accommodate the film to in-plane stretching. Since our films were not significantly strained, there is no indication that RP-faults are

actually present; however, it is an interesting point to consider because RP-faults have been identified as a promising route for defect-engineering of functional properties in perovskite oxides [77].

There are also two interesting visual features in the reciprocal space maps, one of which is the black diagonal line that abruptly terminates the transition region from the substrate reflection to the film reflection (intersects the y-axis at around 5 Å). This is a recurring feature in reciprocal space maps obtained with this instrument and is as such an instrumental artifact.

The other diagonal, passing straight through the origin of the substrate reflection, may be a structural feature originating from the interface. While processing the data in so-called low-speed mode, the now straight line appeared as dashed and was thought to come from crystal truncation rods arising from the abrupt termination of the substrate surface against the film. These are particularly useful because their specific characteristics depend on the film structure and can be used to determine and reconstruct the atomic structure at the surface. Unfortunately, it was not possible to resolve these in the final reciprocal space map, making further analysis of them impossible.

6.2.4   Physical property measurement system and observed metal-insulator transition

The PPMS was intended to be used as a complement to more routine electrical characterization and to provide data that could be compared and analyzed in-depth. Unfortunately, this was suspended due to unforeseen problems with the "electronic heart" (Model-6000) of the instrument and only the measurement that was presented in 5.2.2 was obtained. The instrument is still down at the time of completing this thesis.

There is a specific difference between the PPMS and standard four-point probes that is of relevance and should be addressed here. The electrical connection from the sample to the measurement puck occurs *via* gold wires that have been contacted with silver paint. The additional parasitic resistance was not directly factored into the resistivity, but becomes enveloped by normalizing temperature-dependent resistivity to the measured room-temperature resistivity.

Since the T_{MIT} is derived from temperature-dependent resistivity data, this type of experiment is rather prevalent in literature on MIT characteristics or electronic behavior of $NdNiO_3$. The T_{MIT} found with the PPMS here (140 K) is significantly lower than in bulk (200 K), and the lowest of any value reported in literature (of NdNiO3 on STO). A question that emerges is, what parameters and variables in this work have contributed to this downward shift of the T_{MIT}? Strain and oxygen non-stoichiometry have already been discussed as potential strain-related sources, but it still does not explain why the magnitude of the shift is so much larger than ever previously observed (Table 6.1).

In fact, the lowest T_{MIT} was obtained with polycrystalline $NdNiO_3$ films on Si(001) (with native SiO_2) that were RF-sputtered at 250 °C. This deposition temperature is comparable to the one used here, and even though our films were not polycrystalline, it does in a way parallel the domains that can be assumed to have been formed in the relaxation process since our films were not fully strained.

Table 6.1 Overview of previously reported T_{MIT}s in $NdNiO_3$ thin films made with different deposition methods and on various substrates.

Deposition method	Substrate	Reported T_{MIT} [K]	Source
ALD	STO(001)	140	This work
PLD (650-750 °C)	STO(001)	200	[6]
		180	[75]
		160	[81]
		175	[7]
		162	[10]
	$NdGaO_3(001)_{pc}$	160	[48]
	$(LaAlO_3)_{0.3}(Sr_2AlTaO_6)_{0.7}$ (001)$_{pc}$	170	
RF sputtering	Si(001) with SiO_2	146 (T_D = 250 °C)	[82]
		184 (T_D = 600 °C)	

Interestingly, the hysteresis loop for the measured thin film is not closed in that sense that T_{MIT} coincides at the same temperature for heating and cooling. Instead, the TMIT defined from heating the sample is significantly higher, at ~175 °C. It could be a result of measurement error, but since the overall resistivity of the heated sample continues to be lower than for cooling, it can almost seem like the sample has responded to its thermal history. It does not yet show signs of typical memristive behavior, but cyclical PPMS measurements might provide an indicator of the origin for the open hysteresis loop.

6.3 Tuning the Metal-Insulator Transition with Rare-Earth Substitution

6.3.1 X-ray fluorescence of rare-earth substituted samples

As was briefly mentioned in 4.2.2, very little chemical information could be obtained about the substituted samples due to a lack of calibration standards for most of the rare-earth oxides. This was rather unfortunate since more quantitative analyses would have been possible if the chemical distribution between the different cations was known.

While it is possible to manually create calibration standards for the XRF, it is a time-consuming process that requires very accurate information on thickness, density and roughness. A more accurate way to obtain the same data is through XPS. However, that too is an extensive task since several compositions

between and including the members are needed, which is why it was considered outside of the scope of this task.

A discussion of the XRF measurements that were made is nonetheless valuable. It was observed that 1:2:1-pulsed thin films of $(La,Nd)NiO_3$ and $(Sm,Nd)NiO_3$ contained almost equal amounts of rare-earth, but it cannot be assumed that the same holds for nickelates with smaller rare-earth elements. As has been pointed out, the ionic radii of La^{3+}, Nd^{3+} and Sm^{3+} is in the same size range (106 pm, 100 pm and 96 pm, respectively) and the GPC of their nickelates reflects this. Therefore, they presumably experience their deposition environment relatively similarly in terms of steric hindrance, number of available active sites, and chemistry with the preceding surface layer. This does not necessarily apply to heavier and smaller rare-earth element and one should be careful to not extrapolate the data for the two measured samples to the rest of the series.

As with ternary systems, growth of a quaternary oxide does not necessarily correspond one-to-one with the pulsed ratio and this was evident from the chemical composition of $(La,Nd)NiO_3$ and $(Sm,Nd)NiO_3$ thin films. With practically equal amounts of substituent rare earth as Nd, it can be inferred that full mixing in the subcycle arrangement (as illustrated in Table X) facilitates excellent growth conditions for the RE-precursor.

A possible hypothesis is this: the first pulse of $Nd(thd)_3$ sees a completely Ni-covered surface, and, while there certainly are reactive seats for Nd to chemisorb onto, growth is not optimized because the different structure and arrangement of atoms in the preceding layer effectively reduces the density of possible reactive groups. A not fully dense monolayer is deposited, but in turn provides a more favorable template for the subsequent rare-earth (substitution) precursor. Owing to the chemical and physical similarities between Sm/La and Nd, the growth environment for $RE(thd)_3$ on Nd_2O_3 is probably almost interchangeable with $Nd(thd)_3$ on RE_2O_3 when RE = La or Sm. As such, the rare-earth pulse and the second Nd-pulse perceive a close to identical environment and exhibit similar GPCs, while the first Nd-pulse contributes less, in relative terms. This could be an explanation for why the chemical composition was what it was, but the situation might be different for other combinations of Nd and RE.

If the chemical composition could be determined for the same films with other pulsing regimes, then it might be possible to map out a composition range in the form of RE:Nd ratio pulsed vs. obtained in the film, similar to the one for pure $NdNiO_3$. Essentially, the challenge now is that we're working with two unknown variables at the same time: amount of RE incorporated into the film, and the RE size. Since these contributions cannot be separated, it is impossible to isolate their effects and ascribe observations to either one.

6.3.2 Room-temperature resistivity of (RE,Nd)NiO₃ thin films

For discussions pertaining to room-temperature resistivities in rare-earth substituted samples, it is helpful to refer to Figure X. A number of interesting observations could be made for the different substitution schemes, although the data appears somewhat chaotic.

One common observation for all substitution schemes was that thin films could conduct as deposited without showing crystallinity by XRD. This was never the case for films in the pure Nd-Ni-O system, although they sometimes became conductive after annealing. It is rather surprising that even with the structural disruption from the "foreign" rare-earth introduced in the system, electronic transport was enabled to the degree that it overcame the lack of crystallinity. Additionally, as-deposited conductivity only occurs for RE < Nd (in terms of size) and the presence of a smaller A-site cation would be expected to induce stronger octahedral distortions. This is the mechanism that leads to higher resistivities and T_{MIT}s for smaller rare-earth nickelates, so it is difficult to comprehend how it also seems to enable as-deposited conductivity. Unfortunately, the relationship between chemistry and structure could not be measured quantitatively, which could have provided more fine-grained nuances that might explain our observations.

This would have been particularly helpful for the 1:4:2 (RE:Nd:Ni) substitution scheme because it showed unique potential for tuning the resistivity with rare-earth cation type (size). For the films that conducted as deposited (RE = La, Gd, Ho, Er, Tm) there was a systematic increase in resistivity from La to Ho, after which it began to decrease. With the exception of (Ho,Nd)NiO₃, these films were crystalline as deposited.

The supposed pattern raises some questions about what this means and how it can be utilized. The nearly linear increase in resistivity with smaller rare-earth cation size aligns well with greater cation mismatches leading to a less ideal atomic packing in the perovskite structure. Again, this relates to reduced bond angles and orbital overlap, compromising electronic transport. This does not, however, explain the appearance of a turning point at Ho. Referring to the phase diagram in Figure X, it is evident that the tolerance factor decreases almost linearly moving from larger to smaller rare-earth nickelates, and there is no deviation from the pattern there that could indicate why (Ho,Nd)NiO₃ defines some boundary or limit. Whether this is due to unknown, underlying mechanisms or anomalies in the succeeding data points is difficult to establish based on the results obtained so far.

A research paper by Alonso *et al.* [83] might have been able to offer an explanation had it not been relatively outdated both in terms of age (1999) and general agreement. They postulated that the MIT mechanism in HoNiO₃ is different than in the other rare-earth nickelates they investigated (RE = Sm, Gd, Eu, and Dy) because it showed signs of Ni splitting into two distinct sites. As was briefly mentioned

in 2.3.2, this observation is recognized as closely associated with the structural transition, but for *all* rare-earth nickelate members [84].

Focusing on the films that conduct as deposited leads to another interesting observation. The degree to which resistivity decreases after annealing varies with several orders of magnitude, showing dependency on the rare-earth element that has been substituted in without it being systematic. Although the differences are likely a result of random factors associated with deposition (thickness gradients) and/or measurement (probe placement) parameters, they allude to an overarching question: how much can conductivity be improved and what determines it?

If it were a matter of structural optimization and compatibility with respect to the parent (host) $NdNiO_3$ perovskite, then resistivity should increase nearly linearly with size difference. How optimal the structure is also depends on growth conditions and ligand interactions that may vary from rare-earth to rare-earth. For instance, some of the rare-earth elements have the potential to adopt a +2 oxidation state, *e.g.*, Eu, Tm, Sm, and Yb. Although it is unlikely that it would occur under strong oxidizing conditions, it is notable that none of these substituted variants (except for RE = Tm) were found to conduct as deposited in the 1:4:2 pulsing scheme.

Many of the remarks that have been made about the resistivities for different degrees of substitution rely on qualitative observations and a limited data set to base them on. Replicating depositions with the same three pulsing schemes would make it possible to obtain some average and gauge the uncertainty associated with each resistivity. Any trends that potentially exist would likely emerge more visibly in that case.

6.3.3 Temperature-dependent resistivity

The reliability of the temperature-dependent resistivity measurement above room temperature was questioned in relation to the data collected for 1:6:2-substituted $(Sm,Nd)NiO_3$ thin films. In addition to the intrinsic variability that was identified for and with that particular sample, there are other sources of uncertainty and errors that should be addressed.

A systematic one is that the reported temperature is not necessarily the temperature at the thin film surface, the reason being that the reported temperature is based on the metal stage on which the thin film sits. This discrepancy should be reduced the longer the film is allowed to stabilize, but it is yet unknown what the minimum difference is. An estimated uncertainty of $\pm$ 2 °C is considered appropriate for the temperature reading, but the actual error associated with temperature is presumed to be systematically higher.

Substrate size must also be taken into consideration. On smaller substrates (5 mm $\times$ 5 mm), the four probe points only fit along the diagonal and this causes the outer pins to be situated close to the substrate edges. When sample size becomes comparable to the probe spacing (1 mm), it is possible to correct for the edge effect using a correction factor. Specifically, when the distance between the closest probe pin and a non-conducting boundary is less than 20 times the probe spacing, a correction factor becomes relevant [85].

The fact that temperature-dependent resistivity measurements did not reveal an MIT in (Sm,Nd)NiO$_3$ was a little unexpected. While the discussed sources of error and uncertainties certainly can affect the accuracy of a specific resistivity value, they would not conceal a change in the resistivity over one or several orders of magnitude. One hypothesis is that the unexpectedly low T$_{MIT}$ in the pure Nd-Ni-O system propagates into the substituted films as well. If that is the case, then it would appear in PPMS data that could go below room temperature.

6.4   This Work in Perspective

Many of the strategies and foci that occupy much of current research activity have been both directly and indirectly explored in this work. On the synthesis side, subcycle arrangement and growth characteristics of ternary and quaternary systems have particularly captured our attention, building on and corroborating previous findings of [57]. The observations we make regarding the various series of pulsed NNO*x:y* not only illuminate a future path of interest but also appear as very promising tuning knobs for functionality. With respect to deposition choices, we also allude to the potential implications that substrate strain may have had for our studies, noting that this is an ongoing debate whose history extends beyond the scope of this thesis.

This work also makes the only contribution, as of now, to MIT studies of RNO thin films deposited with ALD. Although there remains work to be done in this regard, it is the first step in introducing ALD to this research arena and that will hopefully prove fruitful in the future.

7   Conclusion

This thesis research aimed to evaluate the potential of using the MIT in $NdNiO_3$ for room-temperature electronics. Specifically, it was of interest to see whether high-quality $NdNiO_3$ thin films could be deposited with low-temperature ALD, which is more compatible with the technical conditions employed in industrial processes than other physical deposition methods are.

An ALD recipe for $NdNiO_3$ thin films was successfully developed and tested, with exceptional control of chemical composition and structural quality. Stoichiometric thin films were obtained by pulsing $Nd(thd)_3$ and $Ni(acac)_2$ in a 3:1 ratio and could be precisely tuned with the pulsing regime. Diffraction and RSM studies revealed crystalline, out-of-plane oriented thin films as deposited on single-crystal $SrTiO_3(001)$-substrates, with partial relaxation hampering the goal of full epitaxy. However, low-temperature (225 °C) epitaxy on par with MBE and PLD seems to be within reach for ALD. The stoichiometric samples also exhibited excellent electronic conductivity as deposited, with even lower resistivities $\sim 10^{-4}$ Ωcm after annealing.

An MIT at 140 K with thermal hysteresis was observed in one of the stoichiometric 3:1-pulsed $NdNiO_3$ thin films using the PPMS. This is significantly lower than room temperature and what has previously been reported in literature. Attempts at tuning the T_{MIT} were made by substituting other rare-earth elements for Nd to different degrees. With a nominal 12.5 % rare-earth substitution there was a distinct and interesting trend for resistivity in as-deposited thin films: the resistivity increased for RE = La to Ho and decreased for heavier rare-earth elements. XRF-measurements of La- and Sm-NNO1:2:1 showed almost equal RE and Nd content. Unfortunately, further quantitative analyses cannot be made until it becomes possible to analyze all of the thin films' chemical composition.

In light of the phase diagram for the rare-earth nickelates, $(Sm,Nd)NiO_3$ thin films were anticipated to be particularly promising for room-temperature T_{MIT}s. However, temperature-dependent 4-point probe measurements from 25 °C to 300 °C did not reveal any signs of an MIT in this temperature range and were not very consistent in terms of reproducibility. No other substituted variants exhibited MIT characteristics either, but there were some interesting qualitative observations that would have deserved some more consideration had time allowed it.

In summary, ALD of ternary $NdNiO_3$ and quaternary $(RE,Nd)NiO_3$ thin films proved a reliable synthesis route. With the optimal pulsing ratios, stoichiometric thin films were grown with reasonable crystalline quality and some of the RE-substituted variants were also out-of-plane oriented either as deposited or after annealing. The thin film properties were responsive to subcycle arrangement, but the exact tuning mechanism has yet to be illuminated. Rare-earth substituted films exhibited interesting resistivity trends but require access to chemical analyses before they can be understood better.

8 Future

Discussion of the results presented in Chapter 8 has identified areas of improvement as well as areas of interest for future studies. Although some of these have been introduced earlier, they are collected in this chapter for a collective assessment of the possibilities they may harbor. Visions for the work as a whole and its impact in the scientific community are also discussed.

8.1 Continuation of Thesis Work

The limitations of some of the characterization methods led to a few loose threads that would have been interesting to pursue had time and resources allowed it. This pertains particularly to the chemical characterization of rare-earth substituted variants, which was elaborately discussed in 6.3.1. Working around the problem by using XPS would be an extensive tangent to the original objective, but seeing how it might clarify the observed trends it could be considered worthwhile. The insight gleaned from these methods may be able to help us better understand how chemical characteristics govern the properties we aim to use and optimize.

A more immediate solution that was briefly suggested earlier is to repeat the different series of *RE*-NNO for greater experimental reliability. With only one sample for each composition, and knowing how the properties may vary even within the pure Nd-Ni-O system for NNO3:1 films, it is difficult to know how much to weight the observations regarding these thin films. Internal variation for single samples was already noticed in some of the temperature-dependent resistivity measurements, in which independently repeated trials resulted in very different results. Improvement in both conducting and analyzing the experimental work thus very much relies on identifying the most sources of uncertainty and determining how these affect the obtained data.

Improving the temperature range and certainty of the temperature-varying four-point probe would also open for more concrete and justified analyses. An important step in this direction would be to map a more static system that is not as sensitive to temperature or thermal history as some of the materials in this work may be. Since the temperature-varying probe is a fairly new addition to our available characterization methods, it is expected to need some groundwork before we are able to utilize its full potential.

Ideally, the PPMS could also have been used to a much greater extent. While repeated measurements for different pulsing schemes were intended from the beginning, performing cyclical heating and cooling cycles in a single measurement run was only considered after observing the unclosed hysteresis loop. This would also make it possible to see if the T_{MIT} shifted for sequential cycles, in which case the material may display memristive behavior. It would also be interesting to measure some of the rare-

earth substituted samples with the PPMS to see if the MIT appears at temperatures lower than room temperature. Considering the lower than expected T_{MIT} in stoichiometric $NdNiO_3$, a systematic shift affecting substituted thin films as well could be plausible.

It could be of utility to perform more elaborate RSM studies that tap into the possibilities of this instrument. First and foremost, it could be useful to obtain reciprocal space maps of other reflections to corroborate the results obtained from the (103) reflection. The primary reason this has not already been done is that the availability of many of the reflections was limited by the instrumental angular range. Another way to utilize RSM is by doing temperature-dependent scans, which shows the structural evolution of the film and substrate reflection as temperature changes. This could be used to narrow in on the appropriate annealing temperature for these films by identifying the range of temperatures over which the structure goes from amorphous to crystalline. RSM studies at synchrotron facilities may also be able to resolve the presumed crystal truncation rods and provide a new perspective on the substrate-film interface through atomic reconstruction of the film.

In future work it would also be of interest to broaden the scope by incorporating other advanced characterization methods. In addition to the structural, chemical, and electrical characterization that has been carried out and presented here, it would also be useful to study the film more locally. Optical techniques such as atomic force microscopy and transmission electron microscopy are highly applicable in this context. A general sense of the thin film surface uniformity was acquired by measuring the thickness of a single sample at several different points with the spectroscopic ellipsometer; however, this reveals nothing about surface morphology and topology. Features such as these can contribute to variations in properties or be a result of interface or structure effects that have propagated to the surface. As such, they may indirectly convey information that can be used to optimize the material, for example through deposition parameters. Atomic force microscopy can give a picture of surface topography and roughness, and more interestingly, this could potentially be coupled to an atomic force microscopy variation called scanning spreading resistance microscopy. In this mode, a conductive tip is used to measure the resistance of the surface in a scanning fashion and this could potentially evoke "responses" from microstructural defects or grain boundaries that might have arisen from strain relaxation. Since these interrupt the periodicity of the crystalline structure, they might lead to local increases in resistivity and could as such be used to map local variations in the thin film structure that are engulfed in standard XRD.

Transmission electron microscopy is better suited for studying the substrate-film interface. The latter would be particularly useful for seeing if the interface is sharp or diffuse, and also to observe how strain or relaxation propagates from the interface and through the film. Combined with energy dispersive spectroscopy, this can be a powerful way to examine the internal structure of and elemental distribution in the film close to the interface.

8.2   Expanding to Other Areas and Applications

Having only been reported twice in literature before (and also for different applications), the low-temperature synthesis of NdNiO$_3$ with ALD is a relatively novel contribution to research on rare-earth nickelates. It is the author's hope that this work can also be of relevance in other fields or for different applications than have been identified in the initial scope of this thesis.

The overall success of the synthesis pertains particularly well to a very new and very welcome discovery, which is the observation of superconducting infinite-layer nickelate thin films. Although it has now been discovered in (Pr,Sr)NiO$_2$ [86], (La,Ca)NiO$_2$ [87] and (La,Sr)NiO$_2$ [88], superconductivity in these copper-oxide analogues was initially realized in Sr-doped NdNiO$_2$, specifically Nd$_{0.8}$Sr$_{0.2}$NiO$_2$ thin films [89]. The process has consisted of doping Sr into NdNiO$_3$ thin films before topotactically reducing them in the presence of CaH$_2$, resulting in the square planar network that facilitates superconductivity in these materials.

There was initially variable success in reproducing the first results, presumably because synthesis of these materials is difficult, yet essential for realizing the strongly structure-related superconducting properties. Identifying a reliable low-temperature synthesis route with exceptional control of structure and chemistry would therefore be expected to stimulate research opportunities. Considering the success with low-temperature deposition of conducting, in-plane oriented quaternary thin films with stabilized Ni^{3+}, ALD appears as a unique and promising approach to base future research on superconducting nickelates off.

There are also some more specific results that seem worth delving deeper into. The stoichiometric NdNiO$_3$ thin films whose resistivity became more sensitive to temperature after annealing (see Figure X) underpin their potential for neuromorphic applications. This relatively new field may in fact mark the beginning of a paradigm shift in computing. As opposed to binary memory devices distinguishing between ones (on) and zeros (off), these analogue devices attempt to emulate the physics and pathways of the brain by mimicking its neural networks. Essentially, instead of relying on only two resistance states (metallic and insulating), future neuromorphic devices will use a pseudocontinuum of states [90] *produced* by tunable resistances. This will not only allow for faster and energy-reduced processing, memory storage and computing, but also enable neuromorphic chips to compute more flexibly and broadly [91]. Consequently, tunable resistances are essential to devices with these types of networks. Although such technology already exists, *e.g.*, phase change memories, they are prone to non-linear and asymmetric resistance tuning, which are detrimental because they lead to large write errors [92]. The possibility of exploiting the MIT in rare-earth nickelates for neuromorphic computation is not unknown [90], and if the linear temperature-dependence in the stoichiometric, as-deposited NdNiO$_3$ thin films persist after cycling, it may become a promising material for neuromorphic device technology. The results that have been obtained here are far from substantial enough to make a

definitive prediction and we do not claim to show device concept, but future studies in this direction may be valuable to determine if there is potential to be harvested. Some straightforward extensions of the work could include determining the relative (%) and absolute resistance change, the temperature range over which the linearity is valid, the tunability with repeated cycles, and whether the differences between as-deposited and annealed samples are retained.

The suggestions for future work, improvements, extensions and applications that have been brought up here are far from exhaustive. This thesis considers the work for a rather specific context and it would certainly be interesting to hear different perspectives on the methods and results that have been presented. It therefore seems fitting to conclude the main chapters of the thesis with an invitation to reflect on, challenge and discuss this work, whether it is individually or through scientific discourse.

References

1.   Rupp, K., *42 Years of Microprocessor Trend Data* in *Karl Rupp Computational Scientist* 2018.
2.   *Moore's Law: The number of transistors per microprocessor*, in *Our World in Data*, G.C.D. Lab, Editor. 2016.
3.   Zhang, H.-T., et al., *Reconfigurable perovskite nickelate electronics for artificial intelligence.* 2022: p. 8.
4.   Demazeau, G., et al., *Sur une série de composés oxygènes du nickel trivalent derivés de la perovskite.* Journal of Solid State Chemistry, 1971. **3**(4): p. 582-589.
5.   Catalano, S., et al., *Rare-earth nickelates RNiO3: thin films and heterostructures.* Reports on Progress in Physics, 2018. **81**(4): p. 046501.
6.   Tiwari, A., C. Jin, and J. Narayan, *Strain-induced tuning of metal–insulator transition in NdNiO3.* Applied Physics Letters, 2002. **80**(21): p. 4039-4041.
7.   Kumar, Y., R.J. Choudhary, and R. Kumar, *Strain controlled systematic variation of metal-insulator transition in epitaxial NdNiO3 thin films.* Journal of Applied Physics, 2012. **112**(7): p. 073718.
8.   Wang, L., et al., *Strain Effect on Oxygen Evolution Reaction Activity of Epitaxial NdNiO3 Thin Films.* ACS Applied Materials & Interfaces, 2019. **11**(13): p. 12941-12947.
9.   Heo, S., et al., *Influence of tensile-strain-induced oxygen deficiency on metal-insulator transitions in NdNiO3−δ epitaxial thin films.* Scientific Reports, 2017. **7**(1): p. 4681.
10.   Breckenfeld, E., et al., *Effects of Nonequilibrium Growth, Nonstoichiometry, and Film Orientation on the Metal-to-Insulator Transition in NdNiO3 Thin Films.* ACS Applied Materials & Interfaces, 2014. **6**(24): p. 22436-22444.
11.   Wang, L., et al., *Self-powered sensitive and stable UV-visible photodetector based on GdNiO3/Nb-doped SrTiO3 heterojunctions.* Applied Physics Letters, 2017. **110**(4): p. 043504.
12.   Sidik, U., et al., *Catalytic Hydrogen Doping of NdNiO3 Thin Films under Electric Fields.* ACS Applied Materials & Interfaces, 2020. **12**(49): p. 54955-54962.
13.   Shi, J., et al., *A correlated nickelate synaptic transistor.* Nature Communications, 2013. **4**(1): p. 2676.
14.   García-Muñoz, J.L., et al., *Influence of carrier injection on the metal-insulator transition in electron- and hole-doped $R_{1-x}A_xNiO_3$ perovskites.* Physical Review B, 1995. **52**(18): p. 13563-13569.
15.   Frand, G., et al., *Tuning of Metal/Insulator Transition around Room Temperature of Perovskites Sm1-xNdxNiO.3.* Journal of solid state chemistry, 1995. **120**(1): p. 157.
16.   Ambrosini, A. and J.-F. Hamet, *SmxNd1-xNiO3 thin-film solid solutions with tunable metal-insulator transition synthesized by alternate-target pulsed-laser deposition.* Applied physics letters, 2003. **82**(5): p. 727-729.
17.   Sønsteby, H.H., et al., *A foundation for complex oxide electronics -low temperature perovskite epitaxy.* Nature Communications, 2020. **11**(1): p. 1-7.
18.   Rykkje, L.-M., *Memristive Samarium Nickelate Thin Films* 2020, University of Oslo Oslo. p. 66.
19.   Verne, M.N., *ЁuNiO3 thin films by ALD* in *Department of Chemistry*. 2021, University of Oslo: Oslo, Norway.

20.   Amedjkhou, Y.L., *Synthesis and characterization of GdNiO₃ ALD thin films* 2022, University of Oslo: Oslo.

21.   Sun, Y., et al., *Electrochromic Properties of Perovskite NdNiO3 Thin Films for Smart Windows.* ACS Applied Electronic Materials, 2021. **3**(4): p. 1719-1731.

22.   Van Santen, J.H. and G.H. Jonker, *Electrical conductivity of ferromagnetic compounds of manganese with perovskite structure.* Physica, 1950. **16**(7): p. 599-600.

23.   Wang, N., et al., *Structure, Performance, and Application of BiFeO3 Nanomaterials.* Nano-micro letters, 2020. **12**(1): p. 81-81.

24.   Sun, Y., et al., *Unfolding B-O-B Bonds for an Enhanced ORR Performance in ABO3-Type Perovskites.* Small, 2019. **15**(29): p. 1803513.

25.   Jellite, M., et al., *Investigation of LaVO3 based compounds as a photovoltaic absorber.* Solar energy, 2018. **162**: p. 1-7.

26.   Kivelson, S. and S.A. Kivelson, *Defining emergence in physics.* npj Quantum Materials, 2016. **1**(1): p. 1-2.

27.   Herklotz, A., et al., *Controlling Octahedral Rotations in a Perovskite via Strain Doping.* Scientific Reports, 2016. **6**(1): p. 26491.

28.   *The Shapes of Atomic Orbitals.* Chemistry.

29.   Khomskii, D.I., *Transition Metal Compounds*. 2014, Cambridge: Cambridge: Cambridge University Press.

30.   Mercy, A., et al., *Structurally triggered metal-insulator transition in rare-earth nickelates.* Nature Communications, 2017. **8**(1): p. 1677.

31.   Haule, K. and G.L. Pascut, *Mott Transition and Magnetism in Rare Earth Nickelates and its Fingerprint on the X-ray Scattering.* Scientific Reports, 2017. **7**(1): p. 10375.

32.   Varignon, J., et al., *Reconciling the ionic and covalent pictures in rare-earth nickelates.* npj Quantum Materials, 2017. **2**(1): p. 21.

33.   García-Muñoz, J.L., et al., *Neutron-diffraction study of RNiO 3 (R =La,Pr,Nd,Sm): Electronically induced structural changes across the metal-insulator transition.* Physical Review B, 1992. **46**(8): p. 4414-4425.

34.   Torrance, J., et al., *Systematic study of insulator-metal transitions in perovskites RNiO3 (R=Pr,Nd,Sm,Eu) due to closing of charge-transfer gap.* Physical Review B, 1992. **45**(14): p. 8209-8212.

35.   Catalan, G., *Progress in perovskite nickelate research.* Phase Transitions, 2008. **81**(7-8): p. 729-749.

36.   Badrtdinov, D.I., A. Hampel, and C.E. Dreyer, *Interplay between breathing-mode distortions and magnetic order in rare-earth nickelates from ab $initio$ magnetic models.* Physical Review B, 2021. **104**(5): p. 054403.

37.   Meyers, D., et al., *Pure electronic metal-insulator transition at the interface of complex oxides.* Scientific Reports, 2016. **6**(1): p. 27934.

38.   Obradors, X., et al., *Pressure dependence of the metal-insulator transition in the charge-transfer oxides RNiO3 (R=Pr,Nd).* Physical Review B, 1993. **47**(18): p. 12353-12356.

39.   Scherwitzl, R., et al., *Electric-Field Control of the Metal-Insulator Transition in Ultrathin NdNiO3 Films.* Advanced Materials, 2010. **22**(48): p. 5517-5520.

40.   Hu, W., et al., *Broadband terahertz spectroscopy of the insulator-metal transition driven by coherent lattice deformation at the SmNiO3/LaNiO3 interface.* Physical Review B, 2016. **93**(16): p. 161107.

41.	Catalano, S., et al., *Electronic transitions in strained SmNiO3 thin films.* APL materials, 2014. **2**(11): p. 116110-116110-7.

42.	Conchon, F., et al., *Effect of tensile and compressive strains on the transport properties of SmNiO3 layers epitaxially grown on (001) SrTiO3 and LaAlO3 substrates.* Applied physics letters, 2007. **91**(19): p. 192110.

43.	Hauser, A.J., et al., *Correlation between stoichiometry, strain, and metal-insulator transitions of NdNiO3 films.* Applied Physics Letters, 2015. **106**(9).

44.	Yao, D., et al., *Tuning the metal-insulator transition via epitaxial strain and Co doping in NdNiO3 thin films grown by polymer-assisted deposition.* Journal of Applied Physics, 2016. **119**(3): p. 035303.

45.	Medarde, M., et al., *Giant $^{16}O\ensuremath{-}^{18}O$ Isotope Effect on the Metal-Insulator Transition of $\mathit{R}{\mathrm{NiO}}_{3}$ Perovskites ($\mathit{R}\phantom{\rule{0ex}{0ex}}=\phantom{\rule{0ex}{0ex}}$Rare Earth).* Physical Review Letters, 1998. **80**(11): p. 2397-2400.

46.	Nikulin, I.V., et al., *Oxygen nonstoichiometry of NdNiO3−δ and SmNiO3−δ.* Materials Research Bulletin, 2004. **39**(6): p. 775-791.

47.	Herklotz, A., et al., *Strain coupling of oxygen non-stoichiometry in perovskite thin films.* Journal of Physics: Condensed Matter, 2017. **29**(49): p. 493001.

48.	Catalano, S., et al., *Tailoring the electronic transitions of NdNiO $_3$ films through (111) $_{pc}$ oriented interfaces.* APL Materials, 2015. **3**(6).

49.	Lim, S., *ALD cycle* 2022.

50.	H. Sønsteby, H., et al., *Avoiding water reservoir effects in ALD of functional complex alkali oxides by using O 3 as the oxygen source.* Dalton Transactions, 2022. **51**(3): p. 927-934.

51.	Stary, J. and J.O. Liljenzin, *Critical evaluation of equilibrium constants involving acetylacetone and its metal chelates.* Pure and Applied Chemistry, 1982. **54**(12): p. 2557-2592.

52.	Mills, B. *Acetylacetone enol tautomer from xtal Mercury 3D balls* [Image] 2020 June 7 [cited 2022.

53.	Corsini, C., S. Peeters, and M.C. Righi, *Adsorption and Dissociation of Ni(acac)2 on Iron by Ab Initio Calculations.* The Journal of Physical Chemistry A, 2020. **124**(39): p. 8005-8010.

54.	Sønsteby, H.H., A. Yanguas-Gil, and J.W. Elam, *Consistency and reproducibility in atomic layer deposition.* Journal of Vacuum Science & Technology A: Vacuum, Surfaces, and Films, 2020. **38**(2): p. 020804.

55.	Puurunen, R.L., *Surface chemistry of atomic layer deposition: A case study for the trimethylaluminum/water process.* Journal of Applied Physics, 2005. **97**(12): p. 121301.

56.	Vehkamäki, M., *Atomic Layer Deposition of Multicomponent Oxide Materials.* 2022, University of Helsinki: Helsinki.

57.	Sønsteby, H.H., et al., *Effect of Subcycle Arrangement on Direct Epitaxy in ALD of LaNiO3.* ACS Applied Electronic Materials, 2021. **3**(1): p. 292-298.

58.	Gonçalves, D. and E.A. Irene, *Fundamentals and applications of spectroscopic ellipsometry.* Quim. Nova, 2001. **25**(5): p. 7.

59.	Benzitouni, S., A. Mahdjoub, and M. Zaabat, *Spectroscopic Ellipsometry Characterization of Thin Films Deposited on Silicon Substrate.* Journal of New Technology and Materials, 2014. **4**: p. 138-142.

60.	Shah, D., et al., *A Tutorial on Spectroscopic Ellipsometry (SE), 2. The Cauchy Model.* 2019.

61.	*Ellipsometry FAQ.* [cited 2022; Available from: https://www.jawoollam.com/resources/ellipsometry-faq#toggle-id-5.

62.	Harrington, G.F. and J. Santiso, *Back-to-Basics tutorial: X-ray diffraction of thin films.* Journal of Electroceramics, 2021.

63.	Soares, C., et al., *High surface area LaNiO3 electrodes for oxygen electrocatalysis in alkaline media.* Journal of Applied Electrochemistry, 2012. **42**.

64.	Tucker, J., *The Highs and Lows of Resistance Measurements: Can You Trust Your Test? Pt. 2*, in *EEWeb.* 2012.

65.	Smits, F.M., *Measurement of sheet resistivities with the four-point probe.* The Bell System Technical Journal, 1958. **37**(3): p. 711-718.

66.	Hansen, P.-A., et al., *Structural and optical properties of lanthanide oxides grown by atomic layer deposition (Ln = Pr, Nd, Sm, Eu, Tb, Dy, Ho, Er, Tm, Yb).* Dalton Transactions, 2013. **42**(30): p. 10778-10785.

67.	Dobbelaere, T., P.M. Vereecken, and C. Detavernier, *A USB-controlled potentiostat/galvanostat for thin-film battery characterization.* HardwareX, 2017. **2**: p. 34-49.

68.	Utriainen, M., M. Kröger-Laukkanen, and L. Niinistö, *Studies of NiO thin film formation by atomic layer epitaxy.* Materials science & engineering. B, Solid-state materials for advanced technology, 1998. **54**(1): p. 98-103.

69.	Nilsen, O., H. Fjellvåg, and A. Kjekshus, *Inexpensive set-up for determination of decomposition temperature for volatile compounds.* Thermochimica Acta, 2003. **404**(1): p. 187-192.

70.	Cammarata, A. and J.M. Rondinelli, *Electronic doping of transition metal oxide perovskites.* Appl. Phys. Lett., 2016: p. 5.

71.	Bratvold, J.E., H. Fjellvåg, and O. Nilsen, *Atomic Layer Deposition of oriented nickel titanate (NiTiO3).* Applied Surface Science, 2014. **311**: p. 478-483.

72.	Nilsen, O., et al., *Growth of La1-xCaxMnO3 thin films by atomic layer deposition.* Journal of materials chemistry, 2007. **17**(15): p. 1466-1475.

73.	Tiwari, A. and K.P. Rajeev, *Effect of oxygen stoichiometry on the electrical resistivity behaviour of NdNiO3-δ.* Solid state communications, 1998. **109**(2): p. 119-124.

74.	Guo, Q., et al., *Tunable resistivity exponents in the metallic phase of epitaxial nickelates.* Nat Commun, 2020. **11**(1): p. 2949-2949.

75.	Upton, M.H., et al., *Novel Electronic Behavior Driving ${\mathrm{NdNiO}}_{3}$ Metal-Insulator Transition.* Physical Review Letters, 2015. **115**(3): p. 036401.

76.	Ruddlesden, S.N. and P. Popper, *The compound Sr3Ti2O7 and its structure.* Acta Cryst, 1958. **11**(1): p. 54-55.

77.	Qi, H., et al., *Formation mechanism of Ruddlesden–Popper faults in compressive-strained ABO3 perovskite superlattices.* Nanoscale, 2021. **13**(48): p. 20663-20669.

78.	Jing, H.-M., et al., *Formation of Ruddlesden–Popper Faults and Their Effect on the Magnetic Properties in Pr0.5Sr0.5CoO3 Thin Films.* ACS Appl. Mater. Interfaces, 2018. **10**(1): p. 1428-1433.

79.	Bak, J., et al., *Effect of Lattice Strain on the Formation of Ruddlesden–Popper Faults in Heteroepitaxial LaNiO 3 for Oxygen Evolution Electrocatalysis.* 2020: Washington, D.C. :. p. 7253-7260.

80. Yang, C., et al., *Ruddlesden–Popper Faults in NdNiO3 Thin Films.* Symmetry, 2022. **14**: p. 464.

81. Liu, J., et al., *Heterointerface engineered electronic and magnetic phases of NdNiO3 thin films.* Nature Communications, 2013. **4**(1): p. 2714.

82. Zaghrioui, M., P. Laffez, and P. Goudeau, *Qualitative X-ray diffraction analysis of residual stresses in NdNiO3 thin films with metal-insulator transition.* Journal of Materials Science Letters, 2002: p. 1379-1383.

83. Alonso, J.A., et al., *Metal–Insulator Transitions, Structural and Microstructural Evolution of RNiO3 (R = Sm, Eu, Gd, Dy, Ho, Y) Perovskites: Evidence for Room-Temperature Charge Disproportionation in Monoclinic HoNiO3 and YNiO3.* J. Am. Chem. Soc, 1999. **121**(20): p. 4754-4762.

84. Medarde, M., et al., *Charge disproportionation in $R{\text{NiO}}_{3}$ perovskites ($R=\text{rare}$ earth) from high-resolution x-ray absorption spectroscopy.* Physical Review B, 2009. **80**(24): p. 245105.

85. Valdes, L.B., *Resistivity Measurements on Germanium for Transistors.* Proceedings of the IRE, 1954. **42**(2): p. 420-427.

86. Osada, M., et al., *A Superconducting Praseodymium Nickelate with Infinite Layer Structure.* Nano Letters, 2020. **20**(8): p. 5735-5740.

87. Zeng, S.W., et al., *Superconductivity in infinite-layer nickelate La$_{1-x}$Ca$_x$NiO$_2$ thin films*. 2022.

88. Osada, M., et al., *Nickelate Superconductivity without Rare-Earth Magnetism: (La,Sr)NiO2.* Advanced Materials, 2021. **33**(45): p. 2104083.

89. Li, D., et al., *Superconductivity in an infinite-layer nickelate.* Nature, 2019. **572**(7771): p. 624-627.

90. Preziosi, D., et al., *Direct Mapping of Phase Separation across the Metal–Insulator Transition of NdNiO3.* Nano Letters, 2018. **18**(4): p. 2226-2232.

91. Rand, D., *What's this neuromorphic computing you're talking about?* HPE, 2021.

92. Melianas, A., et al., *Temperature-resilient solid-state organic artificial synapses for neuromorphic computing.* Science Advances, 2020. **6**(27): p. eabb2958.

93. Rao, C.N.R., *Transition Metal Oxides.* Annual Review of Physical Chemistry, 1989. **40**(1): p. 291-326.

94. Khomskii, D.I., *Strongly correlated electrons*, in *Basic Aspects of the Quantum Theory of Solids: Order and Elementary Excitations*, D.I. Khomskii, Editor. 2010, Cambridge University Press: Cambridge. p. 229-271.

95. Khomskii, D.I., *Metal-insulator transitions*, in *Transition metal compounds*. 2014, Cambridge University Press: Cambridge.

96. Zaanen, J., G.A. Sawatzky, and J.W. Allen, *Band gaps and electronic structure of transition-metal compounds.* Physical Review Letters, 1985. **55**(4): p. 418-421.

97. Hüfner, S., *Analysis of the core level satellites in XPS spectra of Ni dihalides.* Solid State Communications, 1984. **49**(12): p. 1177-1179.

98. Medarde, M., M.T. Fernández-Díaz, and P. Lacorre, *Long-range charge order in the low-temperature insulating phase of PrNiO 3.* Physical Review B, 2008. **78**(21): p. 212101.

99. Mazin, I.I., et al., *Charge Ordering as Alternative to Jahn-Teller Distortion.* Physical Review Letters, 2007. **98**(17): p. 176406.

100. Sønsteby, H., *Structural Investigation of Crystalline Systems Utilizing Synchrotron X-ray Radiation* in *Department of Chemistry*. 2012, University of Oslo: Oslo, Norway. p. 213.

101. Montes, A.M., *XRD peak broadening and the Williamson-Hall analysis* 2014, Nanomagnetism group. p. 11.

Appendix

A.1 MIT Theories

To better understand the nature of the RNOs, it is instructive to begin by considering what a metal physically is since this in many ways represents the core of the problem. A suggested definition that is neither too general nor detailed is perhaps this: a material with mobile charge carriers that can move around freely. Although the analogy of "a sea of electrons" is commonly used to evoke a sense of natural, free movement, band theory of solids is a more descriptive and accurate model that describes the same idea. A band is the continuum of "infinite" orbitals in a solid, visualized in Figure X, and is filled with electrons. If the band is partially full or overlaps in energy with another band, then there are available states for the electrons to be scattered to, *i.e.*, there are charge carriers present that can move around (somewhat) freely – it is a metal.

In rare-earth nickelates, the nickel ion takes on a 3+ charge, which means that it has seven electrons in its d-shell (a d^7 ion), out of the possible ten. Upon forming a d-band in a solid, it would be partially filled and this should, according to traditional band theory, make it a metal. As such, it was unexpected to discover that the rare earth nickelates so readily assumed an insulating state at lower temperatures that existing models could not explain.

One of the first successful microscopic interpretations of this was developed by Mott and Hubbard. In their interpretation they included strong electron-electron interactions in a single electronic band in a periodic lattice, with particular emphasis on the d-band. This deviated from the single-particle approximations that were used in conventional band theory [93], but was more accurate in light of how strongly confined and correlated the d-electrons are in transition metal compounds.

The Hubbard model considers the process in which localized electrons hop to a neighboring site, described as $d^n + d^n \rightarrow d^{n+1} + d^{n-1}$. There are two parameters that describe the interaction potential for the process: Coulomb repulsion (U) and hopping amplitude (t, not to be confused with the Goldschmidt tolerance factor). On-site Coulomb repulsion arises from the double occupancy of electrons on a single site and favors localized electrons. On the other hand, the kinetic energy of the electron, gauged by hopping amplitude, impels it to move and thus tends towards delocalization, so-called itineracy. The competition between the strengths of these two energy scales therefore determines whether the system's ground state is itinerant (U < t) or localized (U > t). For strongly correlated electronic systems, U >> t and the energetic cost of moving an electron to an already occupied site would be so large, ~U, that it becomes more favorable to localize electrons at the expense of increasing kinetic energy [94]. The resulting insulating state is termed a *Mott insulator*.

Notably, the insulating state is attained even though there technically are available sites for the electrons to move to. This is best understood as a result of additional splitting of the d-band into an upper and lower Hubbard sub-band (UHB and LHB, respectively). In a half-filled system and $U \gg t$, Coulomb repulsion causes every lattice site to be occupied by a single electron and these occupied states represent a full LHB [75]. If the system is less than half-full, it would again be expected to behave like a metal since there are available states for electrons to move to without a significant energetic cost, *i.e.,* they do not need to traverse the band gap to reach an available site. At half-filling, however, once all sites are occupied an electron would have to overcome the large Coulomb repulsion to move to a neighboring site and this energy is what separates the fully occupied LHB from the completely empty UHB. It is important to remark that this band gap is of a consequentially very different nature than in conventional band theory. In the latter, interactions between electrons and the periodic lattice potential gives rise to an energy gap, whereas in the Mott-Hubbard picture it stems from the interaction between electrons [95].

While Mott theory based on the Hubbard model was an important step for introducing electron correlations, it was pointed out by Zaanen, Sawatzky and Allen (ZSA) that certain transition metal compounds containing Co, Ni, or Cu [96] still diverged from theory. Drawing on the work of Stefan Hüfner [97], they proposed a new theory for the electronic structure of these compounds and developed the idea of another type of insulator distinctly different from the Mott insulator. Mott had assumed that the insulating gap is of d-d character, arising from the aforementioned d-electron interactions. ZSA posited that a charge transfer mechanism involving the ligand may dominate the insulating gap more than d-d excitations in certain cases, eliminating the Coulomb repulsion from the equation. Instead of doubly occupied site, they were concerned with the process described as $d^n + d^n \rightarrow d^{n+1} + d^n\underline{L}$. Here, $\underline{L}$ is a ligand hole that reflects the transfer of an electron from the ligand oxygen p-orbital to the transition metal. This transfer is associated with the energy Δ and takes the place of Coulomb repulsion U in dictating the insulating gap. *Charge-transfer insulators* thus differ from Mott insulators in that the relevant charge transfer defining the insulating gap is of d-p character. Within this renewed ZSA framework, shown in Figure X, the insulating state of a transition metal compound can be characterized by the energy that defines its smallest band gap, i.e. Mott-type if $U < \Delta$, and charge-transfer-type if $U > \Delta$.

In spite of this seemingly coherent development of theories, it has been difficult to find a unifying theory that can be reconciled with the decades of various experimental observations that have been made. One of the findings that has been at the center of the debate is the appearance of charge disproportionation (CD), called a signature fingerprint of the MIT in rare-earth nickelates. The creation of two inequivalent Ni-sites with distinct charges ($Ni^{3+} \rightarrow Ni^{2+} + Ni^{4+}$) aligns well with the observed bond-disproportionation [98] and breathing mode activation [32]. Comparing this to the Mott-

Hubbard process reveals a striking similarity that naturally led many to conclude that rare-earth nickelates were indeed Mott insulators.

Charge ordering (CO) in the form of CD could also explain the lack of Jahn-Teller distortion that was expected to occur in rare-earth nickelates [99]. Ni^{3+} is a d^7-ion, which has degenerate orbitals (same energy) and should undergo geometrical distortion; however, it does not. It has therefore been postulated that the system essentially removes orbital degeneracy by getting rid of the degenerate electron.

Other studies, in turn, have found no evidence of charge ordering to the extent that CD proponents claim. For instance, the type of charge transfer through a ligand hole proposed by ZSA would be physically distinct from a proper charge ordering because the actual movement of charge is small and occurs between ligand and metal instead of neighboring metal atoms. The lack of observed charge movement has therefore been interpreted as evidence for the MIT occurring by purely closing the CT gap (between Ni^{3+} and O^{2-} [6]), starting from an initial d^7 (Ni^{3+}) ground state configuration and ending up as $d^8\underline{L} + d^7$, as described by the ZSA framework.

A.2 Diffractogram for NdNiO$_3$ on Si(100)

Diffractogram obtained for NdNiO$_3$ grown on Si(100) without etching the native SiO$_2$ layer on the substrate surface. Only the reflections from the substrate is visible, indicating that the film grows amorphously on Si(100).
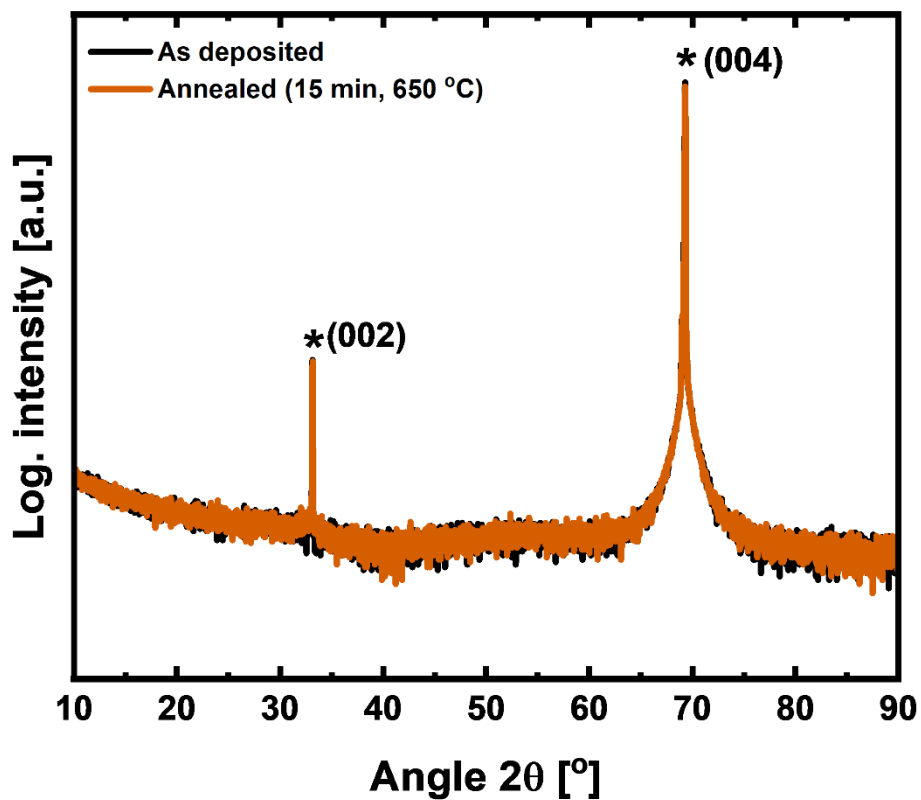
Figure A.2 X-ray diffractogram for NdNiO$_3$ thin films deposited on a Si(100) substrate, shown for as deposited (black) and after annealing at 650 °C for 15 minutes (orange). The reflections correspond to the (200) and (400) planes from the substrate, labeled with asterisks. No thin film reflections are visible.

A.3 Master Data Table

Series	Sample name	Pulsed ratio (Nd:Ni)	Diffractogram thin film reflections	Specific resistivity [Ωcm]		Nd content [%]
				AD	AA	
Stoichiometric	LR1078	3:1	Y	1.83E-1	3.68E-4	N/A
	LR1086	3:1	Y (not as separated)	-	4.85E-4	N/A
	LR1095	3:1	Y	6.77E-3	4.04E-4	48.83
	LR1161	3:1	Y	2.05E-1	8.50E-4	50.39
	LR1162	3:1	Y	2.85E-3	4.34E-4	49.33
	LR1178	3:1	N	-	-	48.92
Stoichiometric ratio multiples (multilayers)	LR1079	6:2	N	-	3.39E-2	N/A
	LR1082	6:2	N	-	3.57E-2	N/A
	LR1087	6:2	N	-	4.53E-2	N/A
	LR1181	6:2	Y	2.70E-1	9.17E-4	48.70
	LR1080	12:4	Y	-	1.02E-3	N/A
	LR1083	12:4	N	-	5.60E-2	N/A
	LR1088	12:4	Y	-	6.33E-4	N/A
	LR1081	24:8	Y *	-	3.39E-2	N/A
Stoichiometric ratio multiple variations	LR1093	5:2	Y	2.85E-2	8.55E-4	44.61
	LR1121	5:2	N	-	3.24E-2	46.70
	LR1092	7:2	Y †	-	7.37E-3	72.13
	LR1182	7:2	Y	9.97E-4	N/A	50.09
	LR1183	7:2	Y	2.34E-2	5.48E-4	50.46
	LR1096	11:4	Y *	-	-	N/A
	LR1097	13:4	N	-	2.65E-2	N/A

* On left side

† Broadening

N/A because Si-substrates or 3x3 cm^2 substrates needed for XRF were not included in deposition

A.4 Reciprocal space map of NNO3:1

A reciprocal space map was also obtained for one of the NNO3:1-films, reproduced in Figure A.4. This specific sample corresponds to the one that was analyzed with XPS, but was not included in the main results because it was more relevant to compare the same thin film before and after annealing.
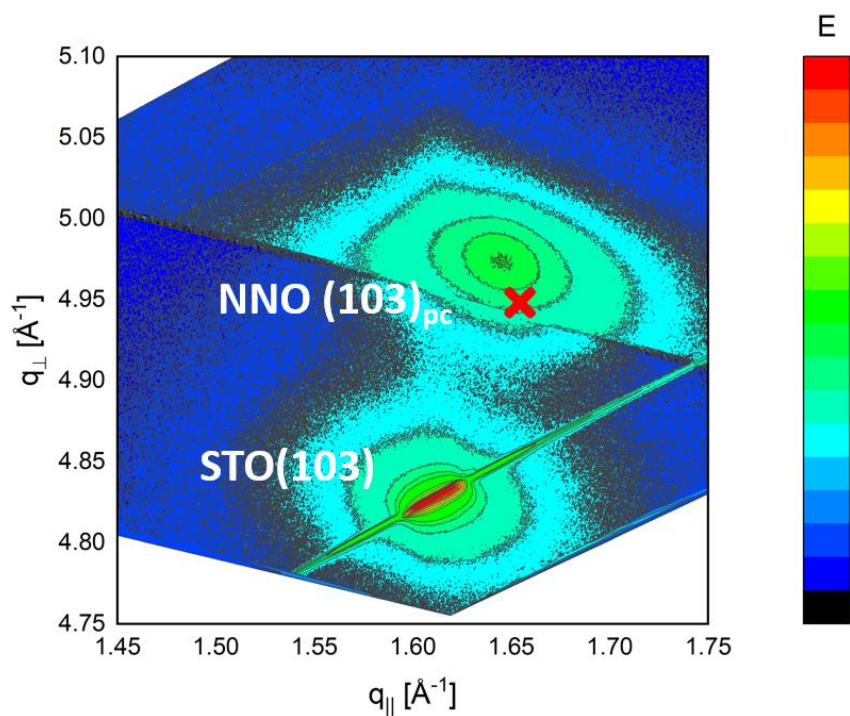

Figure A.4 Reciprocal space map of the (103) reflection from a NdNiO₃ thin film on SrTiO₃(001) for a 3:1 (Nd:Ni)-pulsed sample.

A.5 Derivation of Williamson-Hall

Williamson Hall analysis can be used to estimate the crystallite size and strain from the observed broadening of their Bragg peaks in the diffractogram. Crystallite size is originally be related to peak breadth through the Scherrer equation:

$$\beta_{size} = \frac{k\lambda}{D_c \cos\theta},$$

where k is the shape factor and D_c the crystallite size. Microstrain can also contribute to broadening by introducing non-uniform lattice distortions that allow Bragg scattering over a narrow range of angles. The expression for this relation is given as:

$$\beta_{strain} = 4\epsilon \frac{\sin\theta}{\cos\theta}.$$

Here, ϵ is related to the lattice distortion. Using that the breadths are additive, we obtain

$$\beta_{observed} = \beta_{size} + \beta_{strain} = \frac{k\lambda}{D_c \cos\theta} + 4\epsilon \tan\theta,$$

which can be rearranged to

$$\beta_{observed} \cos\theta = \frac{k\lambda}{D_c} + 4\epsilon \sin\theta.$$

This resembles a linear equation on the form y = a + bx, giving that the crystallite size, D_c, can be deduced from $\beta_{observed} \cos\theta$, when $4\epsilon \sin\theta = 0$, and strain becomes the slope of a best-fit line for the different reflections.

The summary of this derivation was based on [100, 101].

A.6 Pulses for Rare-Earth Oxides

The pulse durations for the rare-earth precursors, RE(thd)$_2$, were experimentally determined by investigating the point of saturation, similarly as described for Nd(thd)$_3$ and Ni(acac)$_2$. The results are compiled in Figure A.6. Gd(thd)$_3$ underwent more extensive tests because there was no obvious plateau even at excessive pulse durations, but this was later achieved by increasing its sublimation temperature to 140 °C.
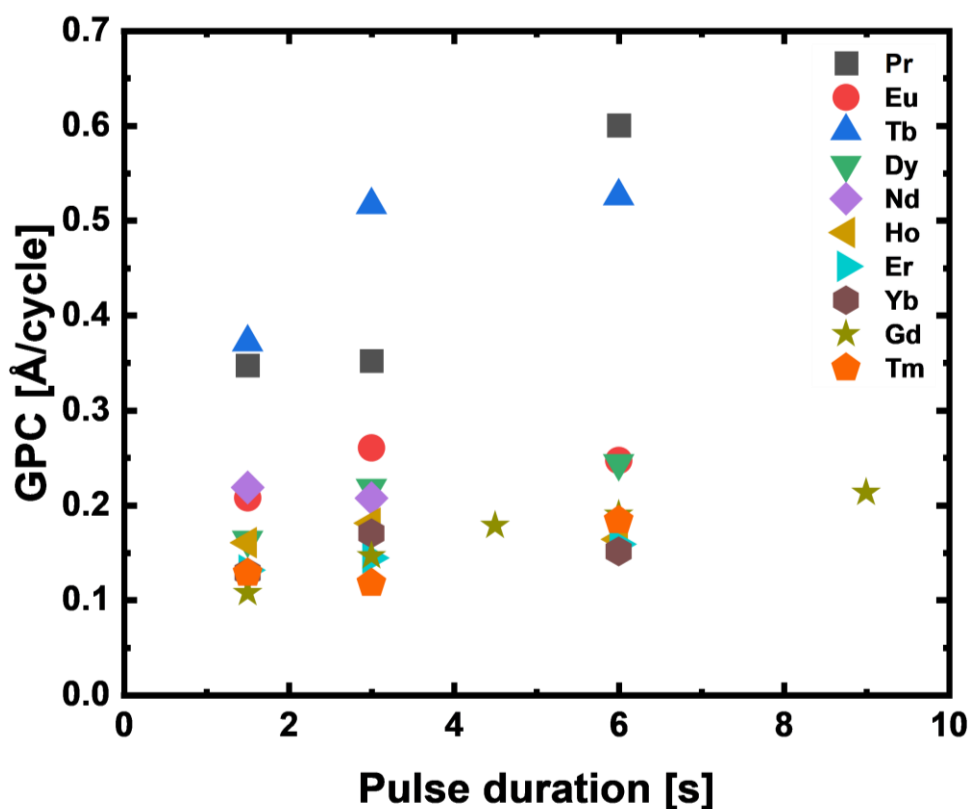

Figure A.6 Experimental tests for pulse durations of RE(thd)$_3$, where RE = rare-earth element.

A.7 Room-temperature Resistivity of As-Deposited Rare-Earth Substituted Thin Films

The resistivity of rare-earth substituted thin films as deposited was not included in the figures for the 1:2:1 and 1:6:2 pulsing regimes for the sake of maintaining a readable graph. Additionally, quite few of the samples of these two substitution schemes conducted as deposited, as can be seen in Figure A.7 (1:6:2) and Y (1:2:1).

Sm-NNO1:6:2 also appears anomalous since the resistivity of the film as deposited is lower than after annealing. It is likely a result of experimental error and the difference (3E-3) can almost certainly be considered within experimental uncertainty.
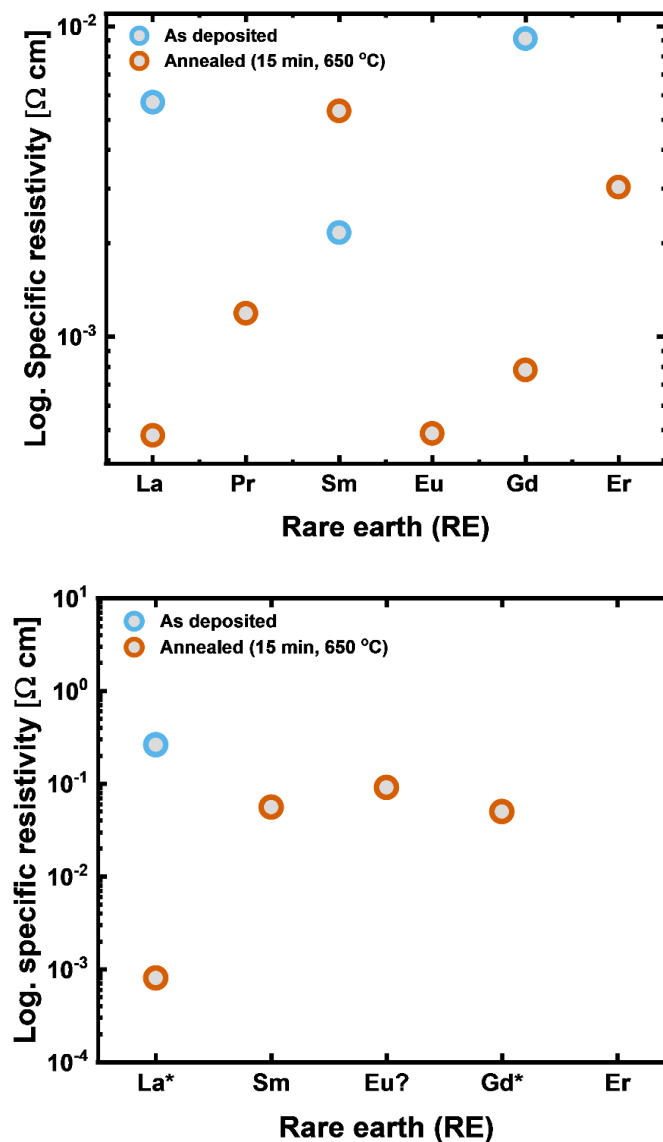

Figure A.7 Room-temperature resistivities of (RE,Nd)NiO$_3$ thin films for a pulsing scheme of 1:6:2 (top) and 1:2:1 (bottom), for thin films as deposited (blue circle) and after annealing (orange circle).

A.8 Diffractograms for Rare-Earth Substitutions

The diffractograms for the rare-earth substituted thin films are shown grouped together according to substitution scheme: 1:6:2 (top), 1:4:2 (two middle), and 1:2:1 (bottom) in Figure A.8. The legend denotes which rare-earth element was substituted into the film, as deposited (AD) and after annealing (AA). Since there were so many different compositions with the 1:4:2 pulsing scheme, the as-deposited and annealed films are separated into two different graphs.
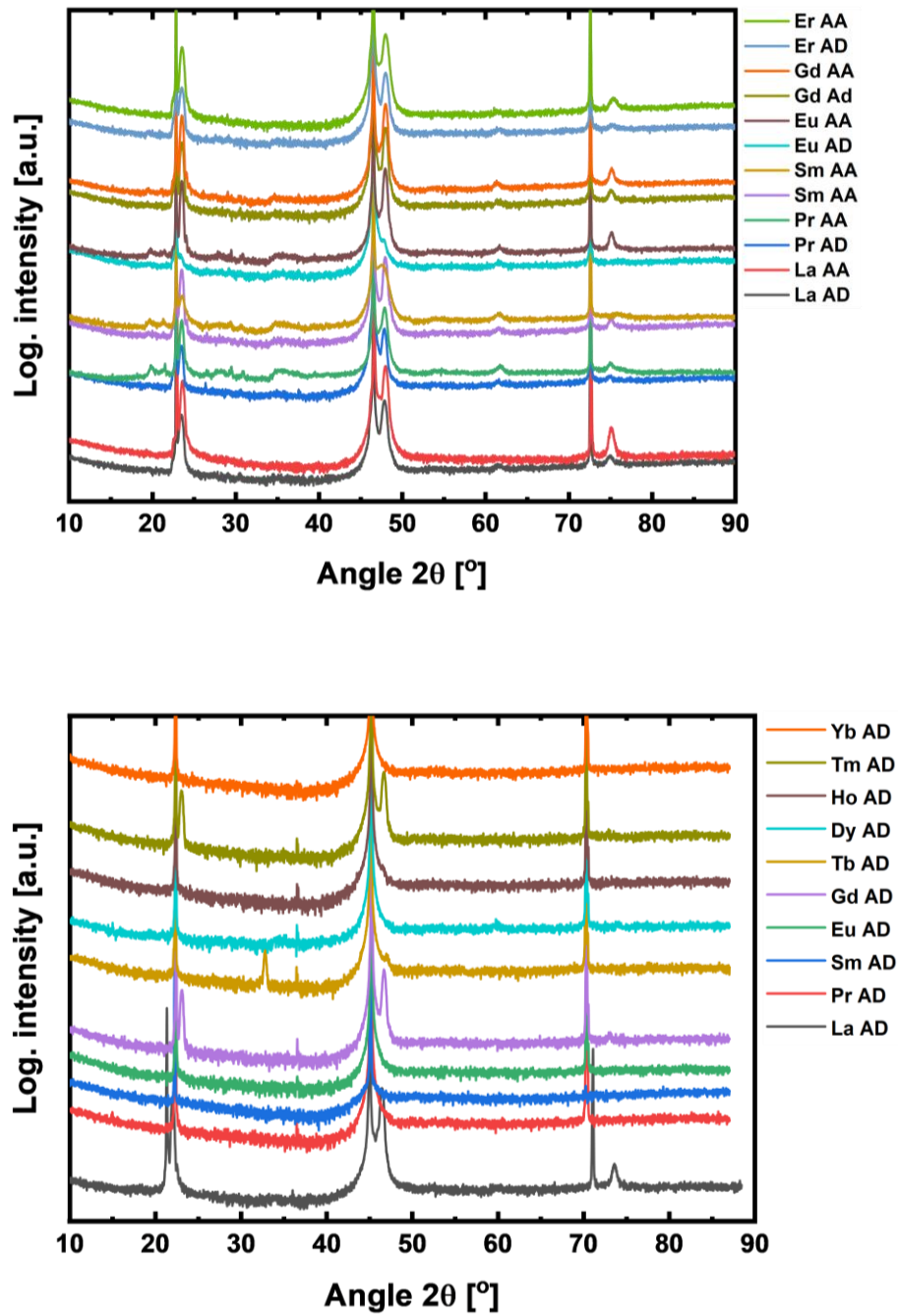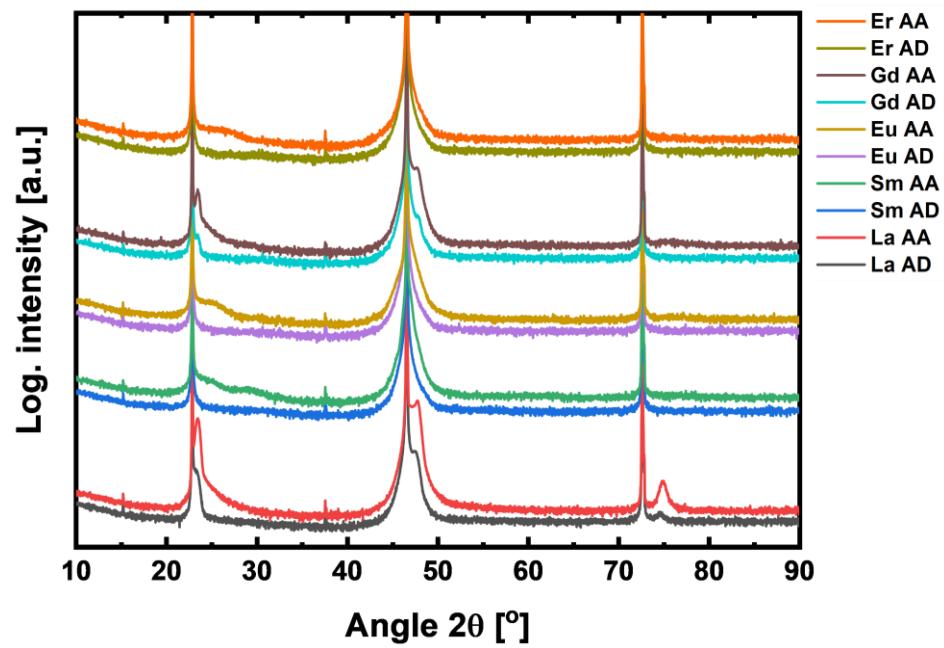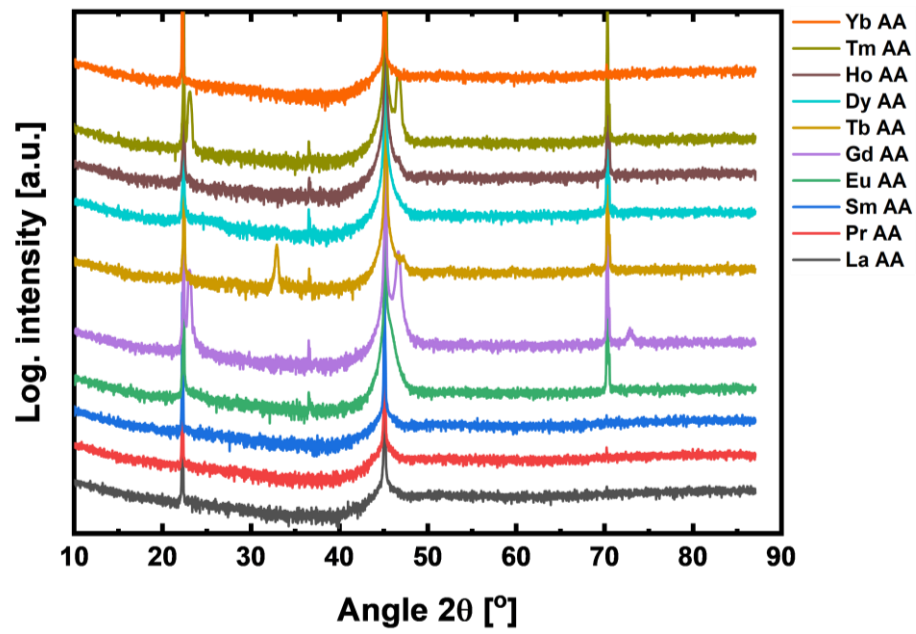
Figure A.8 Diffractograms for various thin films of (RE,Nd)NiO₃ deposited with different pulsing schemes, shown for films as deposited (AD) and after annealing (AA). Pulsing scheme 1:6:2 (top), 1:4:2 (two middle, AD and AA shown separately), and 1:2:1 (bottom).